



The University of  
**Nottingham**

---

# Diamagnetic Levitation of Bubbles and Droplets

---

by  
George Hunter-Brown

Thesis submitted to the University of Nottingham for the degree of Doctor of  
Philosophy

October 2023

# Abstract

This thesis describes the use of diamagnetic levitation to study fluids in a zero-gravity environment, particularly focusing on bubbles and droplets. We use a strong nonhomogeneous magnetic field (maximum field strength 18.5 T) generated by a superconducting solenoid magnet to repel/attract materials at a molecular level allowing for a net zero body force to be experienced by bubbles/droplets. A new technique that allows for the suspension of spherical gas bubbles in liquids at room temperature is presented. The development of this technique allowed for several novel experiments to be carried out.

Firstly, we use this technique to observe the coalescence of multiple pairs of air bubbles in water, starting from hydrostatic equilibrium. The coalescence creates large axisymmetric perturbations to the surface of the bubble which leads to the ejection of satellite bubbles. For the first time, we experimentally observe the simultaneous ejection of two satellite bubbles from the coalescence of a pair of air bubbles. After satellite bubbles are ejected, the bubble formed from the coalescence of the parent bubbles undergoes large nonlinear axisymmetric surface oscillations. We analyse these surface oscillations for two cases: a symmetric case, where the initial parent bubbles have equal radii (within experimental error) and an asymmetric case where the ratio of the radii of the two parent bubbles is  $\sim 1.5$ . We compare our results to the analytical model of Tsamopoulos and Brown and find that in the symmetric case, when only a single large amplitude surface mode is dominant, that experiment and simulation agree well with theory and the oscillation frequency of the dominant mode behaves as a function of the square of its amplitude. But, in the case several surface modes are oscillating with moderate or large amplitudes, agreement between the model of Tsamopoulos and Brown and what is observed in experiment and simulation is seen to be less accurate.

Secondly, we use this technique to observe and manipulate bubble clusters. We show that if a small amount of surfactant is added to the liquid, that air bubbles levitating in the liquid may remain in contact with each other without coalescing for an indefinite period of time. This allows for the creation of clusters of multiple diamagnetically levitated spherical air bubbles. We present bubble clusters created from up to 21 bubbles and show how the arrangement of these clusters may be altered by simply altering the current in the superconducting solenoid. Future use cases are hypothesised for bubble clusters, such as the production of new acoustic metamaterials and a new technique for the study of the nonlinear interaction of

bubbles in an oscillating acoustic field.

The final section of this thesis describes a new experimental technique ‘Sonomaglev’. This new technique combines both acoustic and diamagnetic levitation, allowing for the manipulation of multiple levitated spherical water droplets, using a superconducting magnet fitted with low-power ultrasonic transducers. We show that multiple droplets, arranged horizontally along a line, can be stably levitated with this system, and demonstrate controlled contactless coalescence of two droplets. Numerical simulation of the magnetogravitational and acoustic potential reproduces the multiple stable equilibrium points observed in our experiments.

# Acknowledgments

I would like to sincerely thank my supervisors, Dr Richard Hill and Dr Matthew Scase, for their endless encouragement, guidance and support throughout the entirety of my PhD. Their willingness and enthusiasm for me to pursue my own ideas has allowed me to carry out novel and interesting work that I am incredibly proud of and their unwavering passion for my work and research in general has kept me inspired and motivated even through difficult patches. I would also like to thank Dr Naresh Sampara, for all the time he spent teaching me how to use an assortment of experimental apparatus and for the many hours he spent with me in the lab helping me adjust and refine my experiments. I gratefully acknowledge the Leverhulme Trust for their financial support. I would also like to thank my family for all their love and support.

Finally, I would like to thank my fiancée, Vicki. Even on the hardest days you never failed to put a smile on my face and always knew the right words to keep me going. You are my rock; I can't imagine how I would have gotten here without you.

# Publications

G. Hunter-Brown, N. Sampara, M. M. Scase, and R. J. A. Hill, “Sonomaglev: Combining acoustic and diamagnetic levitation,” *Appl. Phys. Lett.*, vol. 122, no. 1, p. 014 103, 2023. DOI: 10.1063/5.0134297, (Article was chosen as Editor’s pick)

G. Hunter-Brown, N. Sampara, M. M. Scase, and R. J. A. Hill, “Nonlinear oscillations of a magnetically levitated air bubble in water,” *Phys. Rev. Fluids*, 2023, (*Manuscript sub judice*)

## Presentations at international conferences

G. Hunter-Brown, “Nonlinear oscillations of levitated air bubbles in water,” *European Fluid Mechanics Conference*, Athens, Greece, Sep. 2022

G. Hunter-Brown, “Nonlinear oscillations of levitated air bubbles in water,” *UK Fluids Conference*, Sheffield, United Kingdom, Sep. 2022

G. Hunter-Brown, “Nonlinear oscillations of levitated air bubbles,” *British Applied Mathematics Colloquium*, Loughborough, United Kingdom, Apr. 2022

# Contents

<b>Abstract</b>	<b>i</b>
<b>Acknowledgments</b>	<b>iii</b>
<b>Publications</b>	<b>iv</b>
<b>1 Introduction</b>	<b>1</b>
1.1 Levitation . . . . .	1
1.2 Thesis outline . . . . .	2
<b>2 Principles of diamagnetic levitation</b>	<b>5</b>
2.1 A brief history of diamagnetic levitation . . . . .	5
2.2 Earnshaw's theorem . . . . .	6
2.3 Diamagnetic levitation . . . . .	7
2.3.1 Stability conditions . . . . .	8
2.3.2 Stable zones of rotationally symmetric magnetic fields . . . . .	9
2.4 Cryogenic superconducting magnet . . . . .	12
2.5 Shape of magnetogravitational potential traps . . . . .	13
<b>3 Diamagnetic levitation of bubbles</b>	<b>23</b>
3.1 Stable diamagnetic levitation of room temperature spherical bubbles .	23
3.2 Experimental set-up . . . . .	25
3.3 Bubble coalescence experiments . . . . .	26
3.3.1 Image processing and analysis . . . . .	28
<b>4 Nonlinear surface oscillations of bubbles</b>	<b>31</b>
4.1 Theoretical models for the surface oscillations of bubbles . . . . .	31
4.2 Influence of the magnetogravitational trap on surface oscillations . . .	33
4.3 Computational fluid dynamic simulations . . . . .	40
4.3.1 Governing equations of motion . . . . .	40
4.3.2 Numerical domain . . . . .	41
4.3.3 Numerical initiation of coalescence event . . . . .	42
4.3.4 Evaluation of surface profiles . . . . .	43
4.4 Results . . . . .	43

4.4.1	Satellite bubble ejection . . . . .	43
4.4.2	Time series of spherical harmonics . . . . .	49
4.4.3	Fourier transforms of time series . . . . .	51
4.4.4	Time-frequency analysis of time series . . . . .	54
4.4.5	Viscous damping . . . . .	59
4.4.6	Translational motion of bubbles due to oscillation . . . . .	60
4.5	Summary . . . . .	60
<b>5</b>	<b>Contactless manipulation of bubble clusters</b>	<b>63</b>
5.1	Experimental set-up . . . . .	64
5.2	Results . . . . .	64
5.3	Uses for bubble clusters . . . . .	69
5.4	Summary . . . . .	70
<b>6</b>	<b>Sonomaglev: combining acoustic and diamagnetic levitation</b>	<b>71</b>
6.1	Acoustic levitation . . . . .	72
6.2	Experimental set-up . . . . .	72
6.3	Levitation points of droplets . . . . .	75
6.4	Modelling ultrasonic transducers . . . . .	76
6.4.1	Mathematical model . . . . .	76
6.4.2	Rayleigh-Sommerfeld model . . . . .	77
6.4.3	Matrix method for reflections . . . . .	78
6.4.4	The linear acoustic equation . . . . .	80
6.4.5	Perfectly matched layers . . . . .	81
6.4.6	The finite element method . . . . .	84
6.5	Validating our numerical model . . . . .	85
6.6	Numerical domain . . . . .	89
6.7	Amplitude of acoustic potential . . . . .	89
6.8	Results . . . . .	91
6.8.1	Levitation of multiple droplets . . . . .	91
6.8.2	Visualising ultrasound fields using charged droplet clouds . . . . .	93
6.8.3	Positioning of levitated droplets . . . . .	94
6.8.4	Whispering gallery modes . . . . .	96
6.9	Summary . . . . .	97
<b>7</b>	<b>Conclusions</b>	<b>99</b>
7.1	Chapter review . . . . .	99
7.2	Future work . . . . .	101
7.3	Closing statement . . . . .	103

# Chapter 1

## Introduction

The presence of bubbles and droplets are ubiquitous in our daily lives and play a vital role in many natural and engineering processes. A short list of some of these processes is presented here: the impact of raindrops on surfaces, the ejection of droplets due to the bursting of bubbles at free surfaces, the deposition of ink droplets onto a substrate, the collapse of cavitation bubbles, ocean spray produced from breaking waves and many more. The dynamics of bubbles and droplets play an important role in all these processes, yet in many applications, their dynamics are not yet completely understood.

In many mathematical models of bubbles and droplets, the assumption is made that the shape of the bubbles/droplets under investigation are spherical, as this symmetry allows for the manipulation of the underlying equations governing the dynamics to a state where analytical solutions are more tractable. For this assumption to hold often requires neglecting the effect of several other factors, most notably gravity. In many cases, the effect of gravity has a negligible impact on the problem at hand, but for certain problems neglecting the effect of gravity fundamentally changes the solution. One might assume trying to study such problems is a fruitless endeavour, as experimental validation of such results may appear seemingly out of reach due to the complexity and cost of carrying out such experiments. But the work of this thesis is here to show that alternative methods exist to produce weightless environments, and much progress can be made using these oft-overlooked techniques.

### 1.1 Levitation

Levitation is a fascinating phenomenon, as it appears to directly contradict our intuition of how the world around us should behave. Objects levitating freely in mid-air appear supernatural in nature, or possible only in the fictional worlds of fantasy and sci-fi novels. This has led to many magicians performing astounding tricks demonstrating this seemingly impossible feat. But as with all magic tricks, some element of deception or trickery is necessary. In reality, no deception is needed, as a multitude of levitation techniques have been developed by scientists over the

last century allowing for the free suspension of materials.

These techniques are important in many ways, but as new manned missions to space are being planned and prepared for, these techniques offer alternative methods to study the effect of weightlessness on physical systems and biological organisms. Traditional methods to carry out experiments under weightless conditions are either very expensive, such as installing and carrying out experiments on the international space station; severely time-limited, such as using drop towers where experimentation time is limited to 5 seconds or less; or both, such as performing experiments on parabolic flights. Levitation techniques can offer a cost-effective and preferable way of carrying out experiments in weightless environments [1].

A large number of levitation techniques work by applying surface forces to the object they are levitating, which in turn balances the force of gravity on the object. One such technique is acoustic levitation, which utilises ultrasonic transducers to create pressure fields that apply acoustic radiation forces to objects [2]. A second technique which relies on surface forces to provide levitation is electrostatic levitation. This technique uses time-dependent electric fields to levitate charged objects [3]. Since the charge of a conductor resides purely on its surface, objects levitated in this manner only experience surface forces. If liquid droplets are levitated using such techniques it is often found that the surface of the droplet deforms leading to the flattening of levitated droplets.

The levitation technique which is the main focus of this thesis is diamagnetic levitation. While few materials exhibit ferromagnetism, all ordinary materials exhibit the weaker forms of magnetism, diamagnetism or paramagnetism, meaning they are either repelled by or attracted to magnetic fields. Diamagnetic levitation exploits these weaker forms of magnetism by using strong nonhomogeneous magnetic fields, created by superconducting magnets or large electromagnets, to apply forces large enough to an object to balance that of gravity [4]. Diamagnetic levitation differs from the previous levitation techniques mentioned in that it makes use of body forces induced at a molecular level to support the levitated object against gravity rather than surface forces. Since the force balancing gravity is felt throughout the entirety of the volume of a diamagnetically levitated object, smaller deformations of diamagnetically levitated liquid droplets are observed in comparison to droplets levitated using techniques which rely on surface forces to counteract the force of gravity. A more detailed discussion of diamagnetic levitation will be presented in chapter 2.

## 1.2 Thesis outline

Using the technique of diamagnetic levitation we have been able to conduct a number of novel experiments on bubbles and droplets in weightless environments, as well as developing a new technique building upon diamagnetic levitation, allowing for the levitation and manipulation of multiple spherical droplets. We present the

first experimental confirmation of results predicted by numerical simulations of the ejection of multiple satellite bubbles due to bubble coalescence, as well as compare our findings to previously untested theoretical predictions of the nonlinear surface oscillations of bubbles. To complement our experimental work we also carried out numerical simulations, which have allowed us to gain a deeper understanding of the physical processes we observed experimentally. The outline of this thesis is given below.

In **chapter 2**, we discuss the basic physical principles underpinning diamagnetic levitation. Earnshaw’s theorem is introduced, and we show how a static configuration of charges, masses and magnets with constant magnetisation can never be in static equilibrium. The stability conditions necessary for diamagnetic levitation are then derived and we show how this does not violate Earnshaw’s theorem. Finally we show how the shape of “magnetogravitational” traps can be varied in the bore of superconducting magnets.

In **chapter 3**, we introduce a new technique for levitating spherical gas bubbles in liquids at room temperature. We then present the experimental set-up we have used to conduct all experiments on diamagnetically levitated air bubbles discussed in this thesis.

In **chapter 4** we investigate the nonlinear axisymmetric surface oscillations of bubbles. Bubble coalescence is used to introduce a large axisymmetric perturbation to the system. We analyse two cases: a symmetric case, where the initial parent bubbles have equal radii (within experimental error) and an asymmetric case where the ratio of the radii of the two parent bubbles is  $\sim 1.5$ . We compare our experiments and simulations to the theoretical model of Tsamopoulos and Brown [5] by decomposing the surface of the bubble into spherical harmonics, which allows us to observe the shift in frequency for 2nd and 3rd degree shape modes and analyse the coupling between different shape modes.

In **chapter 5** we build upon the technique demonstrated in chapter 3 and present a method to create clusters of spherical levitated air bubbles. We show how to alter the structure of these bubble clusters via non-contact manipulation, by altering the current in the superconducting solenoid coil used to levitate the bubbles. Bubble clusters of up to 19 similarly sized bubbles are demonstrated and multiple configurations of these clusters are shown. We then proceed to discuss possible future uses for bubble clusters.

In **chapter 6**, we present a new experimental technique combining acoustic and diamagnetic levitation. We present our experimental set-up and demonstrate how this technique is able to take advantage of the strengths of both acoustic levitation and diamagnetic levitation to overcome weaknesses of each individual technique. We then compare our experimental results to numerical simulations, demonstrating that we are able to predict accurately the positions of levitated droplets. We then identify some ways in which the future development of this technique expands the toolset available to researchers looking to study systems in weightless environments.

In **chapter 7**, we review the work and findings presented throughout all previous

chapters. We then discuss the prospect of future research building upon the work of this thesis.

# Chapter 2

## Principles of diamagnetic levitation

In his review article ‘levitation in physics’ Brandt remarks that diamagnetic levitation seems to be of no more than academic interest [6]. Though this may have seemed true to him at the time of writing, over the last three decades diamagnetic levitation has proven to be a markedly useful technique. Diamagnetic levitation has been used to study a wide variety of problems in weightless or differential gravity environments, such as the response of biological organism (e.g. fruit flies [7], *Xenopus laevis* embryos (frog eggs) [8], yeast and single celled organisms such as bacteria [9] and protists [10]), protein growth [11], separation of granular mixtures [12], surface oscillations of Newtonian and non-Newtonian fluids [13]–[15], the shape of rotating droplets [16], [17], surface instabilities in multiphase fluid flows [18], [19] and tektite formation [20]. In this chapter we present the underlying physics explaining how materials may be stably levitated using diamagnetic levitation and the experimental set-up we used to achieve this.

### 2.1 A brief history of diamagnetic levitation

The possibility of diamagnetic levitation was first realised in the 1870’s by Lord Kelvin [21]. Lord Kelvin showed that a diamagnetic material placed in a magnetic field was capable of possessing minima in its energy and hence suggested the possibility of stable levitation of diamagnetic objects [22]. This theoretical result was not proven experimentally until 1939 by Braunbeck, who was working on the problem of static levitation [23], [24]. Braunbeck demonstrated that electrostatic levitation was possible for materials of relative permittivity  $\epsilon < 1$  and magnetostatic levitation was possible for materials of relative permeability  $\mu < 1$  (which is the condition that the material must be diamagnetic). Owing to the belief at the time that there existed no material with the physical property  $\epsilon < 1$ , Braunbeck concluded that only magnetostatic levitation was possible and managed to demonstrate this phenomena by levitating small particles of graphite and bismuth in the bore of a solenoid magnet.

Diamagnetic levitation was then largely forgotten for the rest of the 20th century. Only a handful of experiments were still carried out: reproducing Braunbeck's results using permanent magnets [25], the levitation of pyrolytic graphite [26], and studying the motion of diamagnetically levitated particles [27]. Diamagnetic levitation reemerged from relative obscurity with the work of Beaugnon and Tournier [28], who demonstrated levitation of water and organic materials, Berry and Geim [4] and Valles Jr *et al.* [8] who demonstrated levitation of living organisms, and Paine and Seidel [29] and Weilert *et al.* [30] who demonstrated the levitation of liquid hydrogen and liquid helium, respectively. Since then a larger community of researchers have taken up this technique to enable the study of a diverse array of phenomena in pseudo-weightless conditions.

## 2.2 Earnshaw's theorem

Diamagnetic levitation is simple in principle: since diamagnetic objects feel a repulsive force when placed in a magnetic field it can be assumed that this repulsive force could be used to balance other forces on an object such as gravity and hence allow us to levitate objects. Although this is true, it is not as trivial as it first seems. Repulsion is also seen in bar magnets, but it is known to us from childhood that it is seemingly impossible to stably levitate one magnet on top of another. This is due to Earnshaw's theorem which states that no stationary configuration of magnets with constant magnetisation, charges and masses can be in static equilibrium [22]. This can be shown by considering a time-independent gravitational/electric/magnetic field given by  $\mathbf{f}$ . A point in free space within such a field satisfies

$$\nabla \cdot \mathbf{f} = 0, \quad \nabla \times \mathbf{f} = \mathbf{0}. \quad (2.1)$$

Therefore we may describe  $\mathbf{f}$  as the gradient of some potential

$$\mathbf{f} = -\nabla\phi, \quad (2.2)$$

hence

$$\nabla^2\phi = 0. \quad (2.3)$$

For masses and electric charges, the potential energy  $U$ , of a point mass/charge placed in a gravitational/electric field is proportional to the potential of the field  $\phi$ , therefore

$$\nabla^2U = 0. \quad (2.4)$$

For a magnetic dipole, the energy of a magnet of constant magnetisation, with magnetic moment  $\mathbf{m}$ , placed in a magnetic field is given by

$$U = -\mathbf{m} \cdot \mathbf{f}, \quad (2.5)$$

hence

$$\nabla^2U = -\mathbf{m} \cdot \nabla^2\mathbf{f}. \quad (2.6)$$

The Laplacian of the energy in this case can also be shown to be zero by combining the equations from (2.1) with the identity

$$\nabla^2 \mathbf{A} = \nabla(\nabla \cdot \mathbf{A}) - \nabla \times (\nabla \times \mathbf{A}). \quad (2.7)$$

It is known that a necessary but not sufficient stability criteria for a stable equilibrium point is given by

$$\nabla^2 U > 0, \quad (2.8)$$

which can't be satisfied by any of the systems described above, therefore no static system made of purely masses, point charges and magnets can remain in stable equilibrium. Earnshaw's theorem proves magnetic levitation is impossible for stationary materials of constant magnetisation. Diamagnetic materials are not subjected to Earnshaw's theorem because the magnetisation in this case is proportional to the applied magnetic field, i.e.  $\mathbf{m}$  is not constant.

## 2.3 Diamagnetic levitation

Diamagnetic levitation is a phenomenon in which a diamagnetic object is suspended against the force of gravity by magnetic forces due to an inhomogeneous magnetic field. If we take into account the fluid surrounding the object, an identical situation exists, except the object is suspended against buoyancy forces. When this external fluid is taken into consideration the technique is often referred to as magneto-Archimedes levitation, but for the rest of this thesis we shall simply refer to both techniques as diamagnetic levitation [31].

We shall now show theoretically, following closely the work of Berry and Geim [4] altering their derivation to account for an additional surrounding fluid, how objects may be stably levitated using diamagnetic levitation.

Let us consider an object of density  $\rho_1$  and magnetic susceptibility  $\chi_1$  placed in a magnetic field  $\mathbf{B}(\mathbf{r})$  and surrounded by a fluid of density  $\rho_2$  and magnetic susceptibility  $\chi_2$ . Here  $\mathbf{r}$  is the position vector. We shall only consider substances with  $|\chi| \ll 1$ , therefore to a good approximation the magnetic moment of an object of volume  $V$  is given by

$$\mathbf{m}(\mathbf{r}) = \int_V \frac{(\chi_1 - \chi_2)\mathbf{B}(\mathbf{r})}{\mu_0} dV. \quad (2.9)$$

By integrating the work done  $-\mathbf{dm} \cdot \mathbf{B}$  as the magnetic field is increased from zero to  $B(\mathbf{r}) = |\mathbf{B}(\mathbf{r})|$ , we obtain the magnetic energy  $u_{mag}$ , of the object, hence

$$\begin{aligned} u_{mag}(\mathbf{r}) &= - \int_V \int \mathbf{B} \cdot d\mathbf{m} dV \\ &= - \int_V \frac{(\chi_1 - \chi_2)}{2\mu_0} B^2(\mathbf{r}) dV. \end{aligned} \quad (2.10)$$

If we account for buoyancy forces this gives the total energy of the object

$$u(\mathbf{r}) = \int_V \left[ \Delta\rho gz - \frac{\Delta\chi}{2\mu_0} B^2(\mathbf{r}) \right] dV, \quad (2.11)$$

where  $g$  is the acceleration due to gravity,  $z$  is the coordinate directed anti-parallel to the direction of gravity,  $\Delta\rho = \rho_1 - \rho_2$  and  $\Delta\chi = \chi_1 - \chi_2$ . We will assume the volume of the object is small such that the magnetic and gravitational energy varies slowly throughout the domain of the object. Therefore it is reasonable to assume the contents of the integral in equation (2.11) are constant in the domain  $V$ , hence the energy equation may be rewritten as

$$u(\mathbf{r}) = \Delta\rho Vgz - \frac{\Delta\chi V}{2\mu_0} B^2(\mathbf{r}). \quad (2.12)$$

For the object to be levitating the net force on the object must be zero, hence

$$\mathbf{F}(\mathbf{r}) = -\nabla u(\mathbf{r}) = -\Delta\rho Vg\hat{\mathbf{z}} + \frac{\Delta\chi V}{\mu_0} B(\mathbf{r})\nabla B(\mathbf{r}) = 0, \quad (2.13)$$

where  $\hat{\mathbf{z}}$  is the unit vector in the direction opposite to that of gravity. Therefore equilibrium points must satisfy the following equation

$$B(\mathbf{r})\nabla B(\mathbf{r}) = \frac{\mu_0 g \Delta\rho}{\Delta\chi} \hat{\mathbf{z}}. \quad (2.14)$$

### 2.3.1 Stability conditions

For an equilibrium point to be stable we require the energy to be a minimum at that point, meaning

$$\nabla^2 u(\mathbf{r}) = -\frac{\Delta\chi V}{2\mu_0} \nabla^2 B^2(\mathbf{r}) > 0. \quad (2.15)$$

But since

$$\nabla^2 B^2(\mathbf{r}) = \nabla^2 (B_x^2 + B_y^2 + B_z^2) \quad (2.16)$$

$$= 2[|\nabla B_x|^2 + |\nabla B_y|^2 + |\nabla B_z|^2] \quad (2.17)$$

$$+ B_x \nabla^2 B_x + B_y \nabla^2 B_y + B_z \nabla^2 B_z], \quad (2.18)$$

using the fact  $\nabla \times \mathbf{B}(\mathbf{r}) = 0$  we can show

$$\nabla^2 B^2(\mathbf{r}) = 2[|\nabla B_x|^2 + |\nabla B_y|^2 + |\nabla B_z|^2 + \mathbf{B}(\mathbf{r}) \cdot \nabla(\nabla \cdot \mathbf{B}(\mathbf{r}))], \quad (2.19)$$

and since  $\nabla \cdot \mathbf{B}(\mathbf{r}) = 0$  we can write

$$\nabla^2 B^2(\mathbf{r}) = 2[|\nabla B_x|^2 + |\nabla B_y|^2 + |\nabla B_z|^2] \geq 0. \quad (2.20)$$

From this it follows that  $\Delta\chi < 0$  is required for an equilibrium point to be stable, which is equivalent to  $\chi_1 < \chi_2$ . Hence the magnetic susceptibility of the outer fluid

must be greater than that of the object. In other words, it is possible to levitate a paramagnetic object as long as it is surrounded by a fluid that is more paramagnetic [31].

The above condition is a necessary condition for stability but not a sufficient condition. The sufficient conditions for stability are given by

$$\frac{\partial^2 u(\mathbf{r})}{\partial x^2} > 0, \quad \frac{\partial^2 u(\mathbf{r})}{\partial y^2} > 0, \quad \frac{\partial^2 u(\mathbf{r})}{\partial z^2} > 0, \quad (2.21)$$

which enforces that the force in every direction must decrease as an object is moved towards an equilibrium point. If the assumption is made  $\Delta\chi < 0$  then the stability criteria (2.21) reduces to

$$\frac{\partial^2 B^2(\mathbf{r})}{\partial x^2} > 0, \quad \frac{\partial^2 B^2(\mathbf{r})}{\partial y^2} > 0, \quad \frac{\partial^2 B^2(\mathbf{r})}{\partial z^2} > 0. \quad (2.22)$$

### 2.3.2 Stable zones of rotationally symmetric magnetic fields

In all the experimental work presented throughout this thesis we use superconducting solenoids to create magnetic fields. The cylindrical symmetry of these solenoids leads to magnetic fields that are rotationally symmetric about the vertical axis ( $z$ ) of the solenoid. Stable levitation points may only exist on the central axis of the solenoid. Due to this constraint, it is possible to identify zones of stable levitation expressed in terms of the vertical component of the magnetic field and its derivatives [4].

To begin, we introduce the magnetic potential in terms of the radial and vertical coordinates ( $r, z$ ), as

$$\mathbf{B}(r, z) = \nabla\Phi(r, z), \quad (2.23)$$

where we define the magnetic potential on the vertical axis to be

$$\Phi_0(z) = \Phi(0, z). \quad (2.24)$$

We may approximate the magnetic potential close to the vertical axis using a Taylor expansion

$$\Phi(r, z) = \Phi_0(z) + r \frac{\partial\Phi(0, z)}{\partial r} + \frac{r^2}{2} \frac{\partial^2\Phi(0, z)}{\partial r^2} + O(r^3). \quad (2.25)$$

We make the distinction between  $\frac{\partial^n\Phi_0(z)}{\partial r^n}$ , where  $\Phi_0(z)$  is a function of  $z$  only, hence  $\frac{\partial^n\Phi_0(z)}{\partial r^n} = 0$  and  $\frac{\partial^n\Phi(0, z)}{\partial r^n}$ , which is the  $n$ th derivative of the function  $\Phi(r, z)$  with respect to  $r$  evaluated at  $z = 0$ . Due to the cylindrical symmetry, the radial component of the magnetic field on axis must be zero

$$B_r(0, z) = \frac{\partial\Phi(0, z)}{\partial r} = 0, \quad (2.26)$$

hence the second term in the Taylor expansion of equation (2.25) vanishes.

By noting that  $\nabla \cdot \mathbf{B} = 0$  it is clear that the magnetic potential must satisfy Laplace's equation. We can use Laplace's equation and equation (2.25) to show that

$$\Phi_0''(z) = -2 \frac{\partial^2 \Phi(0, z)}{\partial r^2}, \quad (2.27)$$

where the primes denote differentiation with respect to  $z$ . Therefore, we may rewrite equation (2.25) in the form

$$\Phi(r, z) = \Phi_0(z) - \frac{r^2}{4} \Phi_0''(z) + O(r^3). \quad (2.28)$$

We shall now define the on-axis magnetic field-strength to be given by

$$\tilde{B}(z) = \Phi_0'(z). \quad (2.29)$$

By combining equations (2.23), (2.25) and (2.29) the following expression for the square of the magnetic field may be obtained

$$B^2(r, z) = \tilde{B}(z)^2 + \frac{r^2}{4} (\tilde{B}'(z)^2 - 2\tilde{B}(z)\tilde{B}''(z)) + O(r^4). \quad (2.30)$$

We shall now return to the necessary stability conditions given by equation (2.22). Applying rotational symmetry, these equations may be expressed in terms of the radial and vertical coordinates as

$$\frac{\partial^2 B^2(\mathbf{r})}{\partial r^2} > 0, \quad \frac{\partial^2 B^2(\mathbf{r})}{\partial z^2} > 0. \quad (2.31)$$

Inserting (2.30) into the stability conditions we may express the stability conditions in terms of the on axis magnetic field strength

$$\begin{aligned} D_v(z) &\equiv \tilde{B}'(z)^2 + \tilde{B}(z)\tilde{B}''(z) > 0 && \text{(vertical stability)} \\ D_h(z) &\equiv \tilde{B}'(z)^2 - 2\tilde{B}(z)\tilde{B}''(z) > 0 && \text{(horizontal stability)} \end{aligned} \quad (2.32)$$

It was demonstrated by Berry and Geim that these stability conditions are satisfied in the bore of a solenoid magnet [4]. To show this we will consider a rotationally symmetric solenoid of length  $L$  and radius  $a$ . We begin by defining the non-dimensional aspect ratio, the ratio of the diameter of the solenoid to the length of the solenoid

$$\delta = \frac{2a}{L}, \quad (2.33)$$

and non-dimensional coordinate

$$\zeta = \frac{z}{L}. \quad (2.34)$$

Using the Biot-Savart law an analytical expression for the on-axis magnetic field strength may be obtained under the approximation that the coils of the solenoid are infinitesimally thin

$$\tilde{B}(\zeta) = \frac{B_0}{2} \sqrt{1 + \delta^2} \left( \frac{1 + 2\zeta}{\sqrt{(1 + 2\zeta)^2 + \delta^2}} + \frac{1 - 2\zeta}{\sqrt{(1 - 2\zeta)^2 + \delta^2}} \right). \quad (2.35)$$

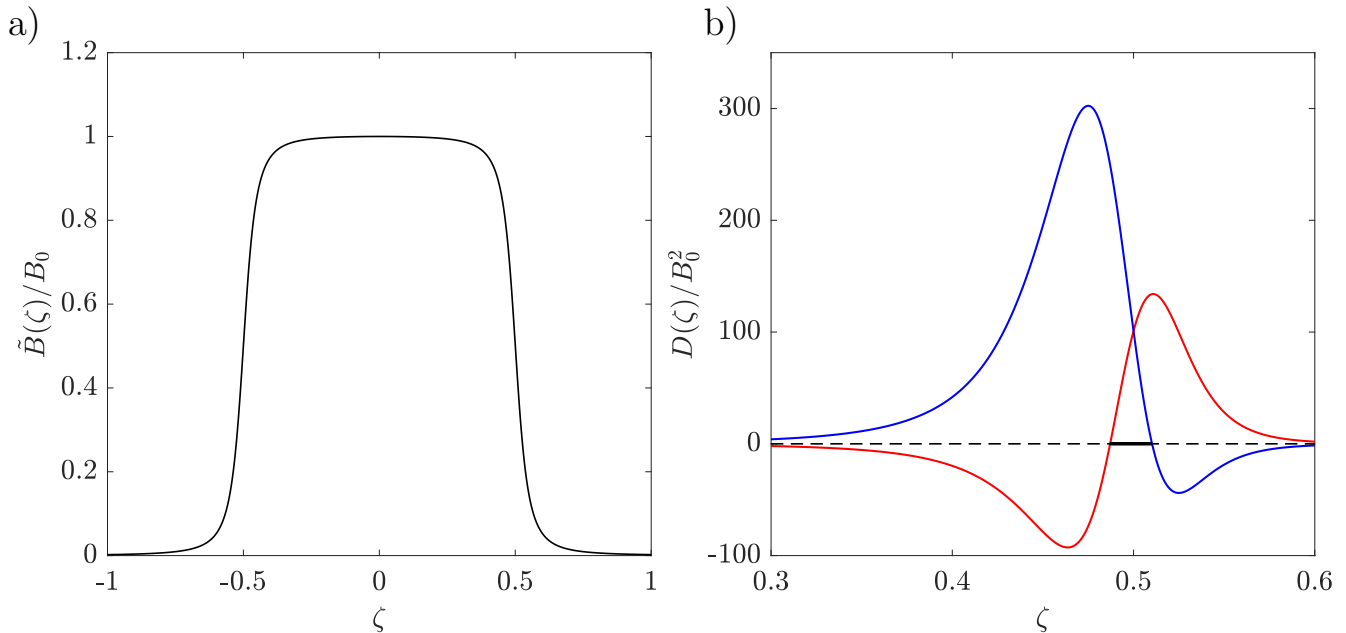


Figure 2.1: a) Plot of the normalised on-axis magnetic field strength for aspect ratio  $\delta = 0.1$ . b) Plots of the stability conditions for the magnetic field presented in a). The horizontal stability condition is displayed in blue and the vertical stability condition is displayed in red. The stable zone where both  $D_h(\zeta) > 0$  and  $D_v(\zeta) > 0$  is indicated by the solid black line between  $0.487 < \zeta < 0.510$ .

Here,  $B_0$  is the magnetic field at  $z = 0$  for a given fixed current through the solenoid.

Figure 2.1a shows a plot of the non-dimensional magnetic field strength against vertical height and 2.1b shows a plot of the stability conditions for  $\delta = 0.1$ . For  $\delta = 0.1$  the stable zone is found to lie between  $0.487 < \zeta < 0.510$  as indicated in plot 2.1b. It should be noted that the expression for the on-axis magnetic field (2.35) is an even function, meaning both stability conditions  $D_v$  and  $D_h$  shown in figure 2.1b are also even, hence a second stable zone exists at  $-0.510 < \zeta < -0.487$ . We note stable zones are a necessary but not sufficient condition for stable levitation, as discussed earlier.

For an object to be diamagnetically levitated there must exist an equilibrium point satisfying equation (2.14) within one of the stability zones. As the location of the stability zones are only dependent on the geometry of the solenoid and entirely independent of  $B_0$ , this can be achieved by adjusting the current in the solenoid, as this scales the magnetic field strength whilst also preserving the geometry of the field lines.

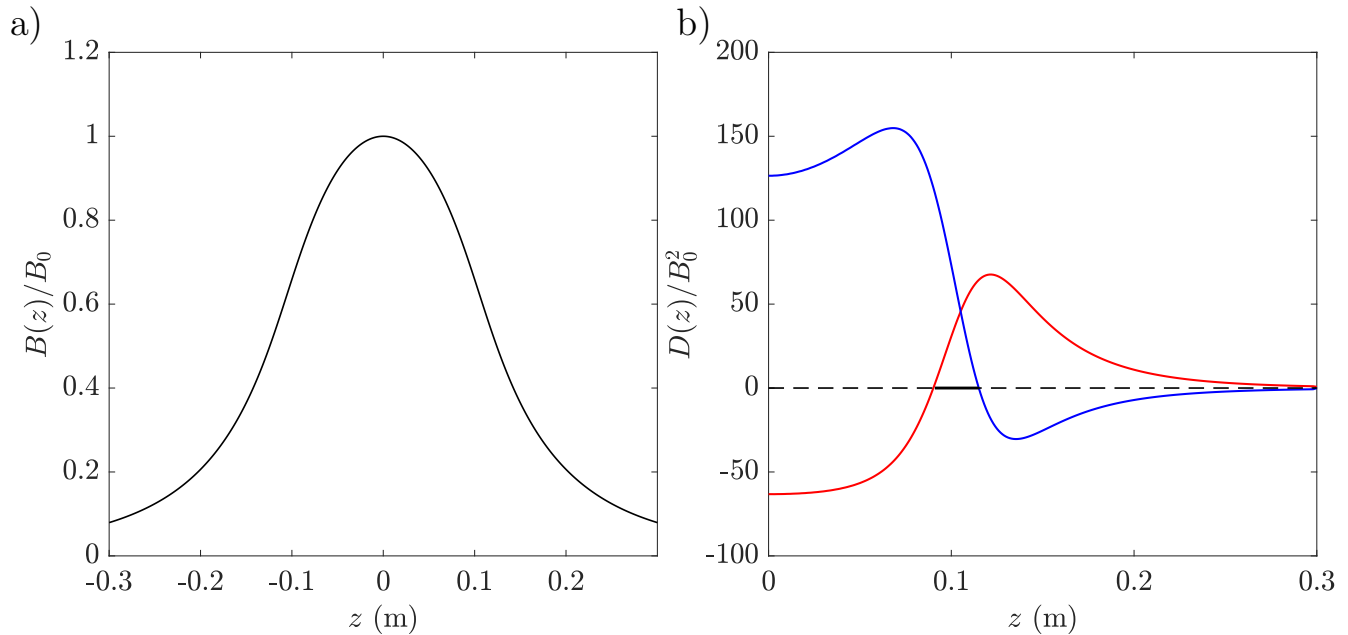


Figure 2.2: a) Plot of the normalised on-axis magnetic field strength for the Cryogenic Ltd magnet. b) Plots of the stability conditions for the magnetic field presented in a). As in figure 2.1b, the horizontal stability condition is displayed in blue and the vertical stability condition is displayed in red. The stable zone where both  $D_h(z) > 0$  and  $D_v(z) > 0$  is indicated by the solid black line between  $0.0902 \text{ m} < z < 0.115 \text{ m}$ .

## 2.4 Cryogenic superconducting magnet

The experiments described throughout this thesis were performed using a custom-designed superconducting magnet manufactured by Cryogenic Ltd. The magnet has a bore diameter of 58 mm, a maximum field strength of 18.5 T and is able to produce a maximum field gradient product ( $BdB/dz$ ) of  $\pm 1640 \text{ T}^2 \text{ m}^{-1}$ . The magnet is constructed from three concentric solenoidal windings using a cryogen free design, meaning the solenoid coils are placed within a vacuum rather than being in direct contact with coolants, such as liquid helium or liquid nitrogen. Although, gaseous helium is still required to cool the system down to approximately 4 K, so the coils remain below their superconducting transition temperature. The lengths of the inner, central and outer coils are 21 cm, 20 cm and 18 cm respectively. The inner and central windings are constructed from  $\text{Nb}_3\text{Sn}$  and the outer winding is constructed from  $\text{NbTi}$ , where all the coils are connected in series. To insulate the system from external radiation a high purity aluminium radiation shield is situated around the magnet.

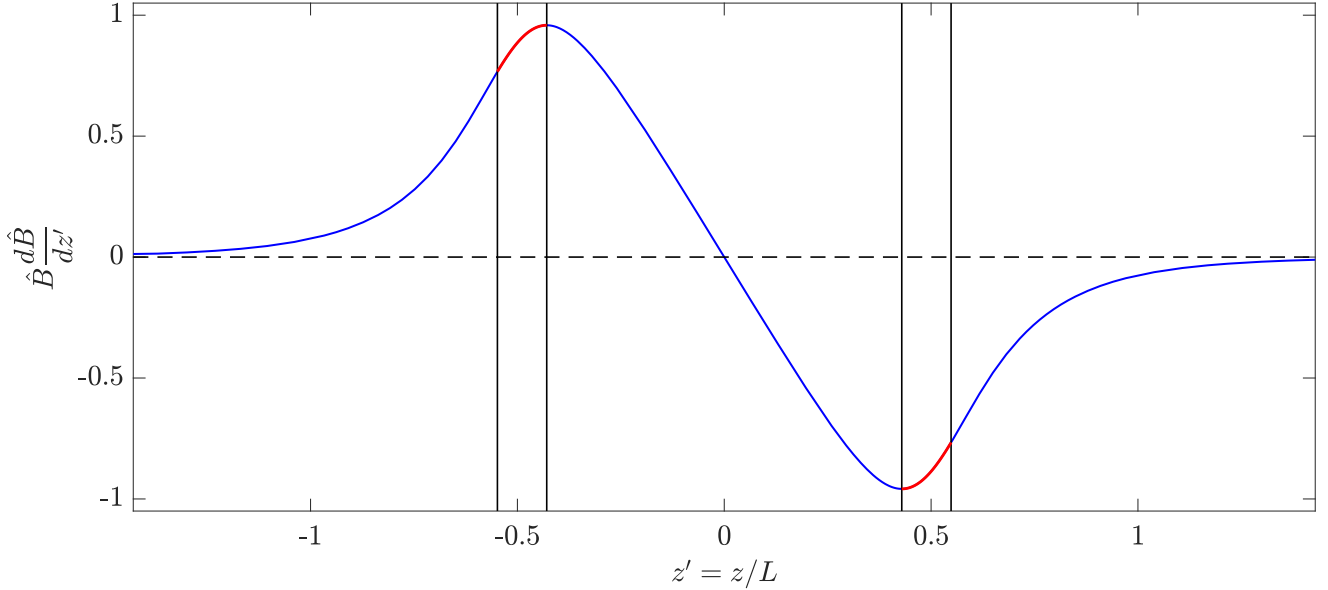


Figure 2.3: Plot of the field gradient product as function of vertical distance from the center of the solenoid for the cryogenic magnet. Regions in red denote the range of values that lie within the stable levitation zones, denoting the range of values  $\kappa$  may take.

## 2.5 Shape of magnetogravitational potential traps

The stable zone for the cryogenic magnet is  $0.090 \text{ m} < z < 0.115 \text{ m}$ , as shown in figure 2.2. As before, due to the symmetry of the magnetic field a second stable zone also exists at  $-0.115 \text{ m} < z < -0.090 \text{ m}$ . Therefore, there exists a range of heights at which objects may be stably levitated, but this is not the whole picture, as the magnetogravitational potential around the stable levitation point varies depending on the vertical location of the stable levitation point.

We shall define the non-dimensional magnetic field to given by

$$\hat{B}(\mathbf{r}) = B(\mathbf{r})/B_0. \quad (2.36)$$

This allows for equation (2.14) to be rewritten as

$$\begin{aligned} \hat{B}(\mathbf{r}') \nabla' \hat{B}(\mathbf{r}') &= \kappa \hat{\mathbf{z}}, \\ \kappa &\equiv \frac{\mu_0 g \Delta \rho L}{\Delta \chi B_0^2}, \end{aligned} \quad (2.37)$$

where here length has been non-dimensionalised by  $L$ , the length of the inner coil, i.e.  $z = z'L$  and  $r = r'L$ . Since the stability zones are only dependent on  $\hat{B}(\mathbf{r})$ , the introduction of the constant  $\kappa$  gives a single non-dimensional parameter that defines

the shape of the magnetogravitational potential for a given magnetic field geometry, central field strength and physical characteristics of the fluid and levitated object. Returning to cylindrical solenoids, equilibrium points may only lie on the central axis of such solenoids due to their rotational symmetry, as previously mentioned in section 2.3.2. Hence, equilibrium points for cylindrical solenoids satisfy the equation

$$\hat{B}(0, z') \frac{d\hat{B}(0, z')}{dz'} = \kappa, \quad (2.38)$$

where it can be shown that

$$\text{sgn} \left( \hat{B}(0, z') \frac{d\hat{B}(0, z')}{dz'} \right) = -\text{sgn}(z'). \quad (2.39)$$

For a stable equilibrium point  $z_0$ , that lies within a stable zone, if  $z_0 > 0$ , then  $\kappa < 0$  and conversely if  $z_0 < 0$ , then  $\kappa > 0$ . The sign of  $\kappa$  is entirely dependent on  $\Delta\rho$ , since it is a necessary condition for the existence of stable equilibrium points that  $\Delta\chi < 0$  (see section 2.3.1). Therefore, only objects that are denser than the surrounding fluid may stably levitate above the centre of the solenoid and only objects that are less dense than the surrounding fluid they are suspended in may stably levitate below the centre of the solenoid.

For the Cryogenic magnet, the range of values  $\kappa$  may take is  $-0.9584 < \kappa < -0.7665$  and  $0.7665 < \kappa < 0.9584$  respectively, see figure 2.3. Figures 2.4 and 2.5 display magnetogravitational contour plots for the Cryogenic magnet for these two ranges of  $\kappa$ . From these two figures the height of stable levitation point is observed to vary as a function of  $\kappa$ , but also the shape of the magnetogravitational potential varies as a function of  $\kappa$ . It is clear by comparing figures 2.4 and 2.5 and observing the symmetry across  $z = 0$  in figure 2.3 that reversing the sign of  $\kappa$  has the effect of reflecting the magnetogravitational across the  $z = 0$  plane. So from now on we will only refer to  $|\kappa|$  when discussing the magnetogravitational potential.

From the contour plots in figures 2.4 and 2.5 we can see that the spatial gradient of the magnetogravitational potential and hence the restoring force on an object is not equal in all directions. In figure 2.4f contours are wider in the radial direction than in the vertical direction. Hence, the potential varies more slowly in the radial direction in comparison to the vertical direction, so objects placed in the stable levitation point feel a stronger restoring force if perturbed in the vertical direction than if they were perturbed radially.

We shall refer to the shape of these contours around the stable levitation point as the shape of the magnetogravitational potential trap. Figures 2.7 and 2.6 show the magnetogravitational potential as a function of vertical and horizontal position respectively, where we define  $u_0 = u(0, 0, z_0)$ . These figures are to elucidate how the depth of the magnetogravitational potential well, contour plots of which are displayed in figure 2.4, varies as a function of  $|\kappa|$ . Initially, for  $|\kappa| = 0.945$ , the depth of the potential well is very shallow in the vertical direction and much deeper in the

horizontal direction, leading to a tear-drop shaped magnetogravitational potential trap (see figure 2.4a). But as  $|\kappa|$  decreases, the depth of the potential well deepens in the vertical direction but decreases in the horizontal direction. The potential well also widens in the horizontal direction as  $|\kappa|$  decreases, leading to the shape of the magnetogravitational potential trap taking a shape similar to that of a thin oblate spheroid (see figure 2.4g-i).

In certain situations, such as when observing the surface oscillations of droplets or bubbles, it is preferable to make the magnetogravitational potential trap as spherical as possible. To analyse the sphericity of the trap it is helpful to express the magnetogravitational potential in terms of a multipole expansion about the stable equilibrium point, hence

$$u = u_0 + \sum_{n=0} \sum_{m=0} c_{n,m}(r) Y_n^m(\theta, \phi), \quad (2.40)$$

where we have used the spherical coordinate system  $(r, \theta, \phi)$  centered at the stable equilibrium point and  $Y_n^m(\theta, \phi)$  is a spherical harmonic of degree  $n$  and order  $m$ . Owing to the cylindrical symmetry of the magnetogravitational potential, terms of order  $m \neq 0$  vanish. Therefore we may express the magnetogravitational as a sum of Legendre polynomials

$$u = u_0 + \sum_{n=0} c_n(r) P_n(\cos(\theta)), \quad (2.41)$$

where  $P_n(x)$  is a Legendre polynomial of order  $n$  and argument  $x$ . Here, as in the rest of this thesis, we shall take axisymmetric spherical harmonics to be given by  $Y_n^0(\theta, \phi) = P_n(\cos(\theta))$ , where  $P_n(1) = 1$ .

For a perfectly spherical magnetogravitational potential trap the coefficients  $c_n(r) = 0$  for  $n \neq 0$ . Figure 2.8 displays these coefficients for the cryogenic magnet for the magnetogravitational potentials displayed in figure 2.4. From these plots and figure 2.9 it can be seen that even degree coefficients, other than  $n = 0$ , vary more rapidly as a function of  $|\kappa|$  than odd degree coefficients. From figure 2.9 it can be further seen that the only terms that have coefficients that may be comparable or larger in size to the monopole ( $n = 0$ ) term are other even terms, but these terms can be minimised by adjusting  $|\kappa|$ . If even terms are minimised the next greatest contribution comes from the octupole ( $n = 3$ ) term, the magnitude of all other odd terms can be seen to be less than the octupole term. The contribution of the octupole term may be minimised by adjusting  $|\kappa|$ , but this leads to increased contribution from the even terms.

Hence, to increase the sphericity of the magnetogravitational trap we chose to minimise the quadrupole ( $n = 2$ ) term, which also leads to decreasing the contribution of all other even terms, but slightly increasing the contribution of all odd terms. To do this we minimise the integral

$$I = \int_0^R |c_2(r; \kappa)| dr. \quad (2.42)$$

It can be seen that  $\lim_{r \rightarrow \infty} |c_n(r)| = \infty$ , hence  $I$  is unbounded in the limit  $R \rightarrow \infty$ . Therefore, we chose a range  $(0 \rightarrow R)$  over which we wish to minimise the the quadrupole contribution. From this operation we obtain a value of  $|\kappa| = 0.9387$  for  $R = 25$  mm for the cryogenic magnet. Figure 2.10 displays a contour plot of the magnetogravitational potential and a plot of the multipole coefficients of the magnetogravitational potential for this value of  $|\kappa|$ . Although the quadrupole coefficient is not zero for the entire range of  $r = 0 - 25$  mm it is well approximated by  $c_2(r) \approx 0$  in comparison to all other coefficients, see figure 2.10b.

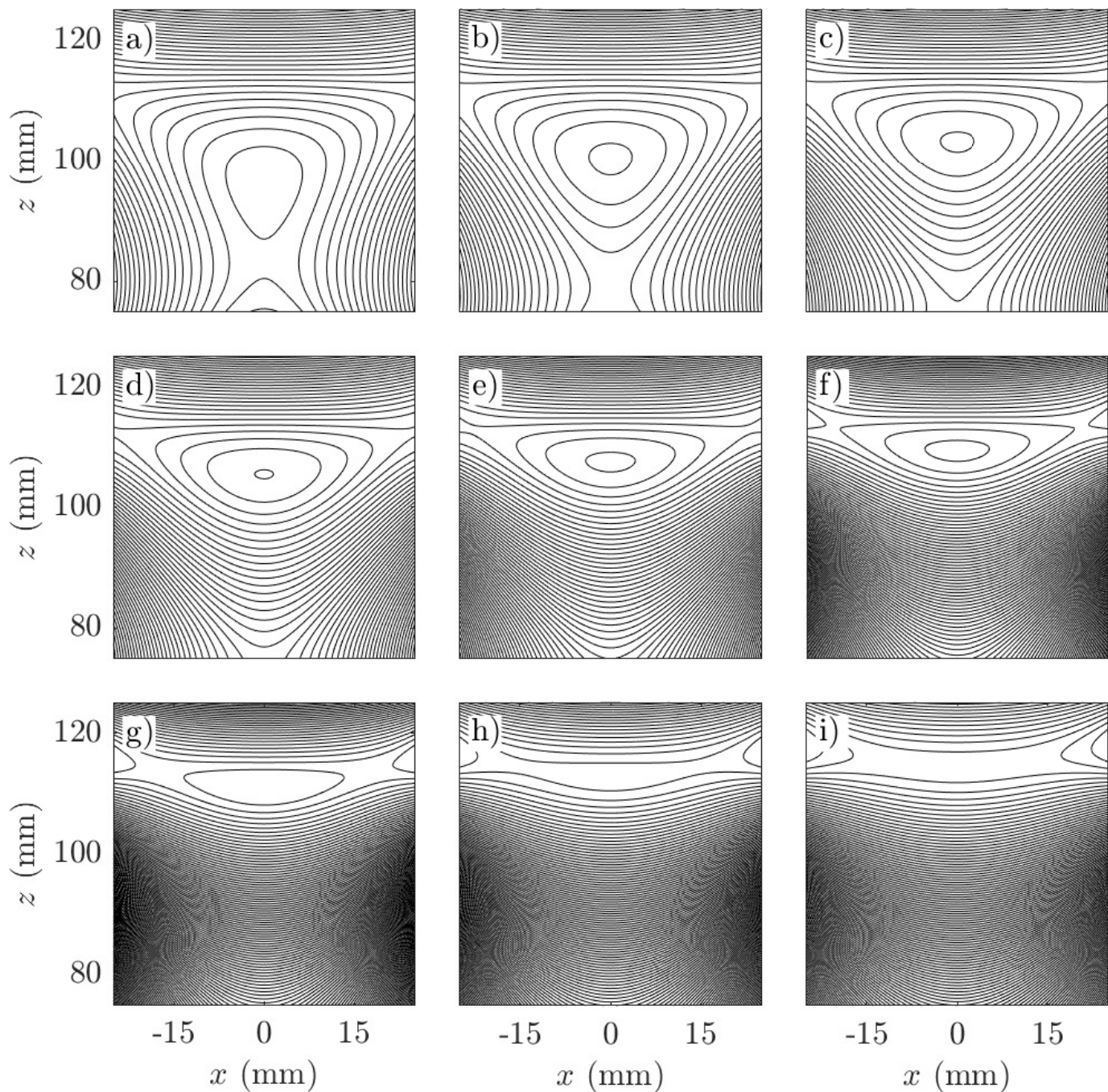


Figure 2.4: Contour plots of the magnetogravitational potential inside the bore of the cryogenic magnet for  $\kappa < 0$ . a)  $\kappa = -0.945$ , b)  $\kappa = -0.924$ , c)  $\kappa = -0.903$ , d)  $\kappa = -0.882$ , e)  $\kappa = -0.861$ , f)  $\kappa = -0.84$ , g)  $\kappa = -0.819$ , h)  $\kappa = -0.798$  and i)  $\kappa = -0.777$

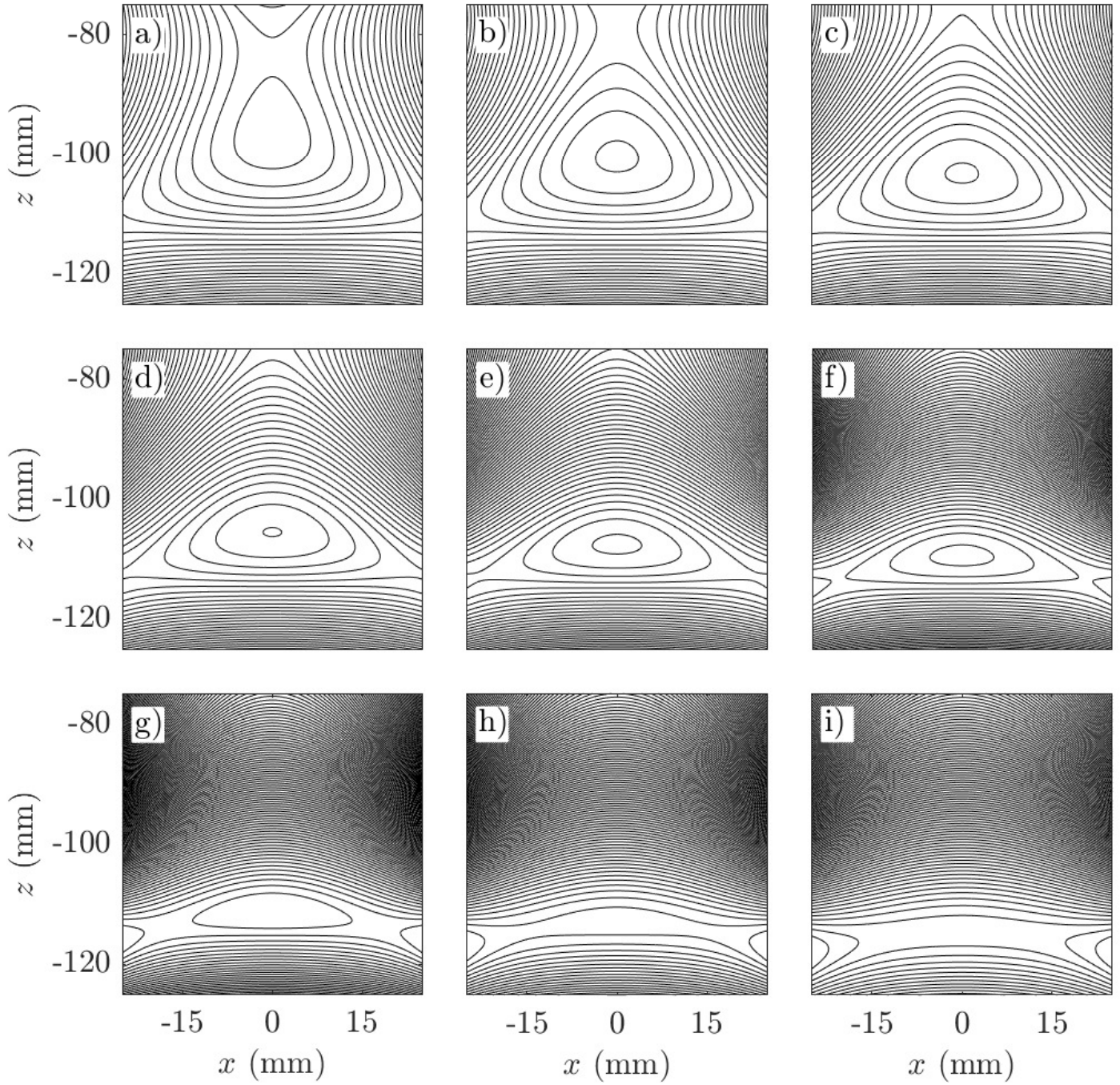


Figure 2.5: Contour plots of the magnetogravitational potential inside the bore of the cryogenic magnet for  $\kappa > 0$ . a)  $\kappa = 0.945$ , b)  $\kappa = 0.924$ , c)  $\kappa = 0.903$ , d)  $\kappa = 0.882$ , e)  $\kappa = 0.861$ , f)  $\kappa = 0.84$ , g)  $\kappa = 0.819$ , h)  $\kappa = 0.798$  and i)  $\kappa = 0.777$

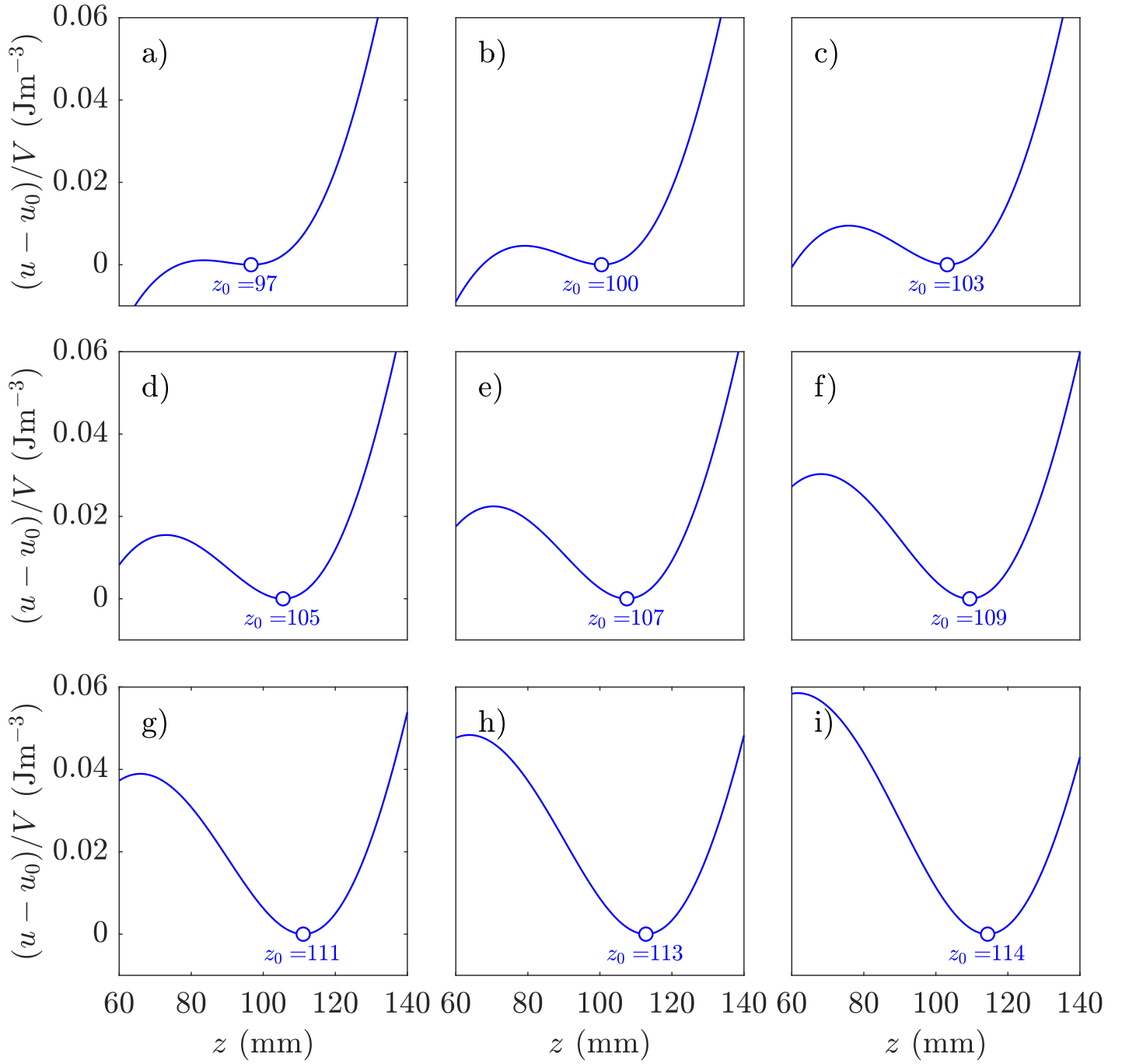


Figure 2.6: Energy density as a function of vertical position.  $z_0$  is the vertical coordinate of the stable equilibrium point and  $u_0$  is the corresponding magnetogravitational potential at  $z_0$ . a)  $\kappa = -0.945$ , b)  $\kappa = -0.924$ , c)  $\kappa = -0.903$ , d)  $\kappa = -0.882$ , e)  $\kappa = -0.861$ , f)  $\kappa = -0.84$ , g)  $\kappa = -0.819$ , h)  $\kappa = -0.798$  and i)  $\kappa = -0.777$

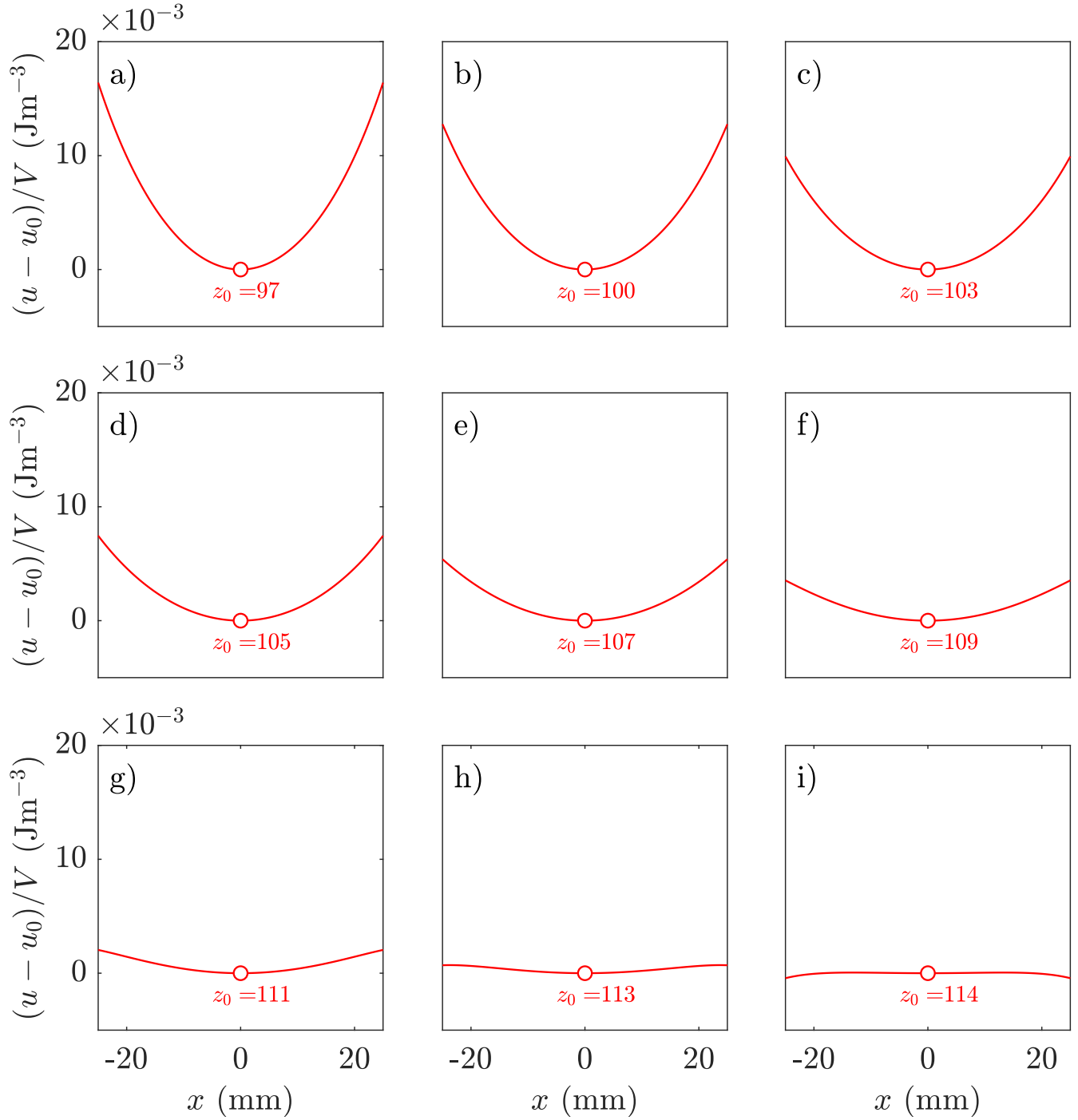


Figure 2.7: Energy density as a function of horizontal position.  $z_0$  is the vertical coordinate of the stable equilibrium point and  $u_0$  is the corresponding magnetogravitational potential at  $z_0$ . a)  $\kappa = -0.945$ , b)  $\kappa = -0.924$ , c)  $\kappa = -0.903$ , d)  $\kappa = -0.882$ , e)  $\kappa = -0.861$ , f)  $\kappa = -0.84$ , g)  $\kappa = -0.819$ , h)  $\kappa = -0.798$  and i)  $\kappa = -0.777$

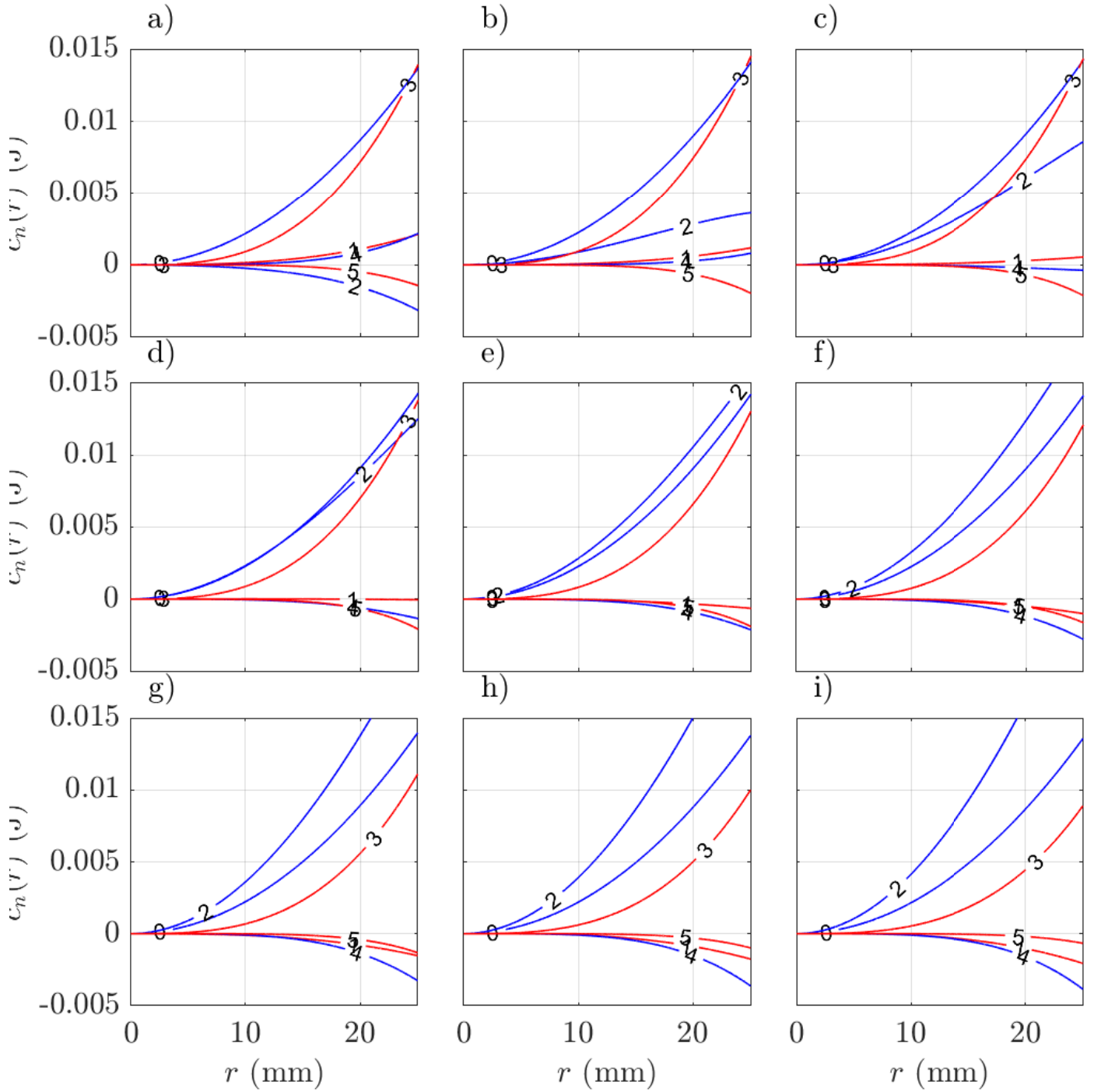


Figure 2.8: Coefficients of the multipole expansions of the magnetogravitational potentials displayed in figure 2.4, for  $n=0-5$ . Blue lines indicate even coefficients and red lines indicate odd coefficients. a)  $\kappa = -0.945$ , b)  $\kappa = -0.924$ , c)  $\kappa = -0.903$ , d)  $\kappa = -0.882$ , e)  $\kappa = -0.861$ , f)  $\kappa = -0.84$ , g)  $\kappa = -0.819$ , h)  $\kappa = -0.798$  and i)  $\kappa = -0.777$

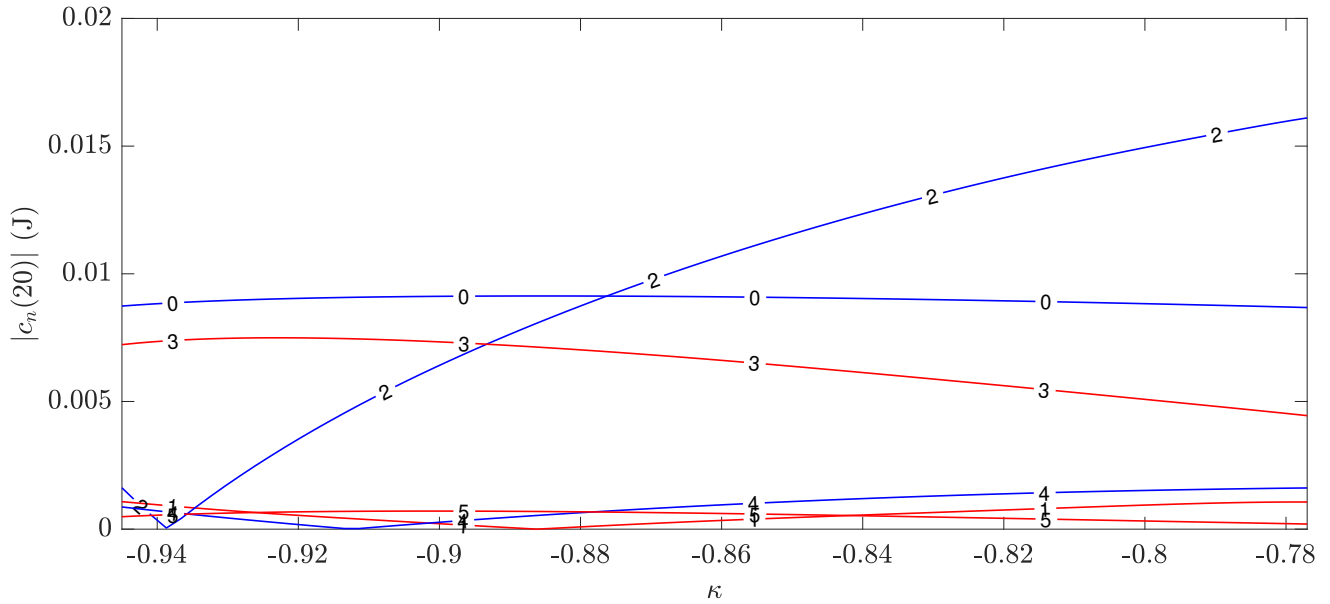


Figure 2.9: Absolute value of the multipole coefficients  $c_n(r)$  evaluated at  $r = 20$  mm as a function of  $\kappa$  for the cryogenic magnet. Even coefficients are indicated in blue and odd coefficients are indicated in red.

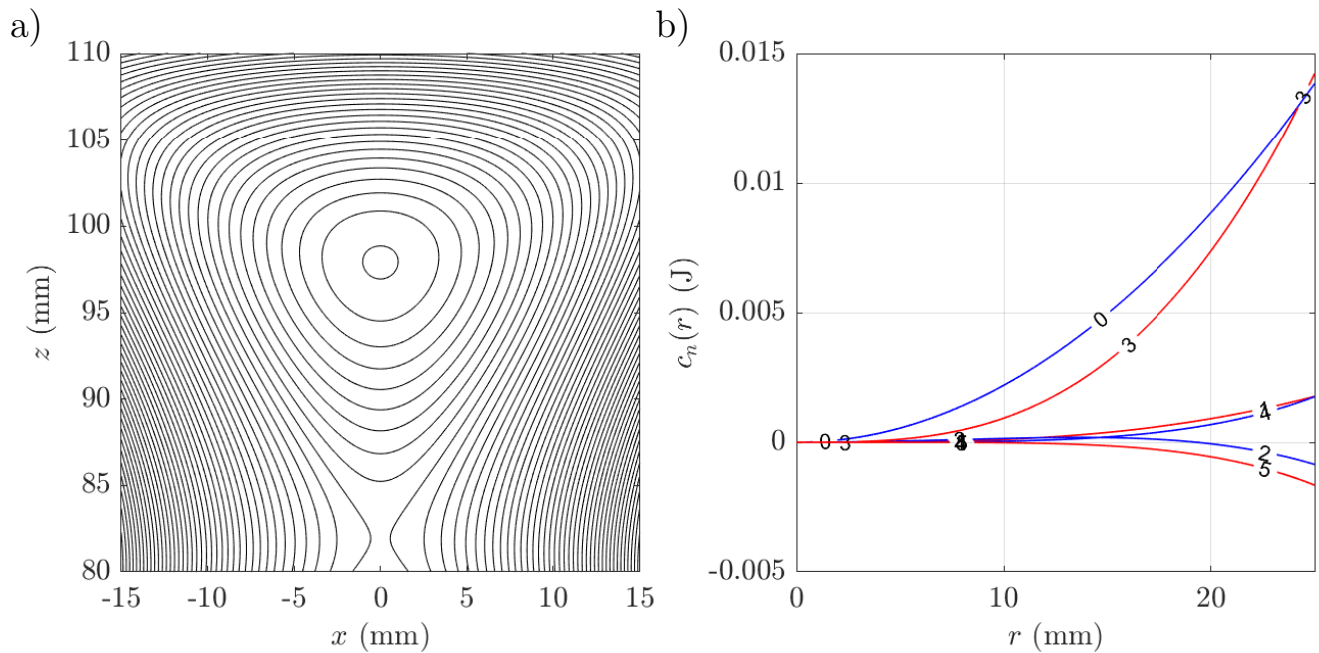


Figure 2.10: a) Contour plot and b) coefficients of the multipole expansion for the cryogenic magnet for  $\kappa = -0.9387$ . In b) blue lines indicate even coefficients and red lines indicate odd coefficients.

# Chapter 3

## Diamagnetic levitation of bubbles

Experimental studies on bubbles are encumbered by the basic problem that bubbles rise due to their buoyancy. Bubbles can be trapped at a solid- or liquid-gas interface but these methods inhibit the free movement of bubbles. It is possible to trap and manipulate bubbles using optical tweezers [32], but so far it has only been possible to trap a small number of bubbles with diameters on the order of micrometres using this technique. Trapping of bubbles has also been achieved using ultrasonic transducers [33], but due to the strong acoustic radiation force required to counteract the buoyancy force, the shape of bubbles trapped in this way deform into oblate spheroids. Also, due to the high-frequency acoustic waves required to trap bubbles using this method, Faraday instabilities are observed at the surface of acoustically trapped bubbles. Experiments in orbit or on parabolic flights allow the trapping and manipulation of mm–cm sized bubbles but are costly and severely time-limited. Here we present a new method for trapping and studying mm–cm diameter air bubbles in water using diamagnetic levitation.

One of our main motivations for finding a new technique to stably trap bubbles is to study the oscillations of bubbles. The stability of the oscillations of bubbles undergoing radial oscillation is important in understanding the phenomenon of sonoluminescence, placing an upper limit on the equilibrium size of bubbles that exhibit this effect [34]. Additionally, exploiting bubble oscillations has shown an increased efficiency in industrial processes requiring efficient mass transfer between bubbles of a gas phase and a surrounding liquid. An example of such a process is in bioreactors requiring aeration. Here, the mass transfer rate between the two phases is enhanced considerably by shape oscillations of the bubbles [35], [36].

### 3.1 Stable diamagnetic levitation of room temperature spherical bubbles

In chapter 2 we demonstrated that it is possible to stably levitate objects in a fluid as long as the surrounding fluid is more paramagnetic than the object. We showed

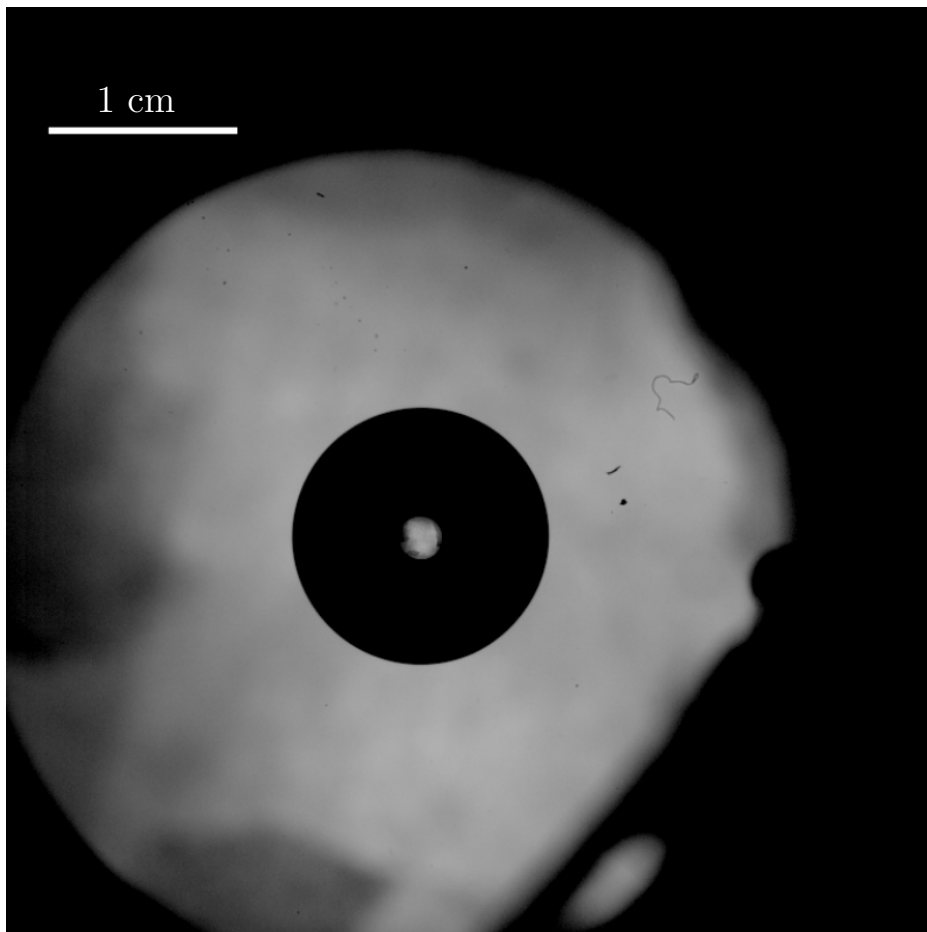


Figure 3.1: Image of a 13.7 mm diameter air bubble levitating in an  $0.11 \text{ mol L}^{-1}$  aqueous manganese chloride solution in the bore of the Cryogenic magnet. The field strength of the magnet at the centre of the solenoid was  $B_0 = 14 \text{ T}$ . The image was taken looking down the bore of the magnet

this is true in the case for objects that are both more dense and less dense than the surrounding fluid.

We are only aware of two previous experiments that use diamagnetic levitation to stably levitate bubbles [37], [38]. In both cases, bubbles of gaseous oxygen are levitated in liquid oxygen. Here, cryogenic temperatures are required to keep the oxygen in the liquid phase. As well as this, bubbles in these experiments also experience demagnetization forces that are comparable in size to surface tension forces, due to the presence of the strong magnetic field. This leads to the deformation of the shape of the bubbles into ellipsoids.

For the Cryogenic Ltd. superconducting magnet used in experiments throughout this thesis, it is possible to levitate objects as long as  $0.7665 < |\kappa| < 0.9584$  and  $\chi_2 > \chi_1$ , where  $\kappa$  is as defined in section 2.5. Most materials found in nature are diamagnetic, including water, therefore to make the surrounding fluid paramagnetic

a paramagnetic salt may be added, e.g. salts formed from manganese, gadolinium or chromium. By placing cylinders filled with aqueous solutions of  $0.1 - 0.2 \text{ mol L}^{-1}$  manganese chloride in the bore of the Cryogenic magnet, we found we were able to stably levitate air bubbles at a position  $\sim 10 \text{ cm}$  below the centre of the solenoid, at a central field strength of  $B_0 \approx 10 - 16 \text{ T}$ .

Figure 3.1 shows an image of an air bubble stably levitating in an aqueous manganese chloride solution in the bore of the Cryogenic magnet. In our experiments, demagnetisation effects were never observed as demagnetisation forces are many orders of magnitude weaker than any other forces experienced by the bubbles. Although bubbles experience a weak restoring force due to the magnetogravitational potential trap (equivalent to  $\sim 0.1 \text{ g}$ ) this force is several orders of magnitude weaker than surface tension forces felt by the levitated bubbles, hence all bubbles attained a spherical shape when levitated in this manner.

## 3.2 Experimental set-up

Here we present the experimental set-up used to conduct experiments on diamagnetically levitated air bubbles discussed throughout this thesis.

We used a 1 litre cylindrical tank of diameter 57 mm filled with an aqueous manganese chloride solution, which was fitted in the bore of the Cryogenic magnet as shown in figure 3.2. The top and bottom of the tank were constructed from clear plastic to allow experiments to be both illuminated and visualised. Bubbles were injected into the stable levitation point from an L-shaped tube connected to an air-filled syringe. By positioning the tip of the L-shaped tube at different positions within the bore we were able to generate bubbles of radii of approximately 1–8 mm. It was found that if the position of the tube was kept stationary and the flow rate of air through the syringe was small enough (less than some critical flow rate), we could consistently produce multiple bubbles of equal radius (within experimental error). This is due to the fact that at vanishingly small flow rates the volume at which a bubble detaches from a needle is given by the point at which surface tension forces holding the bubble to the needle and buoyancy forces on the bubble are equal [39]–[41]. Therefore, as effective buoyancy forces on a bubble vary as a function of position in the magnet, we were able to vary the size of bubbles relative to each other by moving the tip of the L-shaped tube towards and away from the stable levitation point.

Experiments were illuminated by a 0.4 W white LED which was placed under the tank. A 45-degree angled mirror was placed above the tank allowing experiments to be imaged. Two convex lenses, of focal length 40 cm, arranged in a refracting telescope layout were placed between the mirror and any camera being used. This optical set-up allowed for cameras to be placed away from the strong magnetic fields generated by the cryogenic magnet, as well as increasing the resolution of images we were able to record.

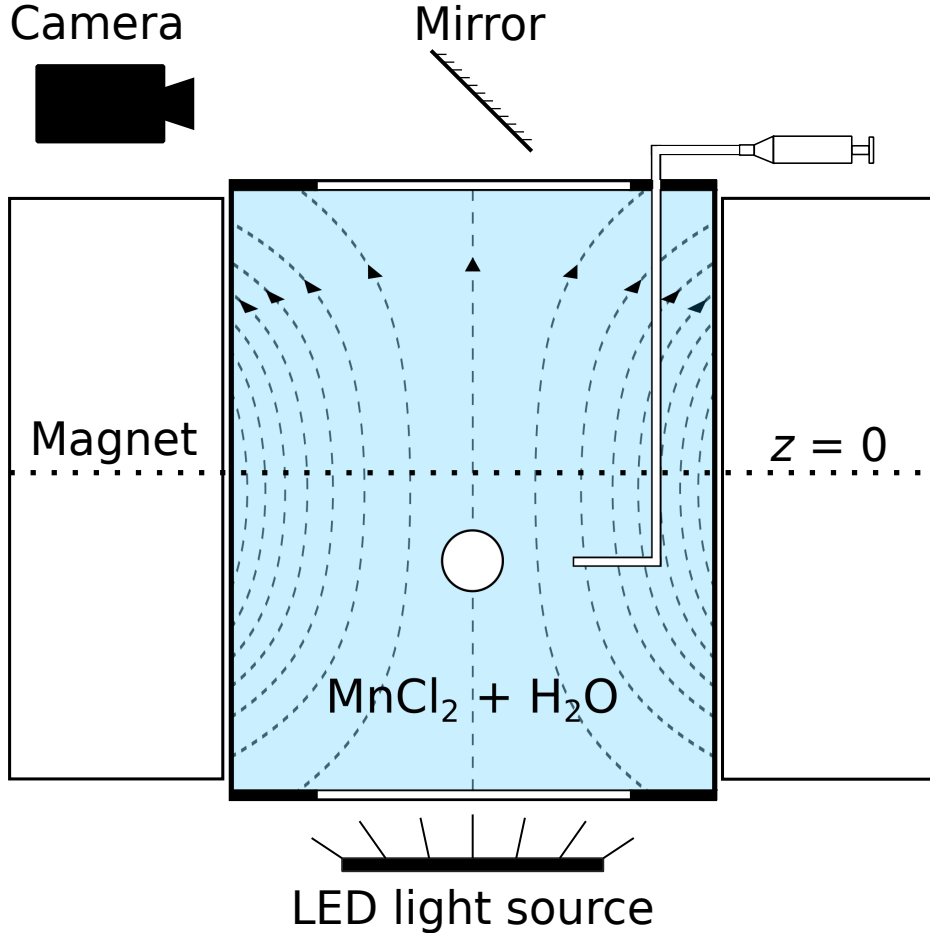


Figure 3.2: Schematic of experimental set-up used to diamagnetically levitate bubbles. Aspect ratio and dimensions of superconducting magnet are not to scale. Dashed lines are representative of the magnetic field lines inside the magnet bore.

### 3.3 Bubble coalescence experiments

In this section, we describe experiments used to study nonlinear surface oscillations of bubbles, the results of which we present in chapter 4.

To produce surface oscillations, we begin by levitating two air bubbles in hydrostatic equilibrium side-by-side. These bubbles then coalesce to produce a single levitating bubble, and we study the resulting shape oscillations. We consider two cases: a symmetric case, where the radii of the initial ‘parent’ bubbles are equal, within experimental uncertainty, and an asymmetric case, where the radii of the parent bubbles differ by a factor of 1.5.

We used the Cryogenic magnet to levitate air bubbles in a weakly paramagnetic aqueous solution of manganese chloride ( $0.18 \text{ mol L}^{-1}$ ,  $\chi_2 = 2.5 \times 10^{-5}$ ). The central field strength of the magnet was set to  $B_0 = 10.7 \text{ T}$  at the centre of the solenoid. The stable levitation point of the bubbles was approximately 97 mm below the centre of

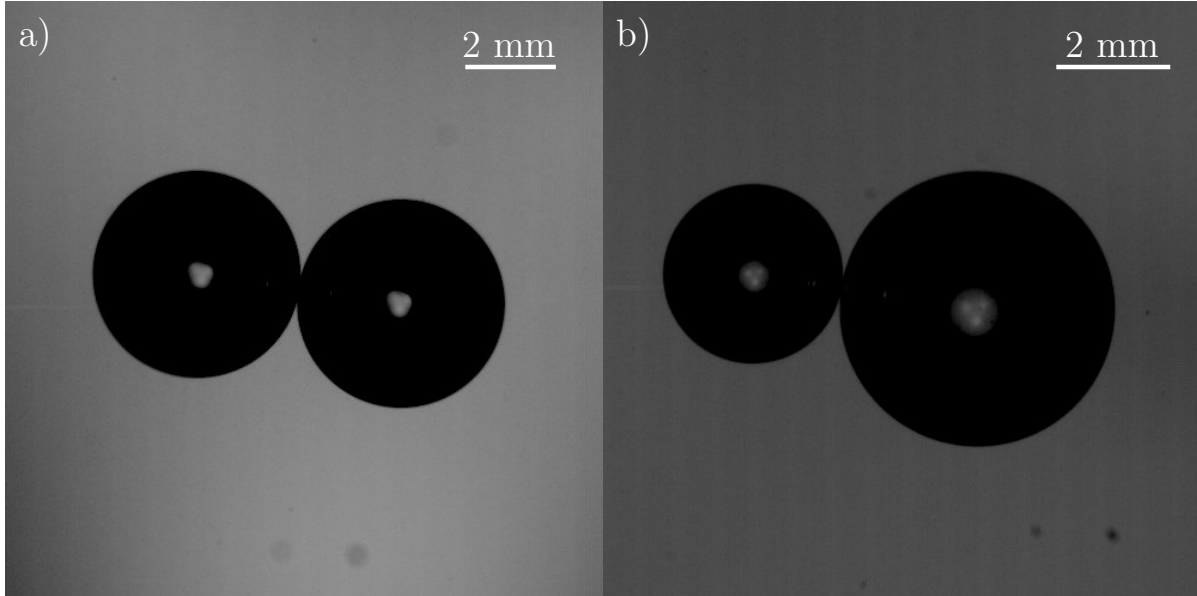


Figure 3.3: Images of the initial state of the parent bubbles, i.e. before coalescence, are shown for a) the symmetric case and b) the asymmetric case.

Case	Radius 1 (mm)	Radius 2 (mm)	Ratio of radii	$\rho_2$ (kg m <sup>-3</sup> )	$\gamma$ (mN m <sup>-1</sup> )	$\mu$ (Pa s <sup>-1</sup> )
symmetric	2.31±0.03	2.31±0.03	1.00±0.03	1017±1	68±1	*0.89 × 10 <sup>-3</sup>
asymmetric	1.60±0.02	2.46±0.02	1.54±0.03	1017±1	70±1	*0.89 × 10 <sup>-3</sup>

Table 3.1: Physical parameters of the fluids used in each series of experiments. \* denotes values taken from Huber *et al.* [43]; we have assumed that the viscosity of our fluid is equal to that of water at room temperature, as the low concentration of manganese chloride in the solution is assumed to have a negligible effect.

the solenoid.

Using an L-shaped tube we injected two parent bubbles into the stable levitation point. We observed that the parent bubbles remained at rest (i.e. in hydrostatic equilibrium) for 3–4 seconds before the onset of coalescence. Experiments were recorded using a high-speed camera (Phantom Miro M340). A frame rate of up to 5000 frames per second was used with a resolution varying from 20 – 30  $\mu\text{m}$  per pixel.

Figure 3.3a & 3.3b show the initial condition for each of the two cases we considered in this study. The radii of each of the initial bubbles, as well as the physical properties of the surrounding fluid are given in table 3.1. The surface tension was calculated from measurements of the oscillation frequency of the  $n = 2$  mode of the bubbles as the amplitude of oscillations tended to zero. Density was measured using a volumetric flask and is in agreement with the empirical formula of Novotny and Sohnel [42].

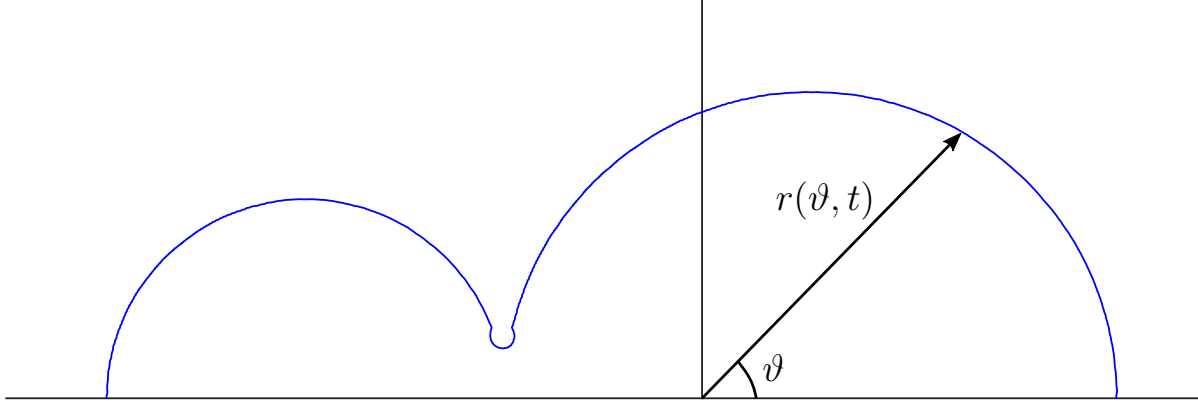


Figure 3.4: Diagram illustrating the coordinate system used in decomposition of the interface. The origin is taken to be at the centre of mass of the bubble system.

### 3.3.1 Image processing and analysis

The data taken in experiments was in the form of black-and-white high-speed videos. Radii of the parent bubbles before coalescence were calculated using a Hough transform on the initial frames of the videos before coalescence proceeded [44]. This gave an error of one pixel per diameter due to the highly spherical nature of the bubbles.

For each video frame we extracted the surface profile of the bubble using the Sobel edge detection method [45]. The extracted curve was then split in half down the symmetry axis and its coordinates, representing the pixel values of the surface, were converted into polar coordinates. The surface contour of the bubble,  $r(\vartheta, t)$ , was measured from the origin at the bubble's centre of mass, where  $\vartheta$  is the polar angle measured from the horizontal  $x$ -axis, i.e. along the axis joining the centres of the original two parent bubbles (figure 3.4). To remove random fluctuations due to the pixelation of the experimental images a 20th degree polynomial was fitted to  $r$  as a function of  $\cos \vartheta$ . This requires  $r(\vartheta, t)$  to be single valued for all  $\vartheta$ , which is true except for very early times after coalescence and for a brief period during pinch-off of a small satellite bubble early in the coalescence. We then decomposed  $r(\vartheta, t)$  as a series of spherical surface harmonics  $r(\vartheta, t) = \sum_{n=0} S_n(\vartheta, t)$ . Since the coalescence is axisymmetric about the horizontal  $x$  axis there are no contributions from tesseral or sectoral harmonics, the surface harmonics may be written purely in terms of the zonal harmonics  $S_n(\vartheta, t) = A_n(t)P_n(\vartheta)$ .

To estimate the error of the amplitude of the zonal harmonics we applied the method described above to the functions

$$f_2(\theta) = \frac{1}{N} (1 + 0.6 \cos(2\theta)), \quad (3.1)$$

and

$$f_3(\theta) = \frac{1}{N} (1 + 0.3 \cos(3\theta)), \quad (3.2)$$

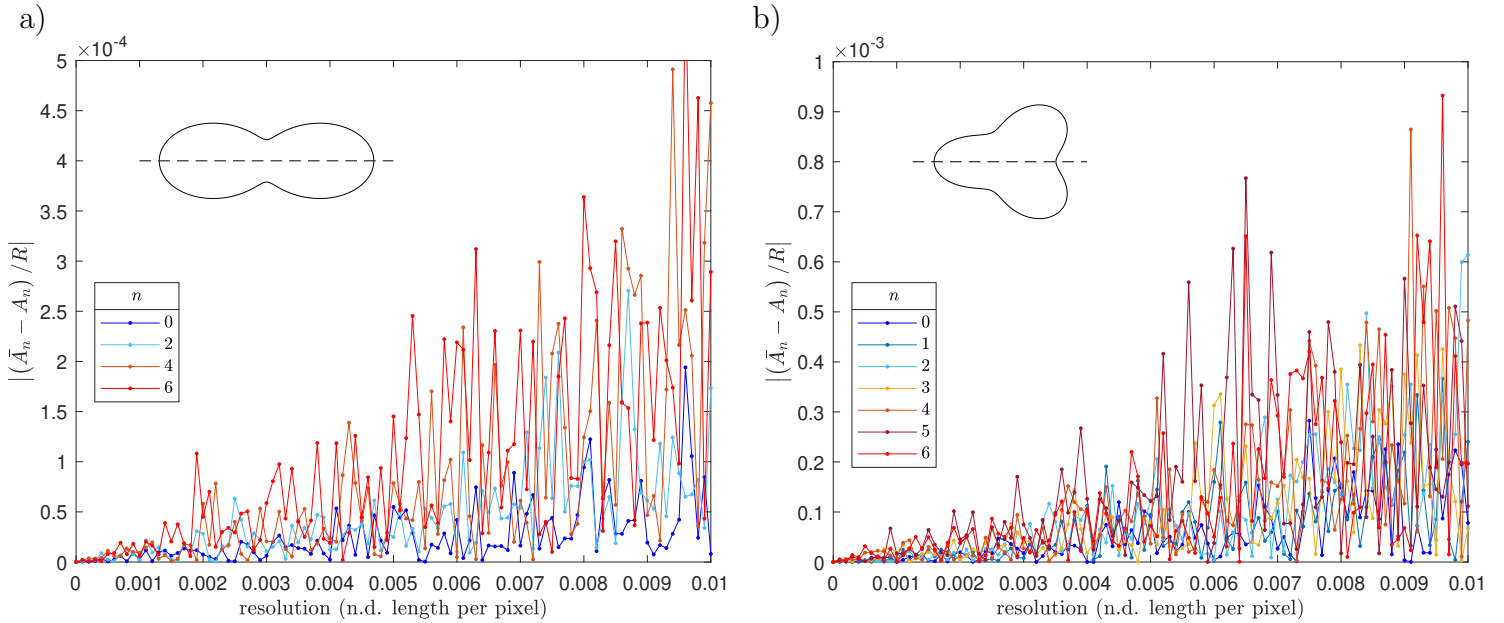


Figure 3.5: Plots of the deviation of non-dimensional amplitude as a function of non-dimensional length per pixel. Values for modes  $n = 0-6$  are shown. An image showing the surface being decomposed into Legendre polynomials is displayed in each figure. Here the dashed line is the symmetry axis through the centre of the shape.

where  $\bar{N}$  is a normalisation factor, such that that volume created by integrating the functions as solids of revolution is equal to  $V = 4/3\pi$ , hence  $\sqrt[3]{3V/4\pi} = 1$ . These functions were chosen as they are representative of the surface contours observed in experiment. To quantify the error, we compared the amplitudes to discretised versions of the same functions at different non-dimensional resolutions. The functions were discretised into 3000 points and to simulate the effect of different camera resolutions the horizontal and vertical coordinates of these points were then rounded each to the closest integer number of pixels for a given resolution; i.e. if a point had a vertical coordinate of 0.76 and we were analysing a resolution of 0.1 this point would be rounded to 0.8. We calculated the resolution as non-dimensional length per pixel as this allowed for direct comparison with experiment where this value is simply the resolution divided by the radius of the bubble at rest, hence why the functions were normalised to have a volume of  $4\pi/3$ .

Plots of the deviation of non-dimensional amplitude of modes  $n = 0 - 6$  as a function of non-dimensional length per pixel are shown in figure 3.5. Only even modes are displayed in figure 3.5a due to the symmetric nature of the function leading to odd modes having zero amplitude. It can be seen from both plots that as resolution decreases the error in the amplitudes decreases to zero, as is expected. Also, in both cases, for a given resolution, the higher the degree of the mode the greater the error on average. For the experiments analysed here, the non-dimensional resolution is 0.0091 in the symmetric case and 0.008 in the asymmetric case. Hence, figure 3.5

suggests that the error in non-dimensional amplitude calculated from experiment is at maximum  $5 \times 10^{-4}$  for modes  $n = 0-4$  and  $9 \times 10^{-4}$  for modes  $n = 5-6$ .

# Chapter 4

## Nonlinear surface oscillations of bubbles

In this chapter and in Hunter-Brown *et al.* [46], we report on the nonlinear surface oscillations of bubbles. We discuss experiments in which we use bubble coalescence to introduce large axisymmetric perturbations which lead to large amplitude surface oscillations. These experiments are then compared with numerical simulations and the theoretical model of Tsamopoulos and Brown [5]. For both experiment and simulation, we decompose the surface of the bubbles into spherical harmonics to analyse the frequency of different shape modes as a function of amplitude and to analyse the mode coupling between different spherical harmonics. Good agreement is found between experiment, numerical simulation, and the analytical model of Tsamopoulos and Brown [5] when the amplitude of a single surface mode is dominant, but when several surface modes are oscillating with moderate or large amplitudes, poor agreement between the model and what is observed in experiment and simulation is seen.

### 4.1 Theoretical models for the surface oscillations of bubbles

When the surface of a bubble of gas surrounded by a liquid is perturbed from its equilibrium shape the increase in surface energy of the system, owing to the surface tension, causes the bubble to oscillate. The first mathematical model for the shape oscillations of bubbles was presented by Lamb [47]. Lamb considered the case of a spherical volume of inviscid incompressible fluid immersed in a second similar fluid in the absence of gravity, and used linear stability analysis to find the frequencies of the normal modes of the shape oscillations. By decomposing the interface between the fluids into spherical harmonics, Lamb found that each spherical harmonic oscillated at an eigenfrequency dependent on the coefficient of surface tension,  $\gamma$ , the density of the inner and outer fluids,  $\rho_1$  and  $\rho_2$  respectively, the radius of the bubble at rest,  $R$ ,

and the degree of the spherical harmonic,  $n$ . If the density of the surrounding fluid is taken to be negligible in comparison to the density of the inner fluid, the earlier result derived by Rayleigh [48] for the oscillation frequencies of a liquid droplet is recovered, whereas if the density of the inner fluid is taken to be negligible in comparison to the density of the surrounding fluid, the oscillation frequencies of a gas bubble in liquid are found,

$$\omega_n^{(0)} = \frac{1}{\tau} \sqrt{(n^2 - 1)(n + 2)}, \quad (4.1)$$

where  $\tau = \sqrt{\frac{\rho_2 R^3}{\gamma}}$  is the capillary time and the superscript (0) denotes the leading order approximation to the oscillation frequency in the limit of vanishingly-small perturbations to the bubble surface.

By considering the velocity fields found for the linear oscillations of inviscid fluids, Lamb [47] was able to estimate the viscous damping for the amplitude of each shape mode in the limit of high Reynolds number. Lamb found that damping for each shape mode was proportional to  $e^{-\alpha_n t}$ , where the rate of viscous dissipation was

$$\alpha_n = \frac{\mu}{\rho_2 R^2} (2n + 1)(n + 2), \quad (4.2)$$

where  $\mu$  is the dynamic viscosity of the surrounding fluid.

Miller and Scriven [49] extended the work of Lamb by considering the case of two viscous incompressible fluids. Transcendental equations were derived for the full viscous solutions; the results of Lamb [47] are obtained in the limit of low viscosity. Prosperetti [50] considered the initial value problem of a slightly perturbed, spherical, incompressible viscous fluid immersed in a second incompressible viscous fluid. After an initial period the damping rate and oscillation frequency approaches the steady state solutions found by Miller and Scriven [49].

The first study to consider moderate amplitude oscillations was carried out by Tsamopoulos and Brown [5] (herein referred to as T&B) using the Poincaré-Lindstedt method [51] to calculate second order corrections for the velocity potential, shape functions, and eigenfrequencies of individual axisymmetric modes of inviscid, incompressible bubbles and droplets.

The dimensionless surface shape was found to be of the form

$$\begin{aligned} F(\theta, t; \varepsilon) &= \sum_{k=0}^{\infty} \frac{\varepsilon^k}{k!} F^{(k)}(\theta, t) = \sum_{k=0}^{\infty} \frac{\varepsilon^k}{k!} \frac{d^k}{d\varepsilon^k} F(\theta, t; 0) \\ &= 1 + \varepsilon P_n(\theta) \cos(\omega_n t) + \frac{\varepsilon^2}{2} \sum_{k=0}^n c_k P_{2k}(\theta) (\cos(2\omega_n t) + d_k) + O(\varepsilon^3), \quad (4.3) \end{aligned}$$

where here  $\theta$  is the polar angle,  $P_n$  is a Legendre polynomial of degree  $n$  and argument  $\cos(\theta)$ ,  $\varepsilon$  is the amplitude of a given mode as a fraction of the radius of the bubble at rest,  $c_k$  and  $d_k$  are coefficients determined by T&B;  $\omega_n$  is the frequency of oscillation

of mode  $n$  given by

$$\omega_n = \omega_n^{(0)} - \frac{\omega_n^{(2)}}{2}\varepsilon^2 + O(\varepsilon^4), \quad (4.4)$$

where  $\omega_n^{(2)}$  is the second order frequency coefficient determined by T&B. In contrast to the linear approximation of Lamb [47], where shape functions are given by a single spherical surface harmonic, the second order shape function terms add additional even-degree spherical harmonics, up to twice the order of the linear term. These second order terms oscillate at twice the frequency of the linear term. Revised values for the second order frequency coefficient  $\omega_n^{(2)}$  were published by Tsamopoulos [52], [53]. Further corrections up to third order have been calculated by M. M. Scase and may be found in the appendices of Hunter-Brown *et al.* [46].

A shift to lower frequency of the  $n = 2$  mode of liquid drops with increasing amplitude was observed by Wang *et al.* [54], who conducted experiments on droplets in microgravity, creating large initial perturbations using an acoustic trap, and by Becker *et al.* [55] who studied the large amplitude oscillations of free-falling ethanol droplets. Both observed the change in frequency as a function of amplitude to be in good agreement with the predictions of T&B. Trinh *et al.* [33] observed the moderate amplitude oscillations of acoustically-trapped silicone oil droplets in water. On experiments on droplets driven into  $n = 2$  shape oscillations, the authors mention that they observed the excitation of the  $n = 4$  surface harmonic at a frequency approximately twice that of  $\omega_2^{(0)}$ , consistent with T&B's prediction. In addition, they performed experiments on acoustically-trapped air bubbles in water: experiments studying free decay of oscillations found evidence for coupling between modes, but the data does not show quantitative agreement with the result obtained by T&B. One reason for this may be the influence of the method of levitation in these experiments, which distorts the equilibrium shape of drops and bubbles into oblate spheroids. Kornek *et al.* [56] studied the large amplitude oscillations of thin-film soap bubbles and found a quadratic relationship between frequency and amplitude for surface oscillations, and coupling between the 2nd and 4th degree shape modes. They measured the shift in frequency of the oscillations of each surface harmonic as a function of their amplitude and compared with the second order frequency coefficients,  $\omega_n^{(2)}$ , calculated by T&B. In the case where large amplitude mode 2 oscillations were excited,  $\omega_2^{(2)}$  was found to be approximately 10% greater than value predicted by T&B, but in the case that both large amplitude mode 2 and 3 oscillations were excited,  $\omega_2^{(2)}$  was found to be up to 60% greater and  $\omega_3^{(2)}$  was found to be more than three times the value of T&B.

## 4.2 Influence of the magnetogravitational trap on surface oscillations

The restoring forces that stabilise the levitation of a droplet or bubble acts as an additional cohesive force, giving rise to a relatively small increase in the frequencies

of their shape oscillations [13], [57]. Hill and Eaves [13] calculated the shift to higher frequency of the linear modes of a diamagnetically levitated spherical water droplet in air. Here, we calculate the frequency shift in the linear modes for the more general case of a levitated spherical fluid droplet (bubble) of density  $\rho_1$  immersed in a fluid of density  $\rho_2$ . Using this analysis, we show that in our experiments the restoring forces that stabilise the levitation of the bubbles are relatively weak compared to surface tension, therefore we expect the effect of the trap to have a negligible effect on oscillation frequencies.

Neglecting viscosity, the governing equations in each fluid layer are given by the incompressible Euler equations

$$\rho_j \frac{D\mathbf{u}_j}{Dt} = -\nabla p_j + \mathbf{f}_j, \quad (4.5a)$$

$$\nabla \cdot \mathbf{u}_j = 0, \quad (4.5b)$$

for  $j = 1, 2$  corresponding to the inner and outer fluid layers respectively, where  $\mathbf{f}_j$  is the body force felt by the fluids. We shall only consider conservative body forces, hence the body force may be expressed as the gradient of some potential,  $\mathbf{f}_j = -\nabla\psi_j$ . Here we use the symbol  $\psi$  to denote potential energy rather than  $u$  to avoid confusion between the potential energy and the fluid velocity. Therefore, we may rewrite equation (4.5a) as

$$\rho_j \frac{D\mathbf{u}_j}{Dt} = -\nabla [p_j + \psi_j]. \quad (4.6)$$

By assuming our velocity fields may be expressed as the gradient of velocity potentials  $\mathbf{u}_j = \nabla\varphi_j$ , we find from equation (4.5b) that these velocity potentials must satisfy Laplace's equation. Working in spherical coordinates  $(r, \theta, \phi)$ , the solution to Laplace's equation is given by

$$\varphi_j = [a_j(t)r^n + b_j(t)r^{-(n+1)}] Y_n^m(\theta, \phi), \quad (4.7)$$

where  $Y_n^m(\theta, \phi)$  is a spherical harmonic of degree  $n$  and order  $m$ . It is a requirement that the velocity in each fluid layer is finite, hence  $b_1(t) = 0$  and  $a_2(t) = 0$ .

To look for linear perturbation solutions of the equations of motion (4.6), asymptotic expansions of the velocity field, pressure field and potential are made by expanding in the small parameter  $\varepsilon$ , such that

$$\mathbf{u}_j = \mathbf{u}_j^* + \varepsilon \mathbf{U}_j + O(\varepsilon^2), \quad (4.8a)$$

$$p_j = p_j^* + \varepsilon P_j + O(\varepsilon^2), \quad (4.8b)$$

$$\psi_j = \psi_j^* + \varepsilon \Psi_j + O(\varepsilon^2), \quad (4.8c)$$

where  $\varepsilon$  is defined to be the initial amplitude of perturbations made to the interface of the droplet and satisfies the condition  $\varepsilon \ll R$ , where  $R$  is the radius of the droplet at rest. It is noted that the fluid is perturbed from an initially hydrostatic state,

therefore  $\mathbf{u}_j^* = \mathbf{0}$ . Noting this and inserting the conditions (4.8) into equation (4.5a) and ignoring all terms of order  $\varepsilon$  and higher allows for a relationship between the leading order potential and leading order pressure field to be obtained

$$p_j^* = -\psi_j^* + C_j, \quad (4.9)$$

where  $C_j$  is a constant of integration. Carrying out the same procedure but only retaining leading and first order terms we obtain the first order equation of motion

$$\rho_j \frac{\partial \mathbf{U}_j}{\partial t} = -\nabla [P_j + \Psi_j]. \quad (4.10)$$

This equation may be integrated to obtain

$$\rho_j \frac{\partial \varphi_j}{\partial t} + P_j + \Psi_j = h(t), \quad (4.11)$$

where  $h(t)$  is some constant of integration we set equal to zero without loss of generality.

We make the ansatz that the interface between the two fluids is

$$\mathcal{S} := r - \{R + \varepsilon Y_n^m(\theta, \phi) e^{i\omega t} + O(\varepsilon^2)\} = 0, \quad (4.12)$$

where it is assumed that the interface is constructed from spherical harmonics, each of which is undergoing periodic oscillations at an angular frequency  $\omega$  dependent on the order and degree of the spherical harmonic. For clarity, we define the spherical harmonics used here to be

$$Y_n^m(\theta, \phi) = P_n^m(\cos(\theta)) e^{im\phi}, \quad (4.13)$$

where  $P_n^m(\cos(\theta))$  are the associated Legendre polynomials

$$P_n^m(x) = (-1)^m (1-x^2)^{m/2} \frac{d^m}{dx^m} P_n(x), \quad (4.14)$$

and  $P_n(x)$  are Legendre polynomials of order  $n$  and argument  $x$ , where for  $m < 0$

$$P_n^{-m}(x) = (-1)^m \frac{(l-m)!}{(l+m)!} P_n^m(x). \quad (4.15)$$

We shall now apply the kinematic condition on the interface

$$\left. \frac{D\mathcal{S}}{Dt} \right|_{\mathcal{S}} = 0, \quad (4.16)$$

which enforces that the fluid at the interface moves with the interface. This leads to

$$\left( \frac{\partial \varphi_j}{\partial r} - i\omega Y_n^m(\theta, \phi) e^{i\omega t} \right) \Big|_{\mathcal{S}} = 0, \quad (4.17)$$

which when solved for in each fluid layer results in an expression for the coefficients

$$a_1(t) = \frac{i\omega}{nR^{n-1}}e^{i\omega t}, \quad (4.18a)$$

$$b_2(t) = -\frac{i\omega}{(n+1)R^{-(n+2)}}e^{i\omega t}. \quad (4.18b)$$

Substituting these coefficients into equation (4.7), gives an expression for the velocity potential in each fluid layer, which then can be substituted into equation (4.11) giving expressions for the first order pressure field in each fluid layer

$$P_1 = \frac{\rho_1\omega^2 R}{n} \left(\frac{r}{R}\right)^n Y_n^m(\theta, \phi)e^{i\omega t} - \Psi_1, \quad (4.19a)$$

$$P_2 = -\frac{\rho_2\omega^2 R}{(n+1)} \left(\frac{r}{R}\right)^{-(n+1)} Y_n^m(\theta, \phi)e^{i\omega t} - \Psi_2. \quad (4.19b)$$

We shall now enforce continuity of stress at the interface, which is given by the expression

$$[-p_j]_{\pm}^{\pm} = \gamma\tilde{\kappa}. \quad (4.20)$$

Here,  $\gamma$  is the coefficient of surface tension,  $\tilde{\kappa}$  is the curvature of the interface and  $[\cdot]_{\pm}^{\pm}$  denotes the jump in a quantity from the outer fluid to the inner fluid across the interface  $\mathcal{S}$ . The curvature of the interface is given by

$$\tilde{\kappa} = \nabla \cdot \hat{\mathbf{n}}, \quad (4.21)$$

where  $\hat{\mathbf{n}}$ , the normal to the interface, is

$$\hat{\mathbf{n}} = \frac{\nabla \mathcal{S}}{|\nabla \mathcal{S}|}. \quad (4.22)$$

Therefore, by evaluating equation (4.21) and neglecting second-order terms and higher the curvature of the interface is found to be

$$\tilde{\kappa} = \frac{2}{R} + \varepsilon \frac{(n-1)(n+2)}{R^2} Y_n^m(\theta, \phi)e^{i\omega t} + O(\varepsilon^2). \quad (4.23)$$

Evaluating equation (4.20) and retaining only leading order terms gives the expression

$$C_1 - C_2 - (\psi_1^* - \psi_2^*)|_{\mathcal{S}} = \frac{2\gamma}{R}. \quad (4.24)$$

Similarly, evaluating (4.20) and only retaining leading order and first order terms gives the expression

$$\left( \frac{\rho_1\omega^2 R}{n} + \frac{\rho_2\omega^2 R}{(n+1)} - \frac{\gamma(n-1)(n+2)}{R^2} \right) Y_n^m(\theta, \phi)e^{i\omega t} = (\Psi_1 - \Psi_2)|_{\mathcal{S}}. \quad (4.25)$$

We will now consider the effect of the magnetic field on the fluids. The volume magnetic susceptibility in each fluid layer is given by  $\chi_j$ , where in both layers we

suppose that  $|\chi_j| \ll 1$ , as in our experiments the volume magnetic susceptibility in each layer is of order  $10^{-5}$  or less. We take  $\hat{\mathbf{z}}$  to be a unit vector in the vertical direction and  $z$  to be the spatial coordinate in the vertical direction, such that gravity,  $g$ , acts in the negative  $z$ -direction. The magnetic force per unit volume  $\mathbf{f}_{m_j}$  in each fluid layer subjected to a magnetic field of strength  $B = |\mathbf{B}|$ , which to a good approximation is given by [4]

$$\mathbf{f}_{m_j} = \frac{\chi_j}{2\mu_0} \nabla B^2. \quad (4.26)$$

Therefore accounting for gravity, the body force per unit volume acting on each fluid layer is

$$\mathbf{f}_j = \frac{\chi_j}{2\mu_0} \nabla B^2 - \rho_j g \hat{\mathbf{z}}, \quad (4.27)$$

It then follows that the magnetogravitational potential energy density  $\psi_j$  is

$$\psi_j = \rho_j g z - \frac{\chi_j B^2}{2\mu_0}. \quad (4.28)$$

We expand  $\psi_1 - \psi_2$  about around the stable levitation point using the multipole expansion, as show in chapter 2.5, hence

$$\psi_1 - \psi_2 = \sum_i c_i(r) Y_i^0(\theta, \phi), \quad (4.29)$$

where, here, the polar angle  $\theta$  is measured from the solenoid ( $z$ ) axis; we have disregarded all terms  $m \neq 0$  due to the rotational symmetry of the magnetic field about the  $z$ -axis. From now on we shall drop the summation sign for clarity. Taylor expanding (4.29) about  $R$  we find

$$\psi_1 - \psi_2 = \left[ c_i(R) + c'_i(R)(r - R) + \frac{c''_i(R)}{2}(r - R)^2 + \dots \right] Y_i^0(\theta, \phi), \quad (4.30)$$

where the prime denotes differentiation with respect to  $r$ . Finally, evaluating this expression at the interface  $\mathcal{S}$ , we obtain the expression

$$(\psi_1 - \psi_2)|_{\mathcal{S}} = [c_i(R) + \varepsilon c'_i(R) Y_n^m(\theta, \phi) e^{i\omega t}] Y_i^0(\theta, \phi) + O(\varepsilon^2). \quad (4.31)$$

We show below that, provided the droplet/bubble is only a few mm in diameter, the magnetogravitational trap in our experiments is well-approximated by a spherically symmetric parabolic potential well. Under the assumption that the magnetogravitational trap is spherically symmetric, i.e. that  $c_i(R) = 0$  for  $i \neq 0$ , then

$$(\psi_1 - \psi_2)|_{\mathcal{S}} = c_0(R) + \varepsilon c'_0(R) Y_n^m(\theta, \phi) e^{i\omega t} + O(\varepsilon^2), \quad (4.32)$$

where it should be noted  $Y_0^0(\theta, \phi) = 1$ . Substituting this into equation (4.24) and (4.25) allows us to obtain the dispersion relation

$$\omega^2 = \omega_\gamma^2 + \Delta\omega^2, \quad (4.33a)$$

where

$$\omega_\gamma^2 = \frac{\gamma}{R^3} \frac{(n-1)n(n+1)(n+2)}{\rho_1(n+1) + \rho_2 n}, \quad (4.33b)$$

$$\Delta\omega^2 = \frac{n(n+1)c'_0(R)}{R(\rho_1(n+1) + \rho_2 n)}. \quad (4.33c)$$

From this analysis it can be seen that the effect of the magnetogravitational trap is to always increase the oscillation frequency of any given mode. Although  $\Delta\omega^2$  increases with  $n$ , the fractional change  $\Delta\omega^2/\omega_\gamma^2$  decreases with increasing  $n$ .

In the absence of the magnetogravitational potential, the dispersion relation for an inviscid spherical droplet suspended in a second inviscid fluid derived by Lamb [47] is recovered:  $\omega = \omega_\gamma$ . In the limit that the density of the inner fluid is much greater than the density of the outer fluid,  $\rho_1 \gg \rho_2$ , the dispersion relation derived by Hill and Eaves [13] for a spherical droplet oscillating in a spherical magnetogravitational potential is recovered. Finally, in the limit that the density of the outer fluid is much greater than the density of the inner fluid,  $\rho_2 \gg \rho_1$ , the dispersion relation for a spherical bubble oscillating with small amplitude in a spherically-symmetric magnetogravitational potential is found

$$\omega^2 = \frac{\gamma(n-1)(n+1)(n+2)}{\rho_2 R^3} + \frac{(n+1)c'_0(R)}{\rho_2 R}. \quad (4.34)$$

We now obtain an estimate of the expected effect of the trap on  $\omega$  in our experiments. Figure 4.1 displays a plot of the coefficients  $c'_i(r)$  ( $i = 0, \dots, 5$ ), for the magnetogravitational potential in our experiments, where  $\kappa = 0.937$  (see section 2.5). The radii of the final bubbles, formed from the coalescence of the two parent bubbles, lie in the range 2.5 mm to 3.0 mm in these experiments. Table 4.1 displays values for the coefficients  $c'_i(r)$  for  $i = 0-5$ , for radii  $r = 2.91$  mm and  $r = 2.67$  mm, which correspond to the two cases studied in our experiments, the symmetric and asymmetric cases, respectively. The expansion shows that the shape of the trap is dominated by a parabolic spherically symmetric component, represented by  $c'_0(r) = kr$ . The next largest component after  $c'_0(r)$  is  $c'_3(r)$ , which represents an octupole component. Whereas the octupole component is an inherent feature of the trap, the quadrupole (oblate/prolate) component, represented by  $c'_2(r)$ , can be tuned by adjusting the strength of the magnetic field. In these experiments, we adjusted the magnetic field strength to minimise  $c'_2(r)$ . If we now neglect the dipole and octupole components of the trap in order to obtain an estimate for the shift in  $\omega$ , according to (4.34), we obtain the plot shown in figure 4.2 for bubbles of radius  $R = 2.67$  mm and  $R = 2.91$  mm. From this plot it is clear that the influence of such a trap leads to a no more than  $\sim 0.2\%$  increase in the oscillation frequency of the linear modes of bubbles of this size. Given such a small change in the linear mode frequencies, we expect that the effect on the frequencies of oscillations of moderate amplitude will also be similarly small.

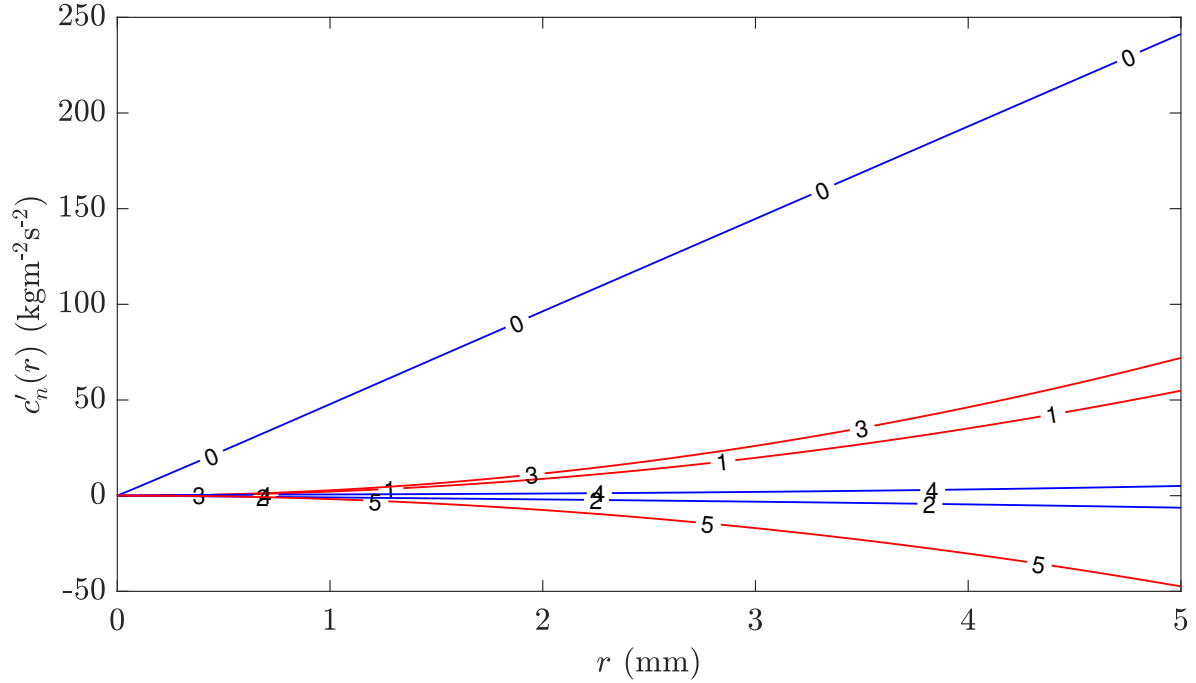


Figure 4.1: First derivatives of the multipole expansion coefficients calculated from the magnetogravitational potential. The physical constants used to calculate the magnetogravitational potential are  $\chi_1 = 5.1 \times 10^{-7}$ ,  $\chi_2 = 2.50 \times 10^{-5}$ ,  $\rho_1 = 1.6 \text{ kg m}^{-3}$  and  $\rho_2 = 1017 \text{ kg m}^{-3}$ . Here,  $\kappa = 0.937$  (see section 2.5).

$R$ (mm)	$c'_0(r)$	$c'_1(r)$	$c'_2(r)$	$c'_3(r)$	$c'_4(r)$	$c'_5(r)$
2.67	129.3	15.5	-2.7	20.4	1.4	-13.5
2.91	140.9	18.5	-3.0	24.2	1.7	-16.1

Table 4.1: Values of the coefficients  $c'_i(r)$  shown in figure 4.1 evaluated at two different radii, corresponding to the radii of the final bubbles, at rest, formed from the coalescence of the two parent bubbles in the experiments: asymmetric case, first row; symmetric case, second row.

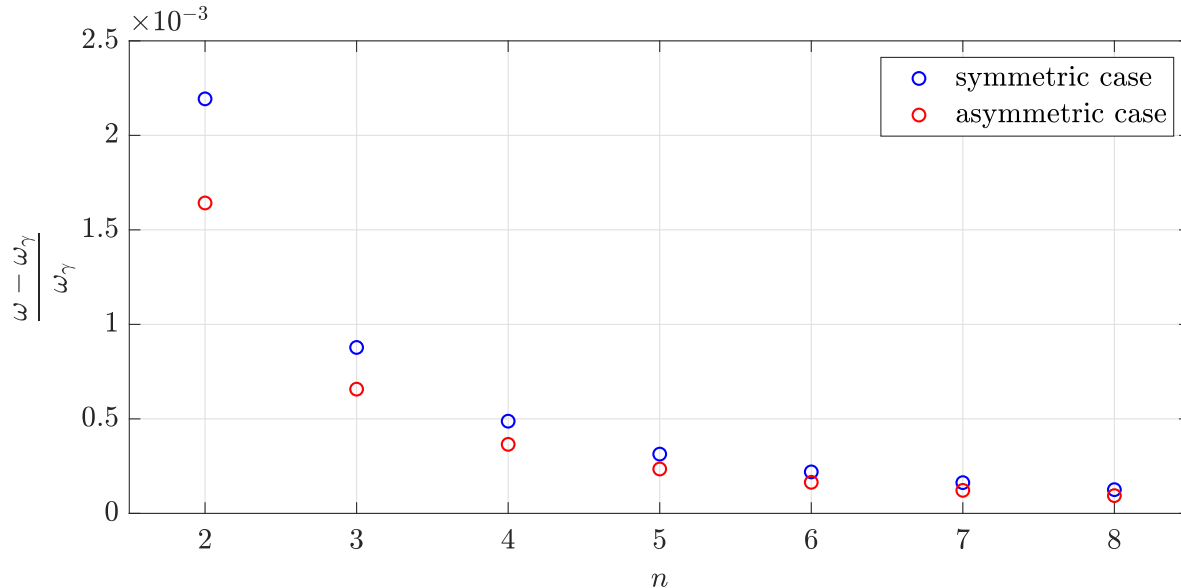


Figure 4.2: Shift in frequency due to the magnetogravitational trap, for modes  $n = 2$ – $8$  for both symmetric and asymmetric cases.

## 4.3 Computational fluid dynamic simulations

This section explains the numerical framework we used to model the coalescence of bubbles using the open-source software Basilisk [58]. An introduction to the code base and a large number of test cases are helpfully provided on the Basilisk website [58]. Of particular interest to anyone trying to recreate the numerical simulations presented in this chapter are the test cases *rising* and *oscillation*, the latter of which is discussed in further detail in Popinet [59].

### 4.3.1 Governing equations of motion

For incompressible flows, the equations of motion are given by the Navier-Stokes equations

$$\rho \left( \frac{\partial \mathbf{u}}{\partial t} + (\mathbf{u} \cdot \nabla) \mathbf{u} \right) = -\nabla p + \nabla \cdot (2\mu \mathbf{D}) + \mathbf{f}_\gamma, \quad (4.35a)$$

$$\nabla \cdot \mathbf{u} = 0. \quad (4.35b)$$

Equation (4.35a) denotes the momentum balance in the fluids, where the left hand side of the equation represents momentum advection and the right hand side is dependent on pressure  $p$ , the strain-rate tensor  $\mathbf{D}$ , which is equivalent to the symmetric part of the velocity gradient tensor ( $\mathbf{D} = (\nabla \mathbf{u} + \nabla \mathbf{u}^T)/2$ ) and surface tension forces  $\mathbf{f}_\gamma$ , represented here by a body force only present at the interface of the fluids.

Here, we have ignored forces due to the effect of gravity and strong magnetic fields. In experiment, diamagnetic levitation is used to create a weightless environment in which we levitate the bubbles and we assume the magnetic trap to have a negligible effect on the oscillation frequency of bubbles, which is justified by the analysis carried out in section 4.2.

We performed direct numerical simulation of the incompressible Navier-Stokes equations using the open source software Basilisk [58]–[60], which implements the one-fluid approximation utilising the volume of fluid (VOF) method for interface tracking [61]. To allow for the efficient computation of multiphase flows, the VOF method uses a “colour” function  $\mathcal{C}$ , which may only take values in the range  $0 - 1$ . Here, values of  $\mathcal{C} = 0$  denote positions where only manganese chloride solution is present and values of  $\mathcal{C} = 1$  denote positions where only air is present. Therefore  $\mathcal{C}$  colours the regions occupied by each fluid, where discontinuities in  $\mathcal{C}$  mark the interface between the two fluids. We may express the physical properties (density and viscosity) of the fluids as a function of  $\mathcal{C}$

$$\rho = \mathcal{C}\rho_1 + (1 - \mathcal{C})\rho_2, \quad (4.36a)$$

$$\mu = \mathcal{C}\mu_1 + (1 - \mathcal{C})\mu_2, \quad (4.36b)$$

where subscripts 1 and 2 denote the inner and outer fluids (air and manganese chloride solution), respectively. As the motion of the fluids develops in time it can be shown that the motion of the colour function must satisfy the following advection equation [62]

$$\frac{\partial \mathcal{C}}{\partial t} + \mathbf{u} \cdot \nabla \mathcal{C} = 0. \quad (4.37)$$

Surface tension forces are introduced into our system through the term

$$\mathbf{f}_\gamma = \gamma \tilde{\kappa} \delta_s \hat{\mathbf{n}}, \quad (4.38)$$

where  $\tilde{\kappa}$  is the local curvature of the fluid-fluid interface which is calculated using the height-function method [59],  $\hat{\mathbf{n}}$  is the normal vector to the interface and  $\delta_s$  is the Dirac-delta function, which is only non-zero on the interface. In the VOF method it can be shown that the r.h.s. of equation (4.38) is well approximated by [63]

$$\mathbf{f}_\gamma \approx \gamma \tilde{\kappa} \nabla \mathcal{C}. \quad (4.39)$$

### 4.3.2 Numerical domain

An axisymmetric domain was used to reduce computational cost. The simulated domain is the meridional plane, taken to be a square with side lengths 12 times that of the radius of the smallest bubble before coalescence. This relatively large domain volume was used to minimise wall effects on the simulation. A quad/octree dynamic adaptive mesh refinement scheme [59] was used to increase mesh resolution at the liquid-gas interface and in areas of relatively large velocity, down to a minimum

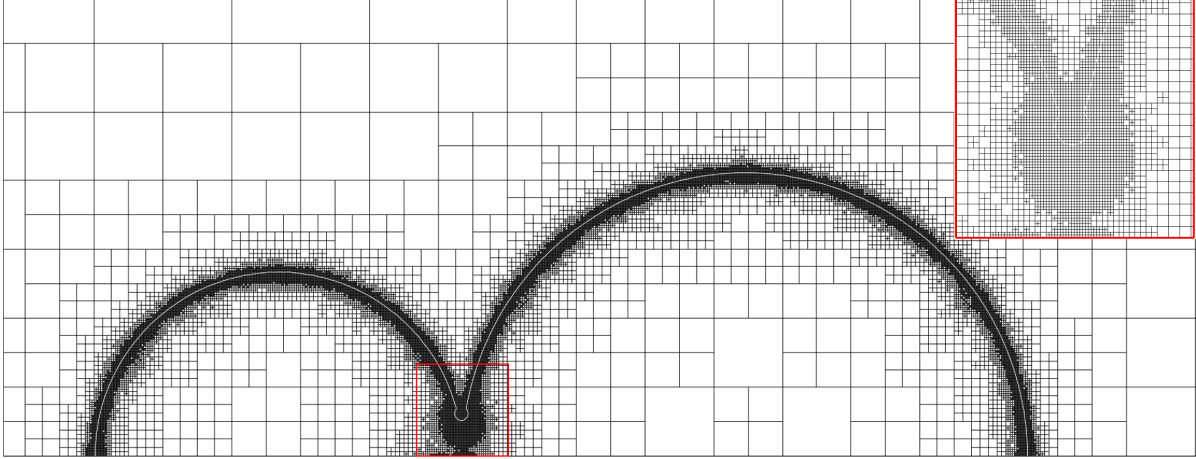


Figure 4.3: A section of the mesh used in the simulation of the asymmetric case. The inset shows an enlarged view of the highlighted section. The white line marks the interface of the bubble. This plot was obtained from the output of the simulation at time  $t = 0.01\tau$ .

cell side length of  $0.0059R_s$ , where  $R_s$  is the radius of the smallest of the two parent bubbles before coalescence. Grid adaption is based on minimizing the error estimated using a wavelet algorithm [60]. Such high resolution was required to accurately model the capillary-driven flows, particularly in the region of the neck between the original two parent bubbles. An example of one of the meshes used is shown in figure 4.3.

### 4.3.3 Numerical initiation of coalescence event

In the work reported here, numerical simulations have been used to simulate the coalescence of air bubbles in an aqueous manganese chloride solution. It was necessary to decide how to initiate the coalescence event in simulations. In experiment, it is assumed that once a pair of bubbles make contact there exists a thin film of liquid between the bubbles. It was observed that coalescence events occurred in experiments approximately 3–4 seconds after bubbles had come into contact with each other. Therefore, it was assumed that coalescence occurs after the thin film between the bubbles managed to drain away and eventually rupture allowing air in each bubble to freely flow between each other. To replicate this in simulation, a small neck of height  $R_s/8$  was initialised to connect the bubbles. Various neck heights were tested for the case of initially equal-sized bubbles. We found for neck heights less than  $R_s/6$  that there was no variation in the simulations for the minimum mesh resolution used in our investigation. A neck of height  $R_s/8$  was chosen as it reduced the additional volume of air added to the simulation to create the neck to be less than 0.005% of the total volume of air.

### 4.3.4 Evaluation of surface profiles

Here we explain the methodology used to extract the surface profiles of bubbles from simulations, and the post-processing performed to compare the results of T&B.

The surface profile of a bubble at a given time step was determined by extracting contours along  $\mathcal{C} = 0.5$ . Once the surface profile was determined surface harmonics were obtained from simulations in a similar manner as in experiment (see chapter 3.3.1), by decomposing the surface contour,  $r(\vartheta, t)$ , into a series of Legendre polynomials  $r(\vartheta, t) = \sum_{n=0} A_n(t)P_n(\vartheta)$ , at intervals of  $t = 0.01\tau$ .

## 4.4 Results

Except where stated otherwise, lengths and times are given in units of the radius of the final bubble at rest,  $R$ , and the capillary time,  $\tau = \sqrt{\frac{\rho_2 R^3}{\gamma}}$ , respectively; angular frequencies are given in units  $1/\tau$ .

A series of images showing the oscillations of a bubble formed from the coalescence of two equal-sized parent bubbles (symmetric case) is shown in figure 4.4 and a second series of images showing the oscillations of a bubble formed from the coalescence of two unequal-sized parent bubbles with radii in the ratio approximately 2:3 (asymmetric case) is shown in figure 4.5. In both cases, the parent bubbles were observed to remain at rest for a short time after their injection into the liquid, as the fluid drained from the small gap between them, before they coalesced. Once started, coalescence proceeded with the rapid growth of a neck generating axisymmetric capillary waves that travelled around each bubble away from the neck towards the apexes of the parent bubbles, as has been observed previously [64], [65]. The capillary waves formed protrusions at the apexes which then pinched off to form small satellite bubbles in both cases. After these ejection events, the bubble formed from the coalescence continued to oscillate. The amplitude of these oscillations decayed with time due to viscous dissipation. From the images, one can discern a contribution from several surface harmonics, in both symmetric and asymmetric cases. The modes of higher degree damp more quickly, with only mode 2 clearly visible in the final images of figure 4.4 (symmetric case) and modes 2 and 3 visible in the final images of figure 4.5 (asymmetric case).

### 4.4.1 Satellite bubble ejection

Protrusions form at the apexes of the parent bubbles during coalescence due to capillary waves propagating around the surface of the bubbles. Successive waves reach the apexes of the parent bubbles leading to these protrusions pinching off to form satellite bubbles [64], [66]. In both the symmetric and asymmetric case, we observe the ejection of satellite bubbles during the initial coalescence.

In the symmetric case, we observe the simultaneous ejection of two satellite bubbles at time  $t = 0.57\tau$ , see figure 4.6a,b. The ejected satellite bubbles are found to

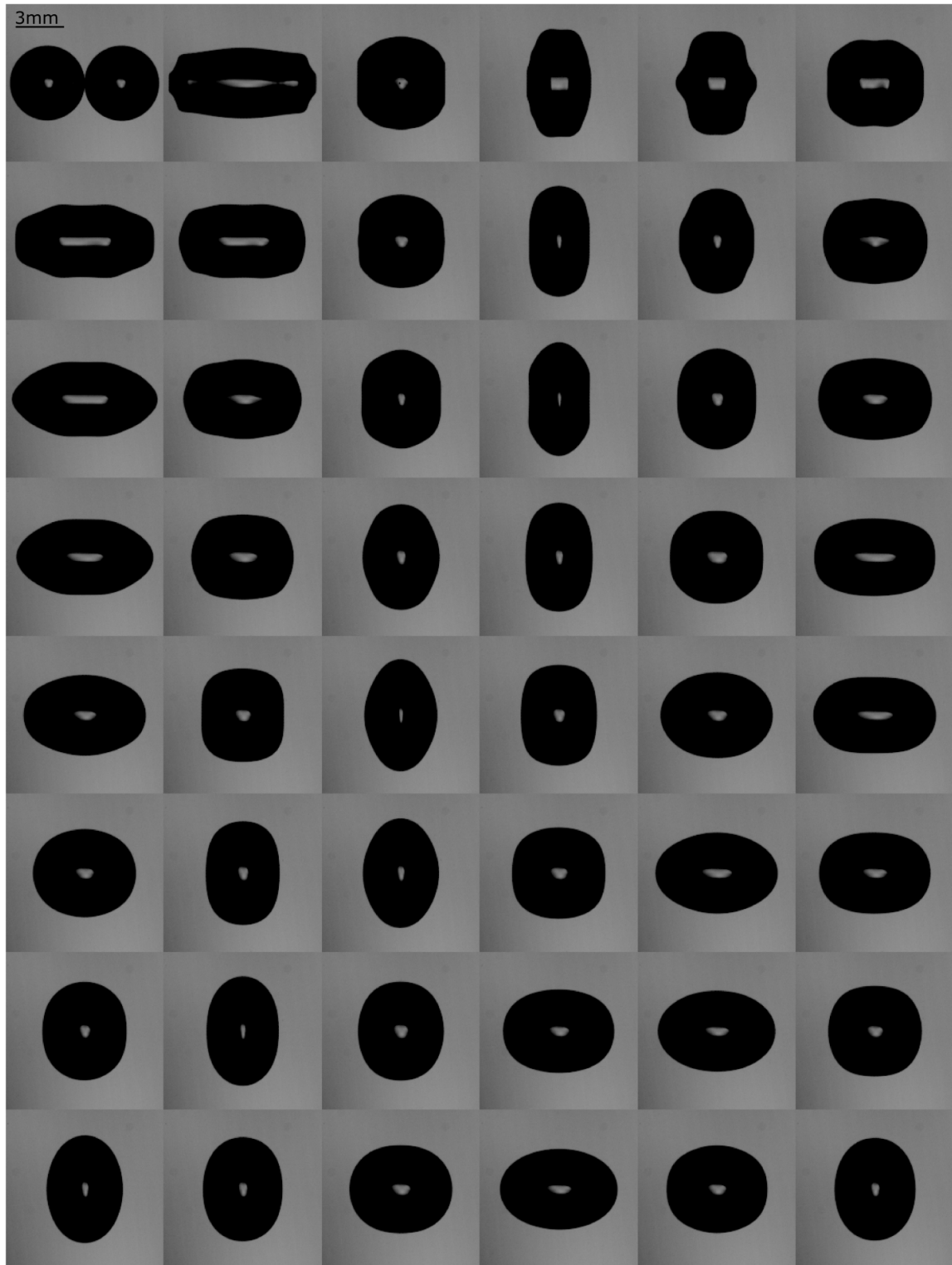


Figure 4.4: Series of images showing the coalescence of two diamagnetically-levitated air bubbles in water. The ratio of the radii of the bubbles before coalescence is equal (within experimental error). The first frame shows the stationary pair of bubbles immediately before coalescence. Time increases from left to right and from top to bottom, with an interval between each frame of  $6.8 \text{ ms}/0.35\tau_{44}$

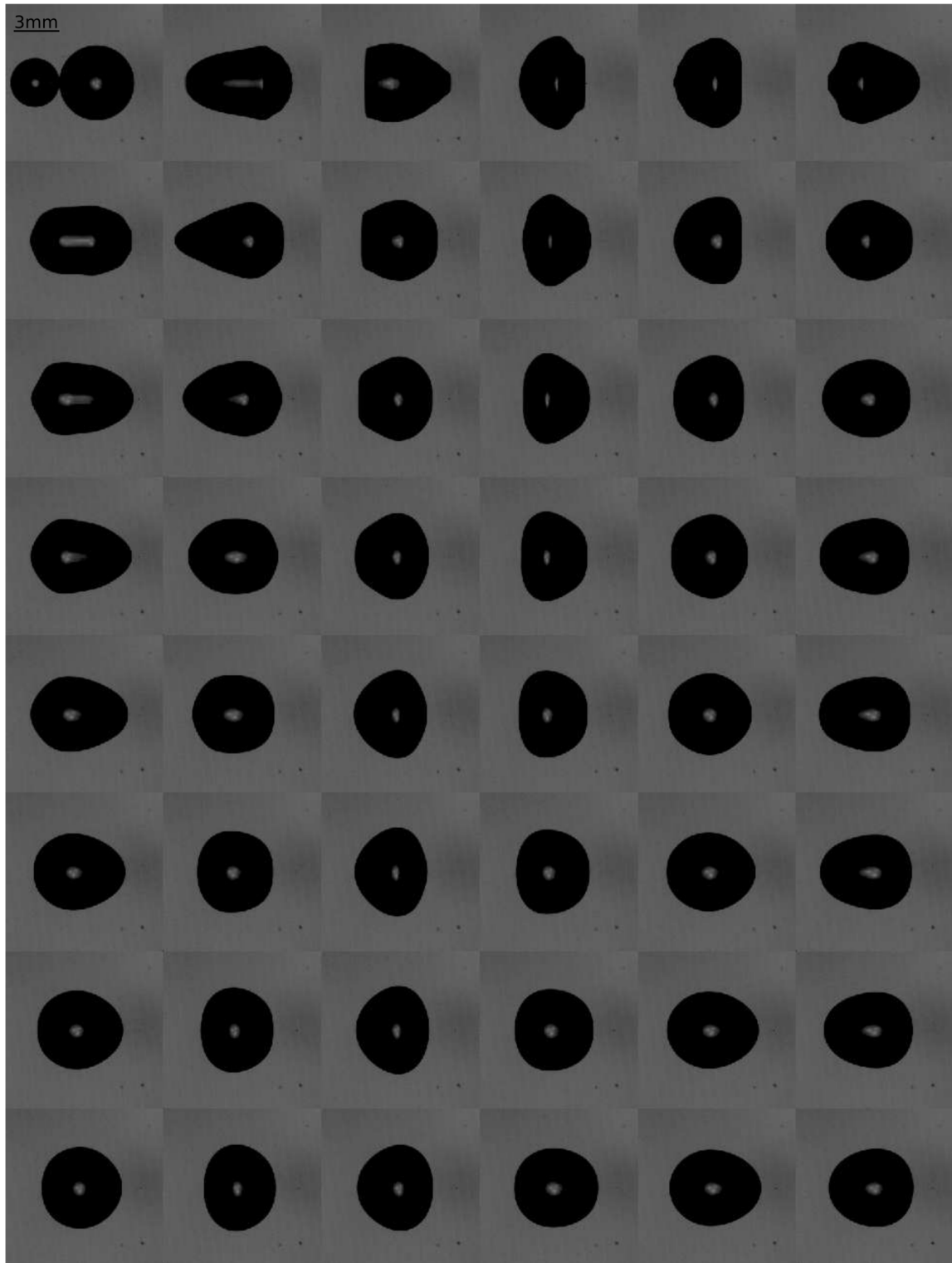


Figure 4.5: Series of images showing the coalescence of two diamagnetically-levitated air bubbles in water. The ratio of the radii of the bubbles before coalescence is approximately 2:3. The first frame shows the stationary pair of bubbles immediately before coalescence. Time increases from left to right and from top to bottom, with an interval between each frame of  $5.5 \text{ ms}/0.33\tau$ .

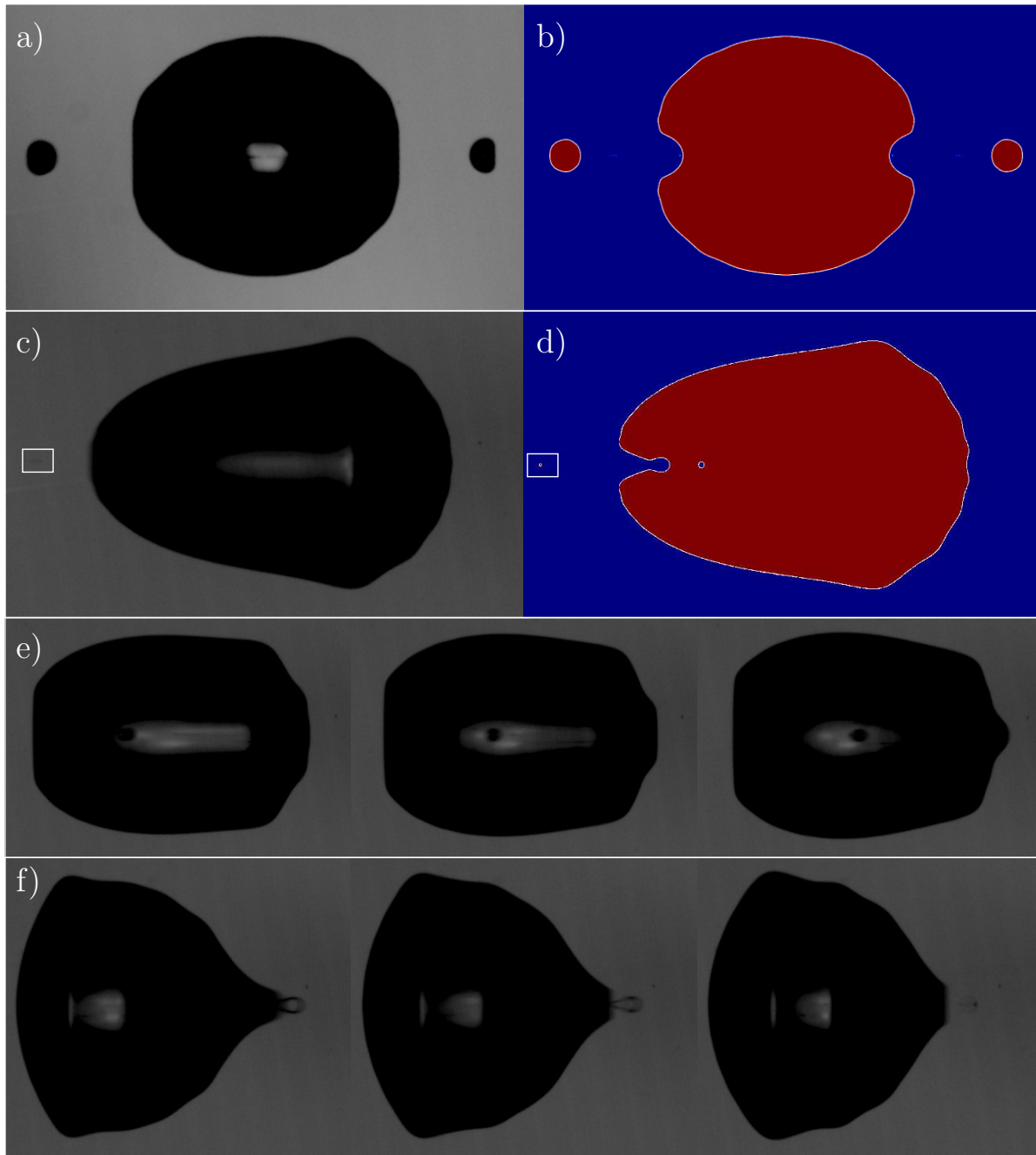


Figure 4.6: a) and b) show the double bubble ejection observed in the symmetric case, results are taken from experiment and simulation, respectively. c) and d) show the single bubble ejection observed in the asymmetric case, results are taken from experiment and simulation, respectively. The white box is to draw attention to the small satellite bubble. Results presented from simulation show a 2d slice down the centre of the bubble, allowing for a better understanding of the internal dynamics of the bubble. e) Sequence of images showing the motion of an internally ejected droplet travelling along the central axis of the coalescing bubbles. f) Sequence of images showing the creation and collapse of an antibubble at the apex of the larger of the two parent bubbles.

have radii of  $0.17 \pm 0.01R_s$  from experiment and  $0.160R_s$  from simulation. The simultaneous ejection of multiple satellite bubbles from the coalescence of equal-sized bubbles has been predicted ever since the discovery that bubble coalescence may lead to satellite bubble ejection [66], but here we present the first experimental confirmation of this. Previous experiments on bubble coalescence have failed to observe simultaneous ejection of multiple satellite bubbles due to the difficulty in trapping bubbles, as bubbles in previous experiments had to be pinned to either a surface or capillary tube [64], [65], inhibiting free surface oscillations at the apex of at least one of the parent bubbles.

In the asymmetric case, we observe the ejection of a single satellite bubble at time  $t = 0.35\tau$ , see figure 4.6c,d. We cannot experimentally identify the size of the ejected bubble as it is below the limit of the resolution of our optical set-up ( $0.017R_s$ ), but simulation finds the radius of the ejected satellite bubble to be  $0.014R_s$ .

In the asymmetric case, the internal ejection of droplets inside the bubble is also observed, in both experiment and simulation, see figure 4.6e. Due to the capillary waves formed during coalescence focusing at the apexes of the parent bubbles, the apexes of the bubbles oscillate. If the surface of the bubble at the apex is outside the initial bubble domain an unstable protrusion may form leading to the ejection of a satellite bubble, as documented above. But, if the surface of the bubble at the apex is inside the initial bubble domain a pocket of liquid may form inside the bubble which may be pinched off to form an internally ejected droplet. Internally ejected droplets are analogous to droplets produced from jets observed when a bubble bursts at a free surface [67], [68]. Neglecting gravity, a bubble bursting at a free surface is directly equivalent to the coalescence of two bubbles, where the ratio of the radius of the two bubbles is infinitely large.

Another phenomenon observed in the asymmetric case is the creation of an antibubble. An antibubble is a thin shell of gas surrounding a cavity of liquid itself surrounded by liquid, this can be seen as the opposite of a conventional soap bubble, where a thin shell of liquid surrounds a cavity of gas itself surrounded by gas [69]. Antibubbles created in bubble coalescence occur at the apex of the opposite parent bubble to which bubble ejection and internal droplet ejection occurs. Antibubbles have previously been shown to be created in bubble coalescence by Zhang and Thoroddsen [64], but the mechanism by which they form in this circumstance has not been explained. From experiment and simulation we observe that antibubbles are created due to the collision of an internally ejected droplet with the gas-liquid interface at the surface of the bubble. The droplet drags a small coating of gas with it as it penetrates the bubble surface, which then pinches off to form an antibubble. This antibubble then rapidly collapses into a ‘traditional’ gas bubble. A sequence of images showing the creation and collapse of an antibubble are shown in figure 4.6f.

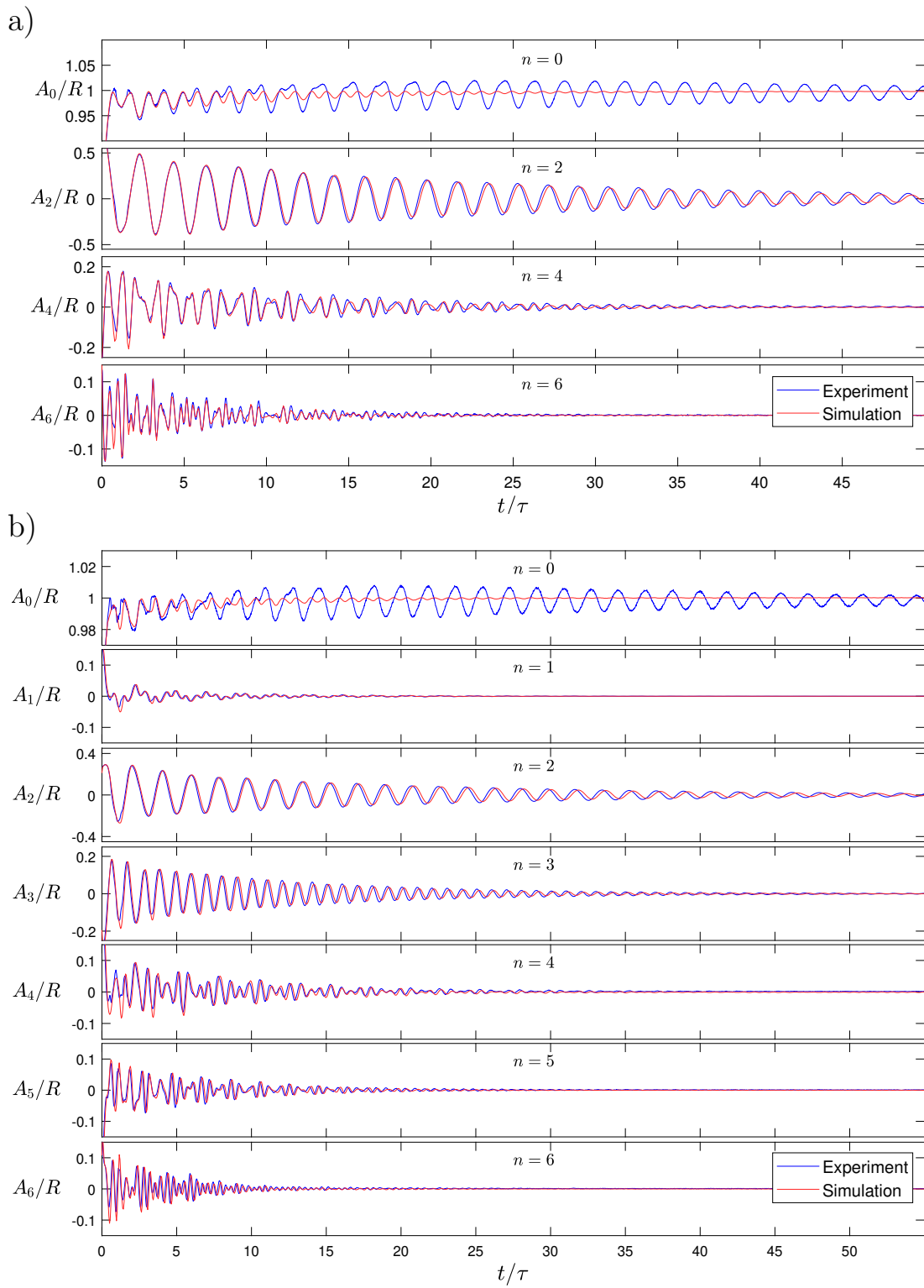


Figure 4.7: Oscillations in time,  $A_n(t)$ , of surface harmonics of degree  $n = 0-6$  for the symmetric case (a), and the asymmetric case (b). In the symmetric case (a), only oscillations of harmonics of even degree are displayed since the  $A_n$  of odd degree harmonics are negligible owing to symmetry. Note the differing scales of the vertical axes for each harmonic. Errors in experimental data are denoted by blue-shaded regions, but due to their size aren't visible on the plots.

## 4.4.2 Time series of spherical harmonics

Here, we decompose the surface contours into spherical harmonics, as described in section 4.3.4 and 3.3.1. The amplitudes  $A_n(t)$  of each spherical harmonic up to  $n = 6$  are displayed in figure 4.7. Only oscillations of the even degree harmonics have been plotted for the symmetric case (figure 4.7a), since the amplitudes of odd degree harmonics are negligible, due to the symmetry across the central plane of the bubble. The error in our experimental data is assumed to be  $\pm 5R \times 10^{-4}$  for modes  $n = 0-4$  and  $\pm 9R \times 10^{-4}$  for modes  $n = 5-6$ , as calculated in chapter 3.3.1. These errors are marked as blue-shaded regions in figure 4.7, but due to their size aren't visible.

The spherical harmonic excited with the largest initial amplitude for the coalescence of two equal-sized parent bubbles was the  $n = 2$  harmonic, with an initial amplitude  $A_2 \approx 0.5R$ . The harmonic with the next largest initial amplitude was  $n = 4$ , with  $A_4 \approx 0.2R$ . Similarly, the  $n = 2$  spherical harmonic was the harmonic excited with the largest initial amplitude by the coalescence of the unequal-sized parent bubbles, with an amplitude of  $A_2 \approx 0.3R$ . The pair of spherical harmonics with the largest initial amplitudes are much closer in value in the asymmetric case than in the symmetric case.

There is close agreement between experiment and simulation for all spherical harmonics except the  $n = 0$  harmonic, as is evident in figure 4.7. For the  $n = 0$  harmonic there is good agreement between experiment and simulation until  $t \approx 7\tau$  but thereafter, the oscillations of  $A_0(t)$  in simulation decay, which is not observed in experiment.

We may expect a difference to arise between experiments and simulations due to several factors. One being the additional magnetogravitational body forces which aren't accounted for in our simulations. But, in section 4.2 we show these forces have a negligible effect on our system. Another factor that could lead to a discrepancy between experiment and simulation is the assumption that the bubbles are axisymmetric. It is known that deviation in oscillation frequency and damping rates arise due to the breaking of the axisymmetry of bubbles [33], [70]. Calculations carried out in the supplementary information of Hunter-Brown *et al.* [46] show that the Waddell sphericity (the ratio of the surface area of a sphere with the same volume to the object's surface area) of hydrostatic bubbles of the same radii considered here only deviates from unity by values of more than  $1 \times 10^{-3}$  if the surface tension of the bubble decreases below a value of  $0.1 \text{ mN m}^{-1}$ . Since the surface tension used in experiments is approximately 700 times greater than this, it is fair to assume that the bubbles remain axisymmetric even when undergoing oscillations. The final factor that is not accounted for is the compressibility of the fluids under consideration, in particular, the air in the interior of the bubble. The simulations we performed assume incompressibility in both fluids and so do not support volume oscillations of the bubble, which is not the case in experiment. Figure 4.8 displays the non-dimensionalised volume as a function of time. From these plots it can be seen in experiment the bubbles

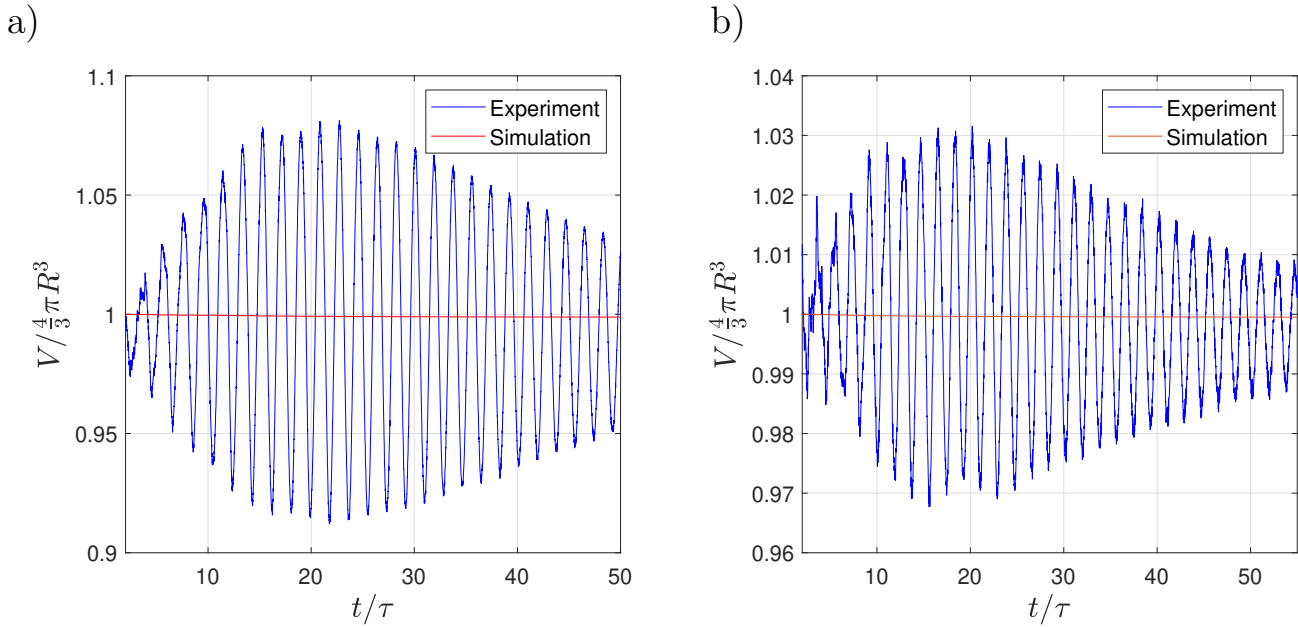


Figure 4.8: Volume as a function of time for the symmetric case (a) and the asymmetric case (b).

oscillate around their initial volume whereas in simulation volume remains constant, as expected. Since compressible effects are not accounted for in the simulations, the difference between experiment and simulation can be attributed to this.

The only notable deviation between experiment and simulation is observed in the  $n = 0$  mode for both cases, due to the compressibility of the air in experiments. This is the largest discernible difference between simulation and experiment and shows that the relatively small amplitude volume oscillations observed in experiment have a negligible effect on the shape oscillations.

It might be expected that no  $n = 0$  oscillations would be present in the simulations, given the incompressibility of the simulated gas, but this would only be true if the amplitudes of the shape oscillations were vanishingly small. If we consider a bubble with a purely axisymmetric  $n = 2$  perturbation, the equation for the surface of the bubble can be written as

$$r = A_0(t)P_0(\theta) + A_2(t)P_2(\theta) = A_0(t) + A_2(t)P_2(\theta).$$

By enforcing conservation of volume it follows that

$$V = \frac{2\pi}{3} \int_0^\pi r^3 \sin \theta d\theta = \frac{4\pi}{3} \left( A_0(t)^3 + \frac{3}{5}A_2(t)^2 A_0(t) + \frac{2}{35}A_2(t)^3 \right).$$

Hence, for the volume to remain constant  $A_0(t)$  must necessarily be time dependent. This is well demonstrated in simulation, as initially the surface harmonics  $n = 2$  and  $n = 4$  in the symmetric case, and  $n = 2$  and  $n = 3$  in the asymmetric case, have

Peaks	$a$	$a_0^*$	$a_2^*$	$a_4^*$	$b$	$b_4^*$	$b_6^*$	$c$	$d$	$d_0^*$	$d_2^*$	$d_4^*$	$e$	$e_0^*$	$e_4^*$	$e_6^*$	$f$	$g$	$h$
Experiment	3.4	6.5	6.6	6.5	9.3	18.7	18.7	15.7	3.4	6.8	6.8	6.8	6.2	12.2	12.4	12.3	9.3	12.8	16.2
Simulation	3.4	6.5	6.6	6.5	9.3	18.8	18.7	15.9	3.4	6.7	6.8	6.8	6.2	12.2	12.3	12.3	9.3	12.8	16.1

Table 4.2: Frequencies,  $\omega\tau$ , of the peaks labelled in figure 4.9.

amplitudes which are a significant fraction of the bubble radius. As the amplitude of these surface harmonics decay the amplitude of the  $n = 0$  harmonic tends to zero, as can be seen in figure 4.7. Since the simulations do not account for gravity or the body forces applied by the magnet, the good agreement with experiment (excepting  $n = 0$ ) is also further evidence that the forces involved in the levitation have no significant effect on the oscillations of the bubble.

### 4.4.3 Fourier transforms of time series

Figure 4.9 shows the amplitude of the Fourier transform of each of the time series shown in figure 4.7, with the exception of a short initial period  $t < 1.5\tau$  immediately after coalescence, as during this period the surface contour  $r(\theta, t)$  is not guaranteed to be single valued. As in subsection 4.4.2, the error in the amplitude of our experimental data is assumed to be  $\pm 5R \times 10^{-4}$  for modes  $n = 0-4$  and  $\pm 9R \times 10^{-4}$  for modes  $n = 5-6$ . The errors are denoted in figure 4.9 by the blue-shaded regions. These errors are purely errors in the amplitude of the experimental data and hence don't affect the location of peaks in the spectra. The error in  $\omega$  for both experiment and simulation is  $\pm 0.05\tau^{-1}$ . These small errors occur due to the fast Fourier transform algorithm used to process the time series.

We have labelled some of the peaks in the spectra with letters  $a-h$ . Since the oscillations decay in time, the magnitudes of the peaks shown in the Fourier transform of the whole time series are smaller than the initial amplitudes given in table 4.2. For example, the magnitude of the peak labelled  $a$  in the frequency spectrum of the  $n = 2$  harmonic is approximately  $0.15R$ , compared to an initial amplitude of  $A_2 \approx 0.5R$ . The spectra also conceal any changes in frequency with time, except through a broadening of the peaks.

For a bubble undergoing mode  $n$  oscillations, T&B's solution consists of a surface harmonic of degree  $n$  and amplitude  $\varepsilon$  oscillating with frequency  $\omega_n$ , with additional even mode surface harmonics of  $0-2n$  of amplitude of order  $\varepsilon^2$  and frequency  $2\omega_2$ , see equation (4.3). Hence, for a bubble undergoing mode  $n$  oscillations, T&B's model predicts a peak in the frequency spectra of the surface harmonic of order  $n$  at a frequency  $\omega_n$  and peaks in the frequency spectra of even order harmonics up to  $2n$  at a frequency of  $2\omega_n$ .

We now compare our results with T&B's theoretical prediction for the moderate amplitude oscillations of a bubble. In the symmetric case, the spectrum of the  $n = 2$  surface harmonic shows a peak ( $a$ ) at a frequency close to  $\omega_2^{(0)}$ . Additional smaller peaks, labelled  $a_n^*$ , are evident at a frequency close to  $2\omega_2^{(0)}$  in the spectra of the  $n = 0$ ,  $n = 2$ , and  $n = 4$  harmonics, respectively. Equivalent features are also

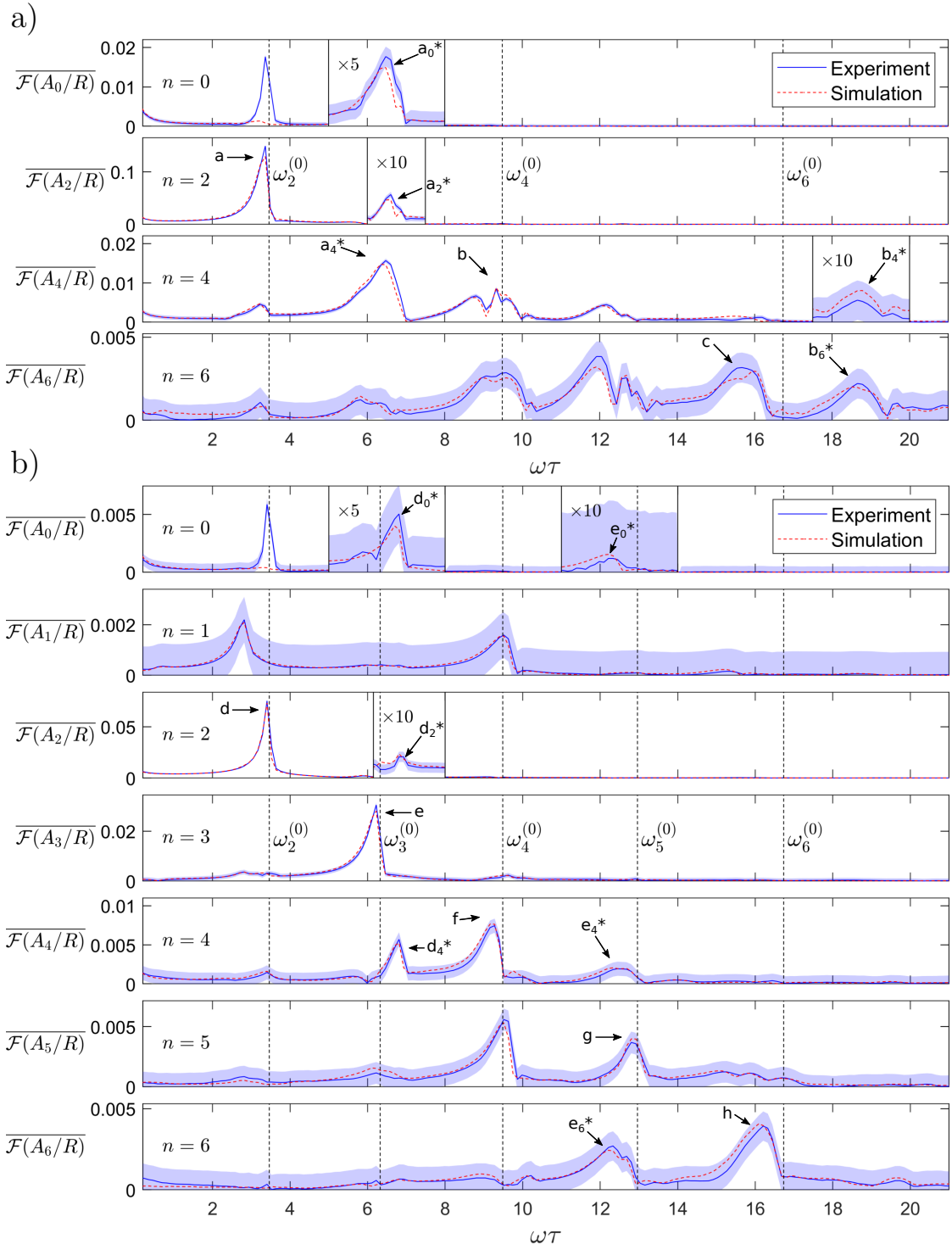


Figure 4.9: Fourier transforms of the time series shown in figure 4.7, for the symmetric case (a), and the asymmetric case (b). Dashed lines indicate the frequencies of the linear modes of oscillation,  $\omega_n^{(0)}$ . It should be noted that different harmonics have different scales for the vertical axes. The vertical scale is magnified in some sections, as indicated. Blue-shaded regions denote errors in the experimental data.

	$n = 2$		$n = 3$			$n = 4$			
$k$	2	4	2	4	6	2	4	6	8
$c_k$	0.167	0.620	0.046	0.279	0.708	0.018	0.043	0.056	0.735

Table 4.3: Values for coefficients  $c_k$  found in equation (4.3) for modes  $n = 2-4$ . These have been taken from equations (57a), (58a) and (59a) of T&B.

observed in the asymmetric case with the main peak, labelled  $d$ , close to  $\omega_2^{(0)}$  and additional secondary peaks, labelled  $d_n^*$ , close to  $2\omega_2^{(0)}$ .

For convenience, we introduce the notation  $\overline{\mathcal{F}}(x)$  to refer to the amplitude of peak  $x$ , e.g.  $\overline{\mathcal{F}}(a) = 3.4$ , refers to the amplitude of peak  $a$  which appears in the frequency spectra of the  $n = 2$  surface harmonic. We find the ratios of the peak amplitudes  $\overline{\mathcal{F}}(a_n^*)/\overline{\mathcal{F}}(a)^2$  and  $\overline{\mathcal{F}}(d_n^*)/\overline{\mathcal{F}}(d)^2$  measured from the spectra are in reasonable agreement with the prediction of T&B for the coefficients  $c_k$  in equation (4.3). For completeness, we give the values of these coefficients in table 4.3. For example, we measure  $\overline{\mathcal{F}}(a_4^*)/\overline{\mathcal{F}}(a)^2 \approx 0.90 \pm 0.05$  in simulation and  $0.70 \pm 0.05$  in experiment, compared to a value of 0.620 predicted by T&B (see table 4.3,  $n = 2$ ,  $k = 4$ ).

In the spectrum of the  $n = 3$  harmonic, for the asymmetric case, we observe a sharp peak labelled  $e$ , at  $\omega_3 \approx \omega_3^{(0)}$ . Smaller peaks, at approximately  $2\omega_3 \approx 2\omega_3^{(0)}$  can also be seen in the spectra of the  $n = 0, 4$  and  $6$  harmonics, labelled  $e_n^*$ , respectively. Although, a clear peak is not observed near  $2\omega_3^{(0)}$  in the  $n = 2$  harmonic. The amplitude  $\overline{\mathcal{F}}(e_3^*)$  is approximately two times larger than expected, and  $\overline{\mathcal{F}}(e_6^*)$  approximately 4 times larger.  $\overline{\mathcal{F}}(e_4^*)$  is much larger than expected, by about two orders of magnitude.

In the spectrum of the  $n = 4$  harmonic, for both symmetric and asymmetric cases, we observe a peak at  $\omega_4 \approx \omega_4^{(0)}$  ( $b$  and  $f$  respectively). In the symmetric case, peaks at approximately  $2\omega_4 \approx 2\omega_4^{(0)}$  are observed in the spectra of the  $n = 4$  and  $6$  harmonics labelled  $b_n^*$ , although similar peaks are not observed in the asymmetric case. The amplitudes  $\overline{\mathcal{F}}(b_n^*)$  are inconsistent with the predictions of T&B: our measured values of  $\overline{\mathcal{F}}(b_4^*)$  and  $\overline{\mathcal{F}}(b_6^*)$  are about two orders of magnitude larger than expected. In the asymmetric case, we were unable to clearly identify any peaks near  $2\omega_4$  in the spectra of any surface harmonic.

In the spectrum of the  $n = 5$  harmonic (asymmetric case) a peak  $g$  is present at  $\omega_5 \approx \omega_5^{(0)}$  corresponding to the mode 5 oscillation and in the spectrum of the  $n = 6$  harmonic for both the symmetric and asymmetric cases, a peak is present at  $\omega_6 \approx \omega_6^{(0)}$  corresponding to mode 6 oscillations. Here, peaks are labelled  $c$  and  $h$  in the symmetric and asymmetric case, respectively.

Peaks  $a-h$  lie at frequencies 2–3% lower than the frequencies of the corresponding linear modes of oscillation,  $\omega_n^{(0)}$ . The peaks at  $2\omega_n$ , marked by the asterisks, also lie at frequencies slightly lower than  $2\omega_n^{(0)}$ . This observation is consistent with the theory of T&B, which predicts a shift to lower frequency with increasing amplitude  $\varepsilon$  of the mode (equation (4.3)).

As well as the labelled peaks, additional peaks are also observed in the frequency spectra of the surface harmonics. These additional peaks are not expected from the theory of T&B (equation (4.3)). The fact that these features are reproduced almost identically in both simulation and experiment indicates that they are not an artefact of the experimental method, nor a defect of the simulations. We find that a number of these additional peaks may be explained by accounting for shape corrections up to third-order, as calculated in the appendices of Hunter-Brown *et al.* [46]. It is shown in Hunter-Brown *et al.* [46] that third-order corrections predict additional contributions to the  $n = 2$  oscillation mode at third order in amplitude from surface harmonics of degree  $n = 0, 4$  and  $6$  oscillating at a frequency  $\omega_2$ , and  $n = 0, 2, 4$  and  $6$  oscillating at frequency  $3\omega_2$ . In the symmetric case, we observe peaks at frequencies close to  $\omega_2^{(0)}$  in the spectra of the  $n = 4$  and  $n = 6$  harmonics. The amplitudes of these two peaks agree roughly with the theoretical prediction, being approximately 2 times larger than predicted. There is also a peak at  $\approx \omega_2^{(0)}$  in the  $n = 0$  harmonic but here the results of simulations and experiment differ considerably due to volume oscillations supported by the bubble in experiment. Peaks close to  $\sim 3\omega_2$  are also observed in the frequency spectra of the  $n = 4$  and  $6$  harmonics with amplitudes 1–2 times larger than predicted. The existence of a component at  $3\omega_2$  in the  $n = 4$  harmonic could explain the split-peak appearance of the feature at  $b$ , as  $3\omega_2^{(0)} \approx 1.1\omega_4^{(0)}$ . In the asymmetric case, the agreement between our experimental and simulation results and the predicted third-order corrections is less good in the asymmetric coalescence than in the symmetric case; whilst we do observe peaks at  $\omega_2$  and  $3\omega_2$  in the spectra as predicted, their amplitudes are 5–10 times larger than expected.

#### 4.4.4 Time-frequency analysis of time series

To study the dependence of the oscillation frequency of a given mode on amplitude, we performed time-frequency analysis on the oscillations of each surface harmonic,  $A_n(t)$ . We obtained the short-time Fourier transform (STFT) of  $A_n(t)$ , using a Hanning window [71] of duration 300 ms which was shifted in steps of 5 ms across the time domain. Time-frequency plots for the harmonics of degree  $n = 2-4$  are presented in figure 4.10.

In the symmetric case, the STFT of the  $n = 2$  surface harmonic shows a dominant peak at approximately  $\omega_2^{(0)}$  which corresponds to peak  $a$  in the Fourier transform shown in figure 4.9a. The two prominent features in the STFT of the  $n = 4$  surface harmonic are a peak at approximately  $2\omega_2^{(0)}$ , corresponding to  $a_4^*$  in figure 4.9a and a second broader feature at approximately  $\omega_4^{(0)}$ , corresponding to  $b$  in figure 4.9a. In all cases, the STFTs show that peaks move to higher frequency with increasing time, for both data obtained from experiment and simulation. In the asymmetric case, the STFT of the  $n = 2$  surface harmonic shows a peak at approximately  $\omega_2^{(0)}$ , as in the symmetric case. Here, this peak corresponds to the peak labelled  $d$  in figure 4.9b. The STFT of the  $n = 3$  surface harmonic shows a prominent peak at approximately

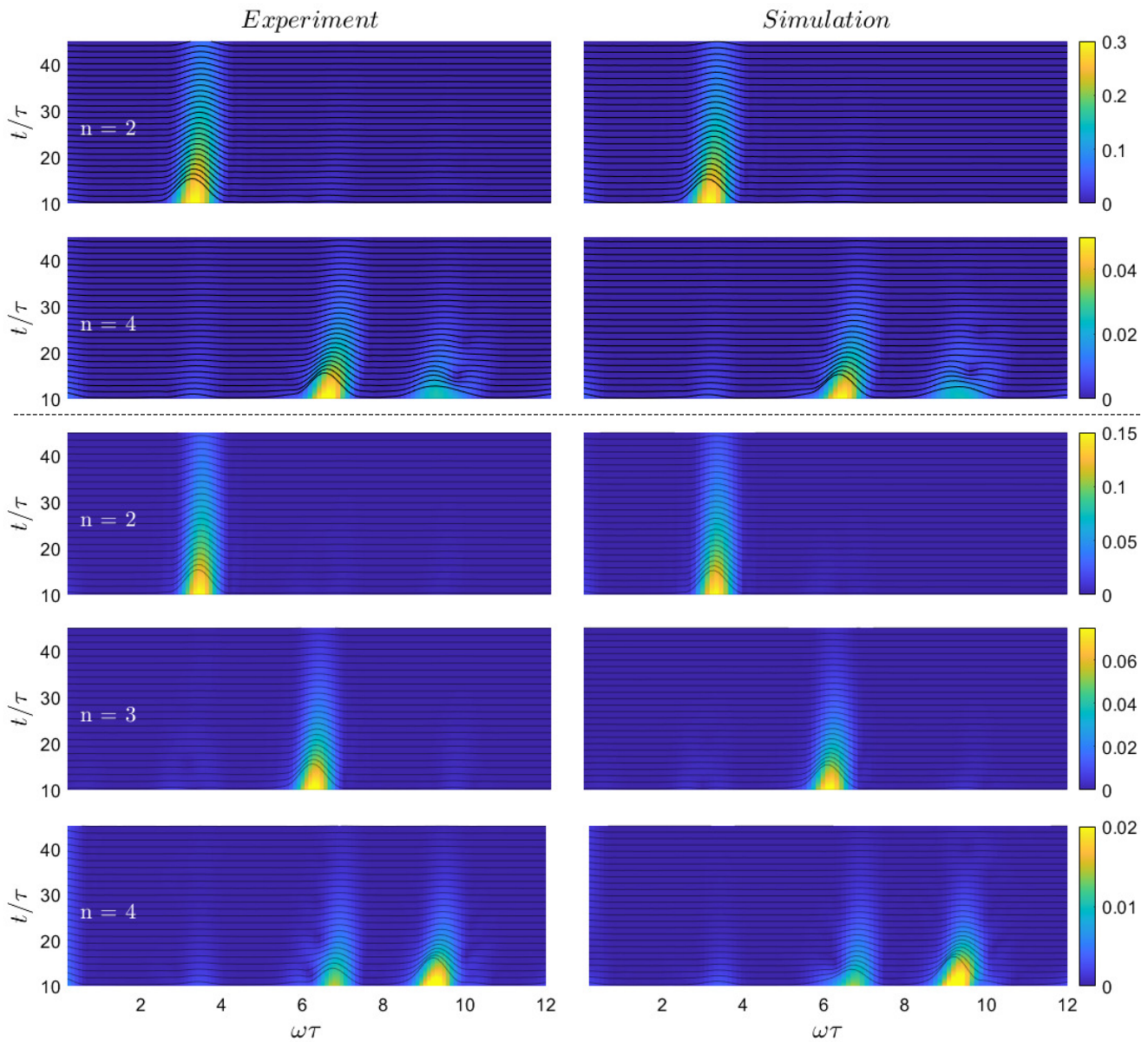


Figure 4.10: Short-time Fourier transforms of the time series in figure 4.7, for surface harmonics  $n = 2-4$ . The upper plots (above the dashed line) show the results for the symmetric case and the lower plots show the results for the asymmetric case. The solid black curves show the same data overlaid in the form of a waterfall plot. Note that colour scales vary between plots.

$\omega_3^{(0)}$  corresponding to the peak labelled *e* in figure 4.9b. The two most conspicuous peaks in the STFT of the  $n = 4$  surface harmonic, at approximately  $2\omega_2^{(0)}$  and  $\omega_4^{(0)}$ , correspond to *d*<sub>4</sub><sup>\*</sup> and *f* in figure 4.9b. As in the symmetric case, these peaks also all move to higher frequency with increasing time.

For both simulation and experiment, we measured the amplitude  $\varepsilon_n^* R$  and frequency  $\omega_n$  of the dominant peak in the  $n = 2$  spectrum in both symmetric and asymmetric cases, and the dominant peak in the  $n = 3$  spectrum in the asymmetric case. (The asterisk here is used as an indicator that  $\varepsilon_n^*$  is measured from the STFT.) From this, we calculated the depression in the frequency of oscillation of modes 2 and 3,  $\omega_n - \omega_n^{(0)}$ , as a function of their amplitudes,  $\varepsilon_n^*$  (figure 4.11). Figure 4.12 shows the derivative of the frequency with respect to the amplitude squared, allowing for comparison with the values of  $\omega_n^{(2)}$  obtained by T&B. To calculate the gradients  $d\omega_n/d\varepsilon_n^{*2}$  a new set of frequency values were interpolated from the original frequency data sets at evenly spaced values of  $\varepsilon_n^{*2}$ . The error in the experimental values of  $\varepsilon_n^{*2}$  is at maximum  $\pm 3.4 \times 10^{-4}$ , which occurs at  $\varepsilon_n^{*2} \approx 0.12$  and is directly proportional to  $\varepsilon_n^*$ . Since the errors in the experimental values of  $\varepsilon_n^*$  are at least 3 orders of magnitude less than the actual value, it is safe to assume they have a negligible effect on our results.

Our simulations of the symmetric case are in reasonable agreement with the results predicted by the theoretical model of T&B for mode 2 oscillations. From figures 4.11 and 4.12 it can be seen that the frequency varies approximately linearly with  $\varepsilon_2^{*2}$ . For values of  $\varepsilon_2^{*2} \lesssim 0.09$  we obtain a value of  $\omega_2^{(2)} \approx 1.4\omega_2^{(0)}$ , compared with the value predicted by T&B of  $1.526\omega_2^{(0)}$ . The simulation data show a slight increase in  $\omega_2^{(2)}$  at higher  $\varepsilon_2^{*2}$ , rising to approximately  $1.6\omega_2^{(0)}$  at  $\varepsilon_2^{*2} = 0.11$ . Our experimentally-measured value of  $\omega_2^{(2)}$  is smaller than the values found in simulation for small  $\varepsilon_2^{*2}$ . Here, we find that approximately  $1.2\omega_2^{(0)}$  for  $\varepsilon_2^{*2} \lesssim 0.02$ , rising to  $\omega_2^{(2)} \approx 1.75\omega_2^{(0)}$  at  $\varepsilon_2^{*2} = 0.11$ . For the asymmetric case, we obtain a value of  $\omega_2^{(2)} = 1.5\omega_2^{(0)}$  in the limit  $\varepsilon_2^{*2} \rightarrow 0$ , consistent with the predicted result. However, unlike in the symmetric case, we find that frequency does not vary linearly with  $\varepsilon_2^{*2}$ : the value of  $\omega_2^{(2)}$  increases nonlinearly with  $\varepsilon_2^*$ , rising to approximately 3.5 at  $\varepsilon_2^{*2} = 0.025$ . Both simulation and experiment are in good agreement. Corrections due to neglected terms  $O(\varepsilon^4)$  cannot account for this large deviation, since measured values of  $\varepsilon_2^{*2}$  are less than 0.025 in this case. For the  $n = 3$  mode (asymmetric case), we observe that the frequency also does not vary linearly with  $\varepsilon_2^{*2}$ . Values obtained for  $\omega_3^{(2)}$  are considerably larger than predicted, approximately  $9.5\omega_3^{(0)}$  in the limit  $\varepsilon_3^* \rightarrow 0$  compared to the theoretical value of  $2.3\omega_3^{(0)}$ . Simulation and experiment both show a sharp drop in the measured value of  $\omega_3^{(2)}$  to approximately  $5.8\omega_3^{(0)}$  at  $\varepsilon_3^{*2} \approx 0.025$ , followed by a rise toward a value of  $9.0\omega_3^{(0)}$  at  $\varepsilon_3^{*2} = 0.065$ . To summarise, our measurements of  $\omega_2^{(2)}$  are comparable with the theoretically predicted value in the symmetric case, but agree in the asymmetric case only in the limit  $\varepsilon_n^* \rightarrow 0$ . Our measurements of  $\omega_3^{(2)}$  are 2.5–4 times larger than predicted, depending on  $\varepsilon_n^*$ . We

note that a similar discrepancy was found for the mode 3 second order frequency coefficient obtained for the non-linear oscillations of soap-film bubbles by Kornek *et al.* [56].

From figures 4.11 and 4.12, it is clear there is a noticeable difference between our results and theoretical predictions in the asymmetric case, in comparison to the reasonable agreement observed for the symmetric case. This could be explained by interactions between the modes in the asymmetric case. From our experiment and simulation of the coalescence of two equal-sized parent bubbles, we find the resulting oscillations to be dominated by the contribution from the mode 2 oscillation. The mode with the next highest amplitude is the mode 4 oscillation, the contribution of mode 3 being negligible in this case due to symmetry. The ratio of the amplitudes of the two modes is approximately  $\varepsilon_4^*/\varepsilon_2^* \approx 0.08$  at  $t = 10\tau$  dropping to  $\varepsilon_4^*/\varepsilon_2^* \approx 0.05$  at  $t = 20\tau$  as the higher frequency mode 4 oscillations damp more quickly. Thus the coalescence of two equal-sized bubbles produces oscillations which decay to (approximately) mode 2 oscillations considered by T&B after approximately  $10\tau$ . In contrast, from our experiment and simulation of the coalescence of unequal-sized parent bubbles, we find oscillations with comparable contributions from two modes,  $n = 2$  and  $n = 3$ . In the case considered here, the ratio of the amplitudes of these two modes are  $\varepsilon_3^*/\varepsilon_2^* \approx 0.50$  at  $t = 10\tau$ , dropping to  $\varepsilon_3^*/\varepsilon_2^* \approx 0.38$  by  $t = 20\tau$ . Thus the contribution of the next highest amplitude mode (mode 3 in this case) is both proportionally much greater than in the symmetric coalescence, and the ratio between the two decreases more slowly with increasing time, owing to the weaker viscous damping of mode 3 oscillations compared to mode 4. Hence, since T&B studied oscillations consisting of a single mode, it is reasonable to assume that the discrepancy arises between our results and theory in the asymmetric coalescence owing to coupling between different modes of comparable amplitude, in the asymmetric case this is modes  $n = 2$  and  $n = 3$ .

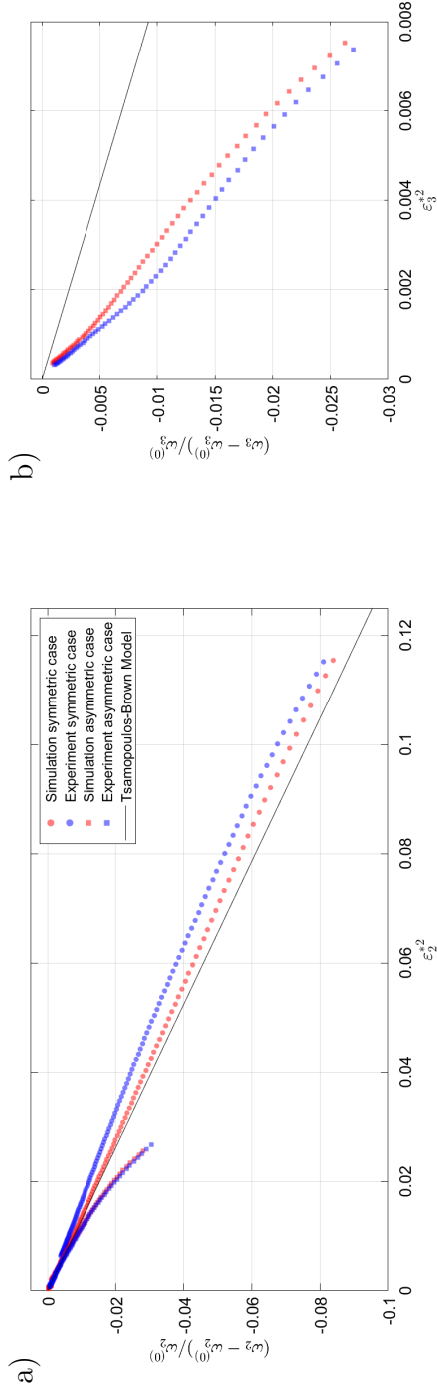


Figure 4.11: Fractional change of the measured frequencies of mode 2 (a) and mode 3 (b) as a function of the square of the amplitudes  $\epsilon_n^*$  of each mode, from experiment and simulation. The unbroken black line shows the prediction of the T&B model.

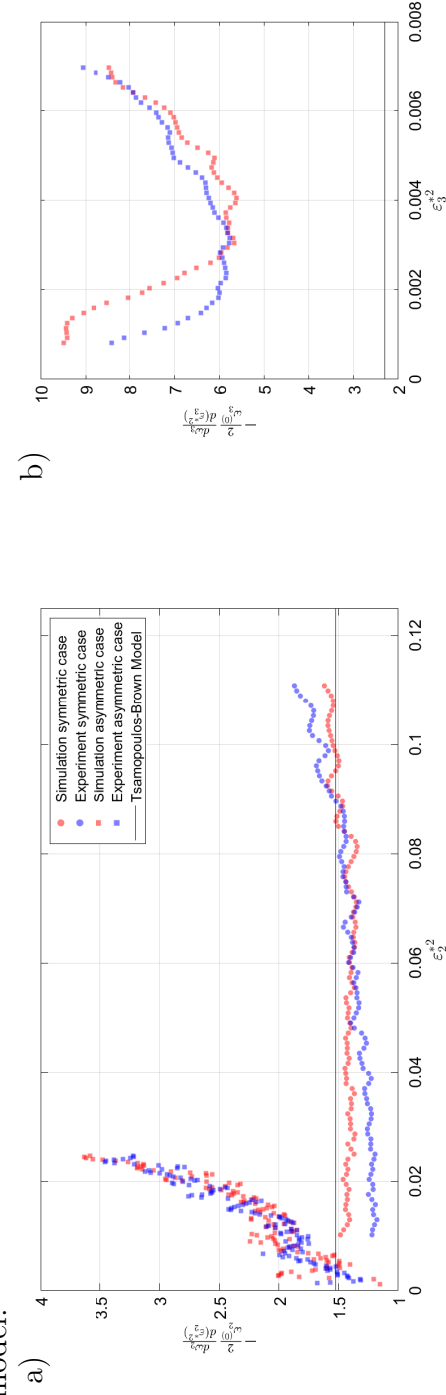


Figure 4.12: Rate of change of the measured frequencies of mode 2 (a) and mode 3 (b) with  $\epsilon_n^{*2}$ . The rate has been scaled by a factor of  $(-2)/\omega_n^{(0)}$  for comparison with the values of  $\omega_n^{(2)}$  obtained by T&B (horizontal black lines).

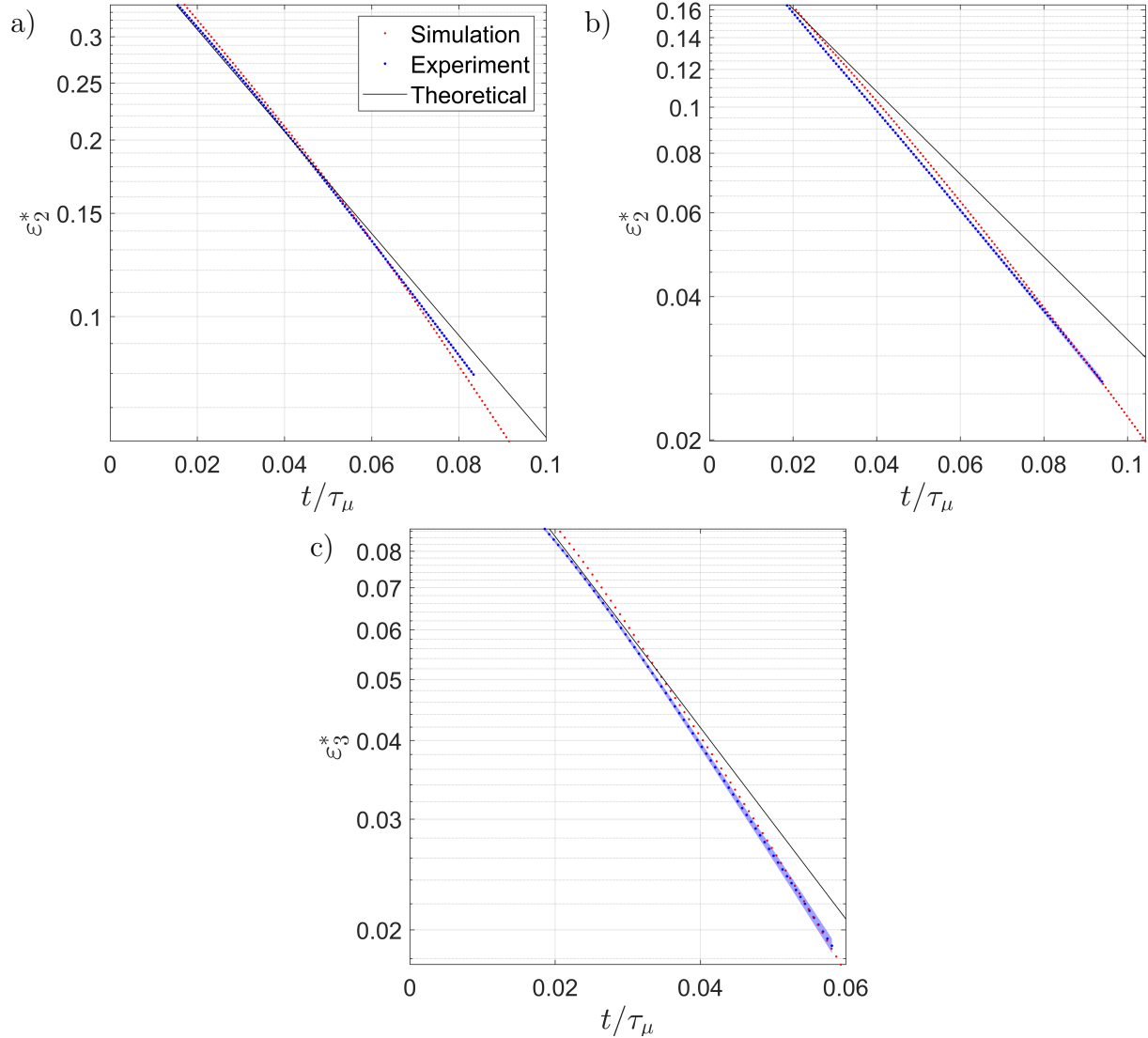


Figure 4.13:  $\epsilon_n^*$  vs time for symmetric case mode 2 (a), asymmetric case mode 2 (b), and asymmetric case mode 3 (c). Time here is non-dimensionalised with the viscous time scale. The blue-shaded regions denote the error in the experimental data. Black lines show the theoretical damping rates of Lamb, where  $\alpha_2 = 20\tau_\mu$  and  $\alpha_3 = 35\tau_\mu$ .

#### 4.4.5 Viscous damping

Here, we discuss the effect that viscosity has on the amplitude of surface oscillations. Energy in the system is dissipated due to viscous shearing between adjacent fluid layers, hence we expect the total energy of the system to decrease as a function of time and therefore the amplitude of surface oscillations to decay as a function of time. To analyse this effect we plot the peak amplitude of modes  $n = 2$  and  $n = 3$  as a function of time, see figure 4.13. In this case time has been scaled by the viscous timescale  $\tau_\mu = \frac{\rho_2 R^2}{\mu}$  and the vertical axes have been plotted on a logarithmic scale.

Small amplitude normal mode surface oscillations of bubbles surrounded by fluids of low viscosity decay exponentially at a constant rate, given by equation (4.2). From figure 4.13 it is clear that observed damping rates are not constant, although the damping rates found from experiment and simulation are of similar magnitude to the theoretical damping rates. It is not anticipated that damping rate would be constant in either experiment or simulation at early times as the assumptions required for the theory of Lamb [47] to hold are not met: the oscillation amplitude is asymptotically small, the viscous boundary layer is asymptotically thin, and the fluid inside the bubble is inviscid with zero density. Figure 4.13 shows that the general trend for the rate of damping is to increase as a function of time. Qualitatively similar results are found between experiment and simulation, although the increase in the rate of damping is greater in simulation than in experiment. This is due to the fact numerical damping occurs in simulation which increases the perceived damping rate.

A comparison between the rate of damping for mode 2 between the symmetric and asymmetric cases shows an increased rate of damping in the asymmetric case. This may suggest that nonlinear mode coupling may affect the rate of damping, but a more in-depth study would be required to verify this.

#### 4.4.6 Translational motion of bubbles due to oscillation

It has been shown that coupling of modes of adjacent degree may lead to motion of the centre of mass of a bubble [72]–[74]. Due to the symmetry plane down the centre of the bubble in the symmetric case, only even degree modes are excited, hence no adjacent modes undergo oscillation, therefore we observed no motion of the centre of mass in either experiment or simulation in this case. Figure 4.14 shows the displacement of the centre of mass along the symmetry axis of the bubble as a function of time, for the asymmetric case. The origin of the system is taken to be at the centre of mass of the bubble at the start of coalescence. For  $t < 7\tau$  there is good agreement between experiment and simulation, which both show an oscillation about its initial position, with an amplitude  $\sim 0.1R$  and period  $2.5\tau$ , with an additional background drift in the direction of the smaller of the two parent bubbles.

The results of simulation and experiment begin to diverge after  $t = 7\tau$  as in simulation the centre of mass continues to drift in the same direction, whereas in experiment this ‘drift’ reverses direction after approximately  $t = 10\tau$ , due to the restoring force experienced by the bubble from the magnetogravitational trap.

## 4.5 Summary

In this chapter, we have used magnetic levitation to study the coalescence of air bubbles in water. Together with numerical simulation, we investigated the nonlinear axisymmetric surface oscillations of 5–6 mm-diameter bubbles generated from the

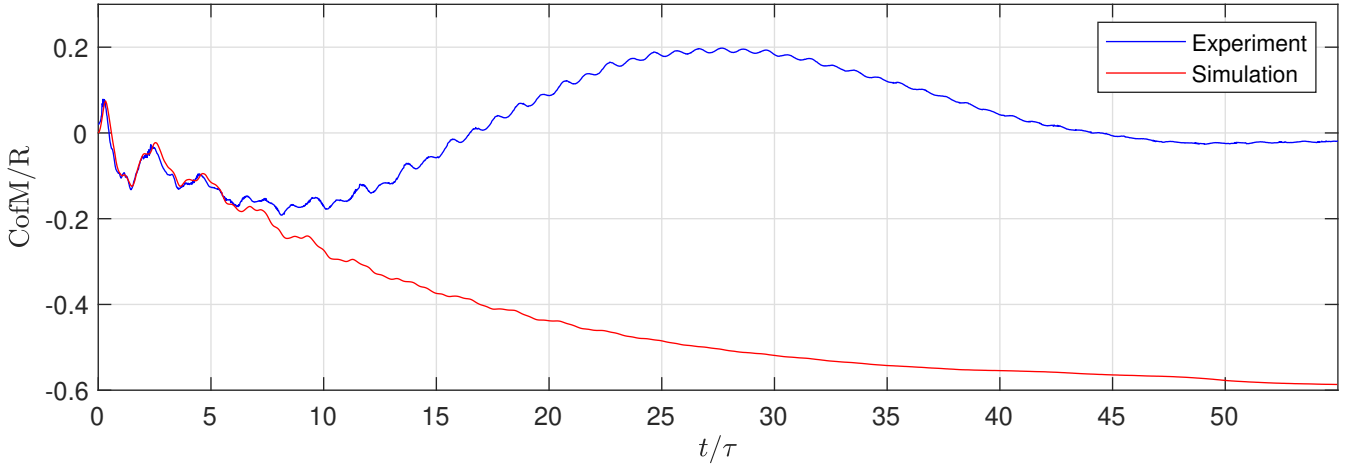


Figure 4.14: Position of the centre of mass of the bubble along its axis of symmetry, for the asymmetric case.

coalescence of two-parent bubbles. Good agreement was found in general between our experimental results and simulations.

Experimental confirmation of the simultaneous ejection of two satellite bubbles is presented here for the first time. As well as this, we show that internally ejected droplets penetrating the surface of the bubbles during the bubble coalescence process may lead to the formation of antibubbles. Providing the mechanism for the formation of antibubbles observed during bubble coalescence.

Analysis of the spherical surface harmonics of the oscillations showed that the coalescence of two equal-sized parent bubbles produced a single bubble undergoing ‘moderate–large’ amplitude oscillations dominated by a single mode of oscillation,  $n = 2$ , approximating the idealised situation considered by T&B. Whereas, coalescence of two unequal-sized parent bubbles, produced oscillations with comparable contributions from both mode 2 and mode 3 shape oscillations. We observed peaks in the frequency spectra of the time series of surface harmonics consistent with T&B’s predicted corrections to the  $n = 2$  bubble shape at second order, and also with predicted shape corrections at third order. The amplitudes of these peaks are in reasonable agreement with theoretical prediction, except for some of the third-order peaks in the asymmetric case. We also observed peaks in the spectra at frequencies in agreement with some of the predicted second and third-order shape corrections of modes  $n > 2$ , but with amplitudes inconsistent with theory.

Time-frequency analysis of the shape oscillations produced from the coalescence of two equal-sized parent bubbles showed that in this case, the frequency of the  $n = 2$  mode oscillation behaves as a function of the square of the amplitude, in reasonable agreement with T&B’s theoretical prediction, in both experiment and simulation. Time-frequency analysis of the shape oscillations produced from the coalescence of two unequal-sized parent bubbles showed that the variation of the frequencies of the

$n = 2$  and  $n = 3$  modes with amplitude was inconsistent with T&B's prediction. For the  $n = 2$  mode it was found that in the limit that amplitude tended to zero, the second-order frequency coefficient approached the theoretically predicted value, but for the  $n = 3$  mode values were found to be more than three times as large as theoretically predicted.

In summary, where the oscillations we observe in simulation and experiment are dominated by a single mode our results are consistent with T&B's prediction for the corrections to the bubble shape oscillations at second order in amplitude, including the predicted depression of the oscillation frequency proportional to the square of the amplitude, and also with our predicted correction to the bubble shape oscillations at third order in amplitude. Where there is more than one mode undergoing moderate-large amplitude oscillations our results indicate the presence of strong coupling between the modes. This suggests that the theory of T&B captures all the significant features of nonlinear surface oscillations of bubbles, but an improved theoretical model is needed to accurately quantify these features if several modes are undergoing moderate/large amplitude surface oscillations. It is suggested that an approach using the unified transform method as carried out for droplets by Plümacher *et al.* [75] may capture the features of non-linear mode coupling not present in the model of T&B.

# Chapter 5

## Contactless manipulation of bubble clusters

Liquid foams are complex multiphase fluid systems where bubbles/droplets of one fluid species, most commonly a gas, are dispersed throughout a second fluid species. Foams appear widely in nature, such as in sea foam produced by breaking waves in the ocean [76], [77] and in nests produced by a diverse range of animals used to protect their eggs [78]–[80], as well as having a large number of industrial applications, such as in firefighting [81], [82] and in mineral floatation [83], [84]. Hence, the study of foams is a very active area of research, e.g. [76], [77], [85], [86].

Foams are classified by their liquid volume fraction  $\phi_f$ , the ratio of gas to fluid per unit volume. Dry foams occur when  $\phi_f \approx 1\%$ . Here, bubbles deform into polyhedra, where most of the liquid is confined in thin films at the bubble edges which form quasi-flat planes known as Plateau borders [85]. Above some critical volume fraction ( $\phi_f \approx 25 - 35\%$ ) bubbles separate into discrete spherical units which move independently from each other. These types of foams are classified as wet foams or bubbly liquids.

Many experiments have been carried out on dry foams due to their ease of creation and stability [87], but far fewer experimental studies have been carried out on wet foams. This is due to the fact that wet foams quickly become unstable and break down due to drainage of the liquid caused by gravity. Recent studies on wet foams in microgravity have shown that inhibiting fluid drainage dramatically increases their stability [88]–[91].

Current methods of creating wet foams in microgravity only allow for the creation of polydisperse foams, foams where the constituent bubbles have a variety of sizes. In this chapter, we present a new method of creating monodisperse wet foams formed of clusters of bubbles. Our new method uses diamagnetic levitation to suspend bubble clusters in a weightless environment for an indefinite period of time, providing a novel way of studying monodisperse wet foams terrestrially. Also, we show we can manipulate the arrangement of these bubble clusters in a contactless manner, by adjusting the current in the superconducting solenoid magnet used to

levitate the bubble clusters. We note that foams have previously been studied in microgravity using diamagnetic levitation [91]. Although in these experiments only the surrounding fluid is levitated in a weightless environment, hence bubbles throughout the foam are still subjected to buoyancy forces.

## 5.1 Experimental set-up

We used the Cryogenic superconducting magnet, set-up as discussed previously in chapter 3, where the tank fitted in the bore of the magnet was filled with an  $0.11 \text{ mol L}^{-1}$  aqueous solution of manganese chloride.

To create bubbles a measured volume of air was injected into the levitation point using an air-filled syringe attached to an L-shaped tube. Following the creation of the initial bubble, subsequent bubbles were injected into the levitation point at a rate of one bubble every 2–5 seconds. It was found that the liquid layer at the point of contact between bubbles ruptured after  $\sim 3\text{--}4$  seconds, initiating the process of coalescence. In order to inhibit bubble coalescence the manganese chloride solution was mixed with a small addition of the surfactant sodium dodecyl sulfate (SDS). The surfactant decreased the surface tension at the liquid-air interface from  $72 \text{ mN m}^{-1}$  to  $\sim 30 \text{ mN m}^{-1}$ , but also increased the foam stability. This allowed bubbles to levitate indefinitely without coalescing [88], [89].

## 5.2 Results

The first row of figure 5.1 shows a series of images showing different configurations of the same seven  $3.1 \pm 0.1 \text{ mm}$  diameter bubbles levitating in differently shaped magnetogravitational potential traps. Images were taken from an angle looking down the axis of the magnet bore. The shapes of magnetogravitational traps were varied by altering the current in the magnet solenoid coils,  $I$ . A convenient alternative measure of this current is the magnetic field strength at the geometric centre of the solenoid,  $B_0 \propto I$ . The second row of figure 5.1 shows the contours of a vertical cross-section of the magnetogravitational potential for the corresponding value of  $B_0$ . The circles on the images display a representation of the bubbles.

In the experiment displayed in figure 5.1, seven bubbles were injected into the levitation point, where  $B_0$  was initially set to 13.2 T, and then increased slowly to 14.5 T. Three different arrangements of the bubble cluster were found: (i) a close-packing arrangement, where the bubbles lie on two separate planes consisting of 3 and 4 bubbles respectively in a close-packing arrangement; (ii) a pentagonal arrangement, where 5 bubbles lie on a horizontal plane equally spaced from each other and the remaining 2 bubbles lie on the solenoid axis equally spaced above and below the central point of the pentagon; (iii) a planar arrangement, where the bubbles formed a hexagonal lattice arranged on a single plane.

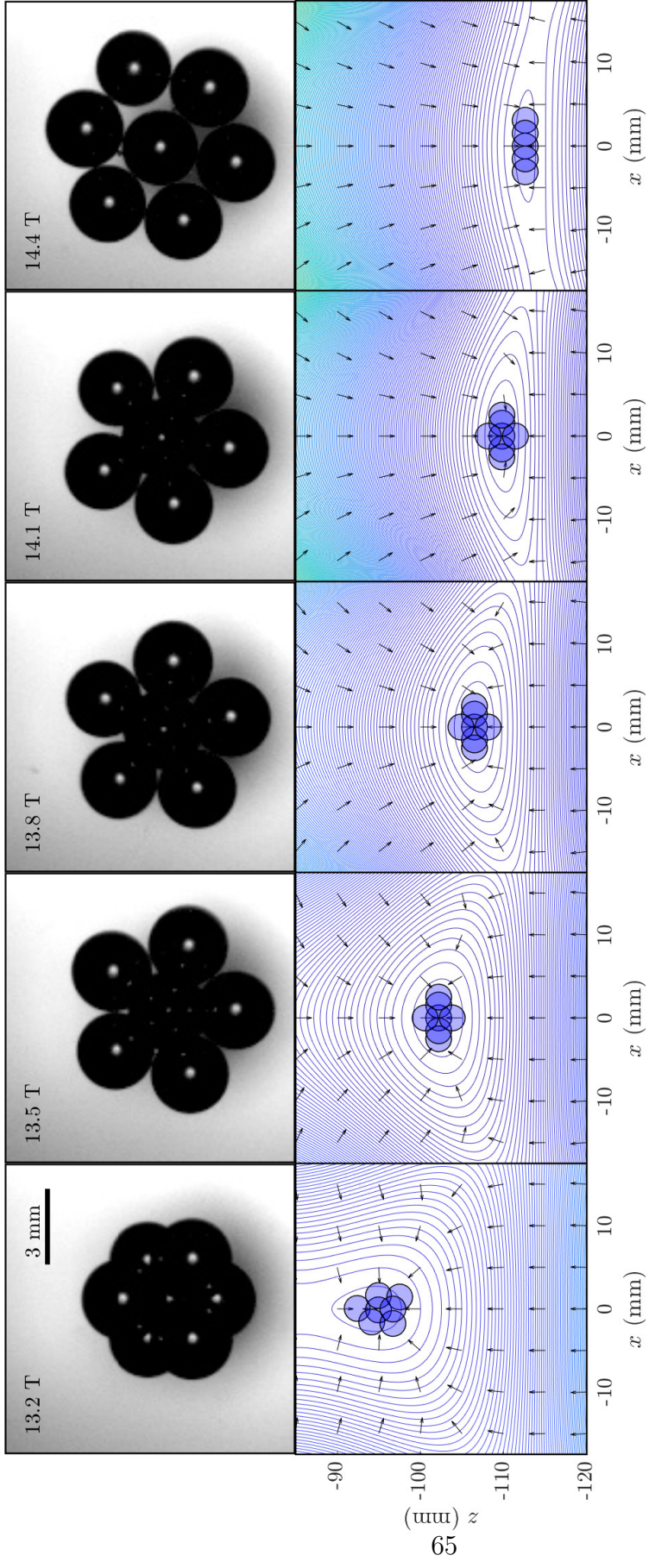


Figure 5.1: A bubble cluster of 7 equal sized bubbles at various values of  $B_0$ . Top row) images of the bubble cluster as viewed from above the magnet bore. Bottom row) a vertical cross section of the contours of the magnetogravitational potential for the corresponding value of  $B_0$ . Circles give a representation of the bubbles as if viewed parallel to the axis of the magnet, where  $x = z = 0$  is the geometric center of the solenoid. Three arrangements of the bubble cluster can be seen from the images: (i) a close-packing arrangement ( $B_0 = 13.2$  T); (ii) a pentagonal arrangement ( $B_0 = 13.5$ – $14.1$  T); (iii) a planar arrangement ( $B_0 = 14.4$  T).

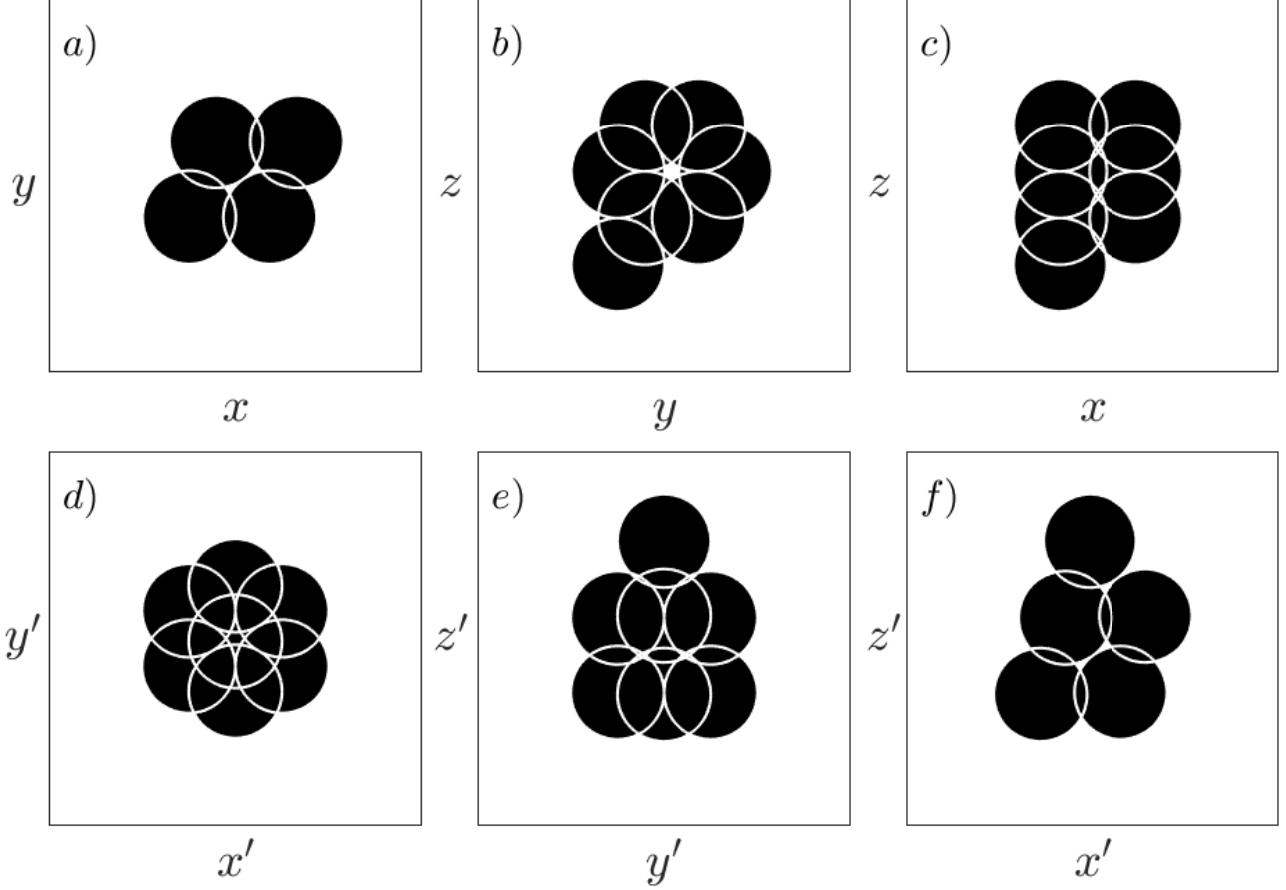


Figure 5.2: 2D projection of seven close packing bubbles. a)-c) show the same 2D projections viewed along three perpendicular axes. d)-f) show the same arrangement of bubbles as in a)-c) except the axes have undergone the coordinate transformation given in equation (5.1).

We can't provide definitive proof that what we refer to as the close-packing arrangement is in actuality a close-packing arrangement. We compared the first experimental image in figure 5.1 to a large number of 2-dimensional projections of bubble clusters constructed of seven bubbles. Figure 5.2 displays a number of these projections. Figure 5.2a-c shows a 2D projection of the same close packing arrangement of 7 bubbles viewed along 3 different axes. In this projection, the two planes the bubbles lie on are parallel to the  $y - z$  plane, these two planes are easily observed in figure 5.2c. Figure 5.2d-f show the same arrangement of bubbles just with the coordinate system rotated about the coordinate axes. The relationship between the two coordinate systems is

$$\begin{pmatrix} x' \\ y' \\ z' \end{pmatrix} = R_z(20^\circ)R_y(340^\circ)R_x(210^\circ) \begin{pmatrix} x \\ y \\ z \end{pmatrix}, \quad (5.1)$$

where the rotation matrices are

$$\begin{aligned}
 R_x(\theta) &= \begin{pmatrix} 1 & 0 & 0 \\ 0 & \cos \theta & -\sin \theta \\ 0 & \sin \theta & \cos \theta \end{pmatrix}, \\
 R_y(\theta) &= \begin{pmatrix} \cos \theta & 0 & \sin \theta \\ 0 & 1 & 0 \\ -\sin \theta & 0 & \cos \theta \end{pmatrix}, \\
 R_z(\theta) &= \begin{pmatrix} \cos \theta & -\sin \theta & 0 \\ \sin \theta & \cos \theta & 0 \\ 0 & 0 & 1 \end{pmatrix}.
 \end{aligned} \tag{5.2}$$

By comparing the top-down view of the close packing arrangement in figure 5.1 and the 2D projection in 5.2d excellent agreement can be found, providing us with confidence that what is observed in experiment is a close packing arrangement.

The bubble cluster transitioned from the close-packing arrangement to the pentagonal arrangement as  $B_0$  was increased from 13.2–13.3 T. In the transition the bubbles rotated as a rigid body about a central point and then rearranged themselves into the pentagonal arrangement. The bubble cluster then transitioned from the pentagonal arrangement to the planar arrangement as  $B_0$  was increased from 14.3–14.4 T. As  $B_0$  was increased from 13.3–14.3 T the vertical distance between the central bubbles decreased leading to a small gap forming between two of the bubbles on the horizontal plane (see figure 5.1), then as  $B_0$  was increased from 14.3–14.4 T the upper central bubble moved vertically down displacing the lower central bubble which then moved into the aforementioned gap. This differs from the transition from the close-packing to the pentagonal arrangement as no rigid body rotation of the bubble cluster was observed.

As  $B_0$  was increased the vertical location of the centre of mass of the bubble cluster decreased as the position of the minima of the magnetogravitational trapped decreased. Stable magnetogravitational traps only exist for air bubbles using the specified manganese chloride solution in our magnet for  $B_0$  in the range 13.2–14.5 T. Outside of this range it is not possible to inject bubbles into the system without them either floating upwards due to buoyancy or being displaced and trapped against the wall of the tank. For bubble clusters stably levitating in the magnetogravitational trap, as  $B_0$  transitioned out of this stable regime bubbles were observed to float upwards due to buoyancy.

Figure 5.3 shows a montage of images of a second bubble cluster. Here, nineteen 3.0–3.4 mm diameter bubbles were injected into the magnetogravitational trap when  $B_0$  was set to 14.5 T, initially forming a planar arrangement of bubbles. This planar bubble arrangement remained stable for  $B_0$  in the range 14.1–14.5 T but changed arrangement for  $B_0 < 14.1$  T. As stated previously, the trap is only able to stably

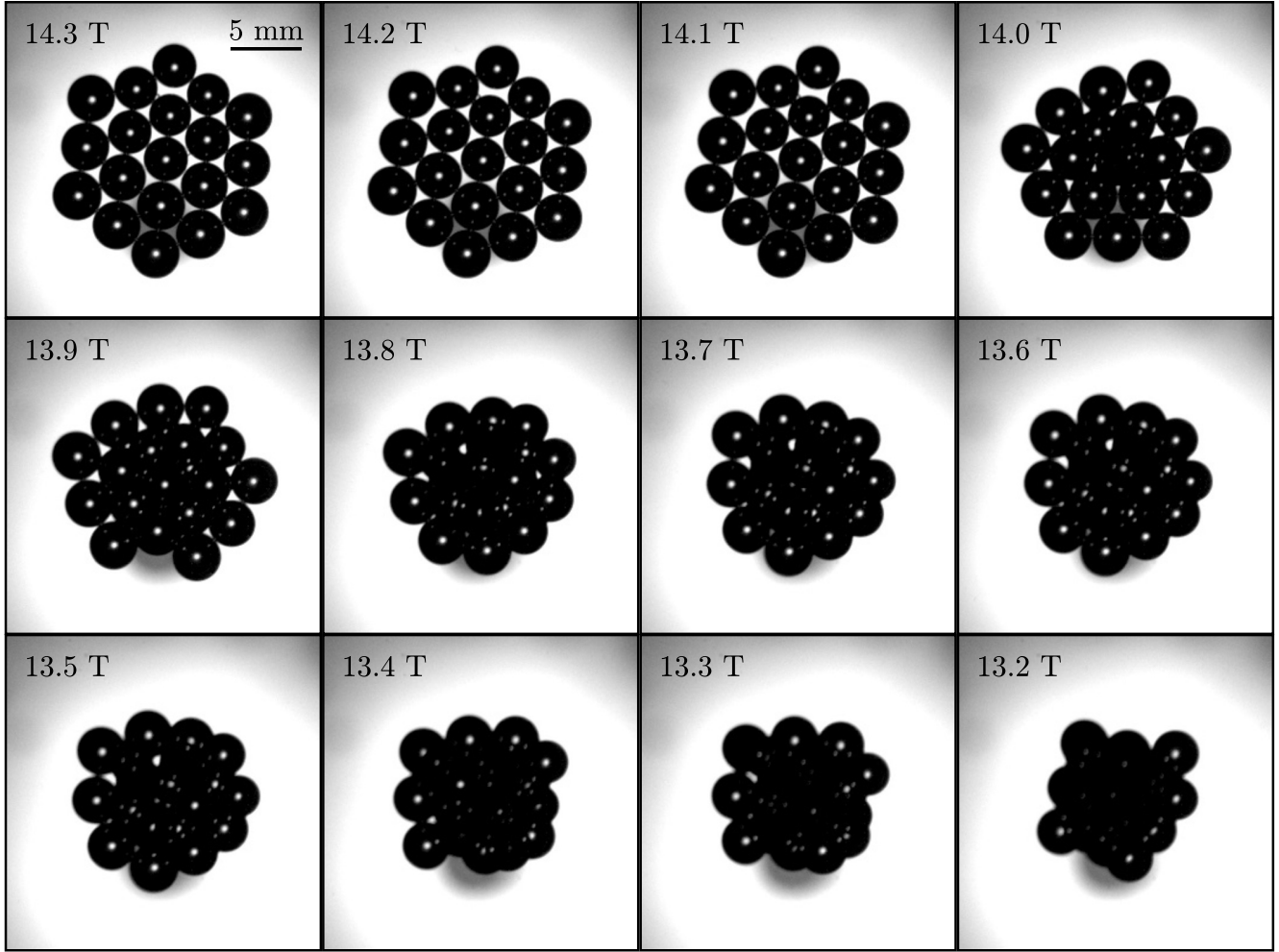


Figure 5.3: A bubble cluster of 19 similarly sized bubbles. In this experiment,  $B_0$  was decreased from 14.5 to 13.2 T. A planar arrangement was observed for  $B_0$  in the range 14.5–14.1 T.

trap bubbles for  $B_0$  in the range 13.2–14.5 T, hence no bubble clusters could be created outside this range. Due to the number of bubbles in this cluster and the limitations of our imaging set-up it is not possible to identify the arrangements the bubbles formed for  $B_0 < 14.1$  T. However, we were able to observe that the horizontal area of the cluster, as viewed from above, decreased as  $B_0$  decreased, implying that the vertical height of cluster increased. This is expected, as the shape of the magnetogravitational trap may be approximated by a thin oblate spheroid at  $B_0 = 14.5$  T which leads to the formation of planar bubble structures, but as  $B_0$  is decreased the trap is ‘squashed’ horizontally inwards, hence the horizontal span of the trap decreases and the height of the trap elongates leading to the shape of the trap transitioning into that of a tear drop at  $B_0 = 13.2$  T (see figure 5.1 second row).

### 5.3 Uses for bubble clusters

At the start of this chapter, we discussed the use of bubble clusters to study three-dimensional monodisperse wet foams. Here, we speculate on some other uses for three-dimensional bubble clusters.

Ilievski *et al.* [92] have previously used diamagnetic levitation to study templated self-assembly of levitated plastic spheres in a manganese chloride solution. In their study, a similar technique was used to diamagnetically levitate plastic spheres, but templates were inserted to control the structure of the levitated spheres. It was found that inserting these templates could force the plastic spheres into close packed crystalline formations. We propose that a similar idea could be used in the case of bubble clusters. Adding a template, such as a tube aligned with the central axis of the solenoid, could force bubble clusters to form close packed crystalline structures. In the study of Ilievski *et al.* [92], agitation was required to manipulate the plastic spheres once positioned within the magnetic field; this is due to the friction between the objects, but this is not an issue with bubbles: due to the thin fluid layer between bubbles they behave as frictionless spheres. Therefore, if a number of spherical bubbles are diamagnetically levitated but confined within a template, we hypothesise that to minimise the energy of the total system they would self-assemble into close-packed planes.

One use for crystalline bubble clusters could be the production of new acoustic metamaterials. Such materials have interesting acoustic properties as their density and bulk modulus, which control the speed of acoustic waves, vary throughout the material leading to the effective density and bulk modulus of such materials to be highly frequency dependent.[93] Due to this variation of physical characteristics throughout the material acoustic metamaterials can also inherit counterintuitive and novel physical properties such as a negative effective density and negative effective bulk modulus. Previously, acoustic metamaterials have been fabricated from cubic crystal lattices of rubber-coated lead spheres embedded in epoxy.[94] We can fabricate a similar arrangement of a lattice of spheres of different density and bulk modulus embedded in a second solution, except that in our case the density of the spheres is several orders of magnitude lower than that of the surrounding material. Crystalline bubble clusters created in a fluid using diamagnetic levitation, then could be solidified, for example if the fluid is a UV-curable polymer solution. The same methodology can be used to create a single plane of ordered, low-density spheres in a higher-density material by using planar bubble lattices. We also have the ability to control the volume of bubbles, hence materials consisting of a combination of bubble sizes or materials, where the size of cavities varies throughout the material, could be constructed. Such materials may pave the way for advancements in acoustic cloaking for example [95].

An additional use of bubble clusters could be to study the collective oscillations of clusters of bubbles. The scattering of acoustic waves due to the nonlinear interactions of clusters of bubbles plays an important role in ultrasonic imaging, ultrasonic

detection and ultrasonic medical therapy [96]–[98]. Due to the importance of this, a large number of both experimental and theoretical studies have been carried out on the oscillations of bubble clusters [99]–[102]. The advantage of using diamagnetic levitation to study this phenomenon is that it allows for control of the size of the radii and the number of bubbles. This would allow for the validation of theoretical models by comparing predictions to the simplest cases of the interaction of just a handful of bubbles. Preliminary experiments we have carried out to study the collapse of diamagnetically levitated air bubbles using pressure waves have shown with a simple modification to our current experimental setup we are able to vary the pressure inside the fluid-filled tank. Hence, the experimental setup required for such a set of experiments could easily be designed and manufactured.

## 5.4 Summary

In this chapter, we presented a method to create monodisperse bubble clusters using diamagnetic levitation to stably trap bubble clusters in a surrounding fluid. The arrangement of these bubble clusters was manipulated in a contactless manner by adjusting the solenoid current, and hence the central magnetic field strength produced by the superconducting solenoid. It was found that bubble clusters conformed to the magnetogravitational potential trap used to levitate them. A variety of configurations of bubble clusters was observed, from planar arrangements to close-packing arrangements.

We observed clusters of up to 19 bubbles, but in theory clusters of hundreds if not thousands of bubbles could be generated and manipulated in a similar fashion. Here, we have focused on studying monodisperse bubble clusters, but polydisperse bubble clusters could in principle be produced just as easily. As well as generic polydisperse clusters, it is possible to create polydisperse clusters where the size of every bubble is controlled, e.g. a bubble cluster consisting of bubbles of a set number of predetermined sizes. As explained in chapter 3, by adjusting the location of the end of the L-shaped tube within the bore of the magnet it is possible to control the size of bubbles produced.

At the end of this chapter, we have speculated on a number of potential future use cases for bubble clusters. Further experiments and research is needed to realise these ideas but it is evident that diamagnetically levitated bubble clusters provide a new experimental tool to study a wide variety of bubble phenomena.

## Chapter 6

# Sonomaglev: combining acoustic and diamagnetic levitation

The motivation behind the work carried out in this chapter was to develop a new experimental technique to manipulate multiple simultaneously diamagnetically levitated objects. The options to manipulate multiple objects magnetically are limited. Diamagnetic levitation allows for the levitation of multiple spatially-separated objects simultaneously if the objects have unique ratios of magnetic susceptibility to density [31]. The creation of multiple traps for a single material is also possible using diamagnetic levitation, by manipulating the shape of the strong magnetic field [103], but both these methods are very limited in the range of motion and number of objects they may manipulate. In contrast, the levitation and manipulation of multiple objects using acoustic levitation is much less technically challenging and correspondingly less restrictive. It has been shown by many authors that acoustic levitation can be used to manipulate levitated objects in a non-contact manner [104]–[106], and has also proven to be a powerful technique to carry out contactless manipulation experiments in a variety of disciplines, including: analytical chemistry [107]–[112], material sciences [113], pharmacy [114], [115] and micro-assembly [116]–[119]. Still, acoustic levitation has its drawbacks. Acoustically levitated objects tend to rotate and oscillate due to the high frequency acoustic radiation forces required to balance objects against the force of gravity. For certain applications this can be advantageous [111], but in most cases *stable* levitation of the objects under consideration is preferable.

In this chapter, and in Hunter-Brown *et al.* [120], we discuss the development of a new experimental technique ‘Sonomaglev’. By combining techniques from both acoustic and diamagnetic levitation we are able to manipulate the position of spherical liquid droplets, drawing on the strengths of each method. The force of gravity is compensated throughout the droplets by applying a vertical diamagnetic body force using a superconducting magnet, providing a simulation of weightlessness. Then, comparatively weak acoustic radiation forces are used to position the droplets. We show that multiple droplets, arranged horizontally along a line, can be stably levitated with this system and demonstrate controlled contactless coalescence of two

droplets. We further show that it is possible to reproduce the locations of the levitated droplets through simulation.

## 6.1 Acoustic levitation

Acoustic levitation utilises high frequency sound waves to exert acoustic radiation forces on objects to suspend them against the force of gravity [2]. The technique was first demonstrated in 1933 by Bücks and Müller, who reported on the levitation of ethanol droplets at the nodes of a standing wave generated between an oscillating quartz crystal and a reflector [121]. Up until recently, most common acoustic levitation set-ups consisted of a Langevin horn, a stack comprised of a piezoelectric transducer coupled to a horn shaped radiative element, placed opposite either a matching device or a reflector plate [106]. These set-ups normally operate at frequencies of between 20–100 kHz, creating a standing acoustic wave along a vertical axis, at the nodes of which objects may be levitated. In principal, the construction of such experimental set-ups is based entirely on the design of the first acoustic levitator constructed by Bücks and Müller. Over the last decade, it has been shown that intricate, readily tuneable sound fields can be constructed by using an array of small ultrasonic transducers [104], [122], allowing for the manipulation of multiple objects in three dimensions. The discovery that an array of ultrasonic transducers can create customisable acoustic levitation systems has led to a resurgence in the study of non-contact manipulation using acoustic levitation techniques [106], [123]–[125].

Although acoustic levitation has many advantages, such as its ability levitate objects of almost any material [2], the method also has some drawbacks. From the earliest experiments, acoustically-levitated objects were observed to have a tendency to oscillate, attributed to the response of the acoustic field to the presence of the object [126], [127]. Objects may also start to rotate spontaneously due to streaming flows in the surrounding gas generated by the high pressure sound waves [128], [129], though techniques to mitigate these effects and control the rotation have been demonstrated recently [130], [131]. These same streaming flows may also be problematic in studies of liquid droplets, where the air flow affects heat and mass transfer non-uniformly at the droplet’s surface [132] and also sets up flows within the droplet [133]. Acoustically-levitated liquid droplets are often deformed into oblate-like shapes [1], [134]; this typically occurs when the diameter of the droplet is of the same order as the acoustic wavelength. These characteristics, which are usually undesirable (though occasionally exploited [134]), are avoided in similar experiments using diamagnetic levitation [13], [14], [16], [17].

## 6.2 Experimental set-up

We used the Cryogenic superconducting magnet, as detailed in chapter 2.4, to levitate water droplets diamagnetically in air at room temperature and atmospheric pressure.

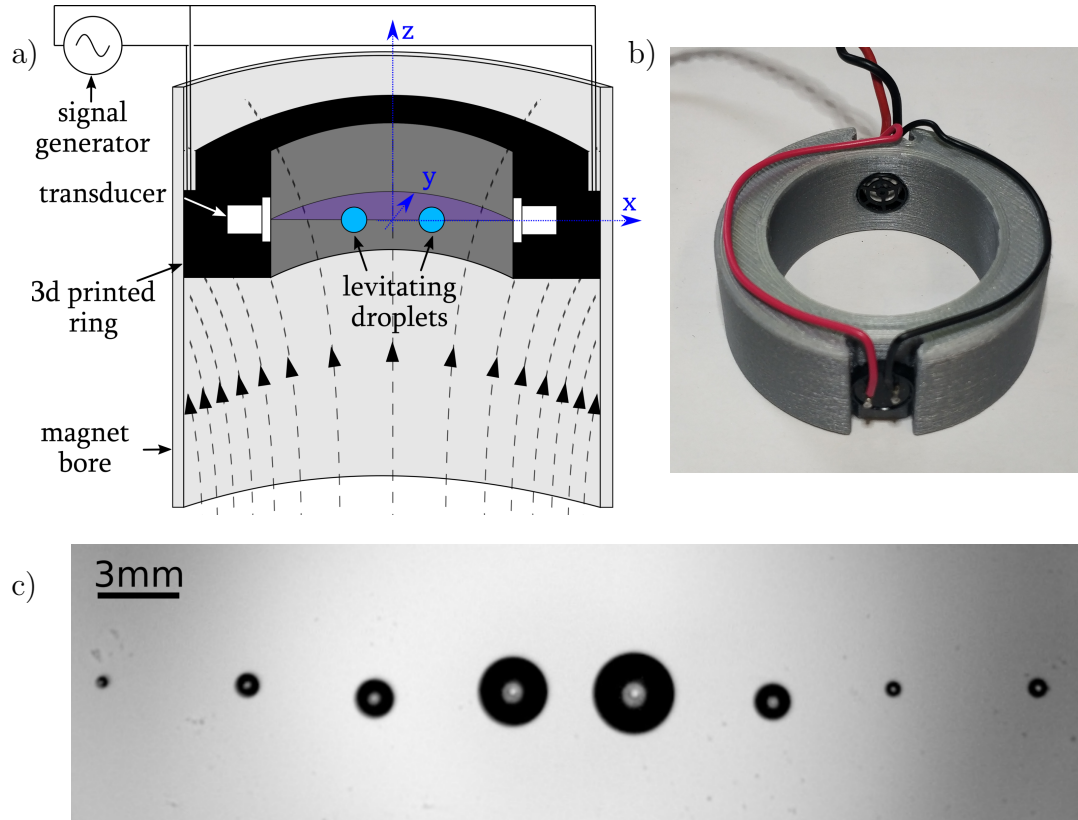


Figure 6.1: a) Diagram of the experimental set-up inside the superconducting magnet bore. The two ultrasonic transducers are aligned along an axis,  $x$ , perpendicular to the vertical bore axis,  $z$ . Dashed lines represent the magnetic field lines. b) Image showing the 3d-printed PLA ring used to mount the transducers in the magnet bore. c) Line of eight droplets of diameters 0.4–3.0 mm (30 nL–14  $\mu$ L) levitating in the bore of the magnet, with position controlled by the acoustic-transducers.

For all experiments discussed in this chapter the magnetic field strength at the centre of the solenoid was set to  $B_0 = 17.4$  T, leading droplets to levitate approximately 11 cm above the centre of the solenoid. This resulted in a value of  $\kappa = -0.903$  (see chapter 2.5) for  $\rho_1 = 998.2 \text{ kg m}^{-3}$ ,  $\rho_2 = 1.2 \text{ kg m}^{-3}$ ,  $\chi_1 = -9.03 \times 10^{-6}$  and  $\chi_2 = 4.0 \times 10^{-7}$  [42], [135]–[137],  $\rho_1$  and  $\chi_1$  being the density and volume magnetic susceptibility of water and  $\rho_2$  and  $\chi_2$  being the density and volume magnetic susceptibility of air.

The bore was fitted with a custom, 3d-printed polylactic acid (PLA) ring of outer diameter 57 mm, inner diameter 39 mm and height 20 mm (see figure 6.1a,b). This ring contained two 10 mm diameter ultrasonic transducers (CamdenBoss CTD40K1007T), positioned diametrically opposite each other and aligned along a horizontal axis such that their faces were perpendicular to the edge of the ring, as shown in figure 6.1a,b. The transducers were wired in parallel, driven in-phase, and connected to a function generator (Stanford Research DS345), which was used to drive the transducers with

frequencies of 37–40 kHz and up to a maximum peak-to-peak voltage,  $V_{pp}$ , of 20 V. The ring was fitted in the bore of the magnet such that the central horizontal plane of the ring intersected with the stable equilibrium levitation position of a diamagnetically levitated water droplet. Despite containing some ferromagnetic material, the operation of the transducers was not affected by the presence of the strong magnetic field produced by the superconducting magnet. Images were taken using a camera and the optical set-up arranged as described in chapter 3.2.

In experiments an atomiser was used to spray a fine mist of distilled water above the magnet, which then descended into the magnet bore. From preliminary experiments, it was found that the friction between the fluid and the atomiser nozzle led to a small amount of charge build up on droplets. For most experiments we required the droplets to be uncharged, as we could not account for additional electrostatic forces between droplets, but for a small subset of our experiments we took advantage of this charging phenomena (see section 6.8.2). To make sure no charge leaked onto atomised droplets we used an atomiser with a tank, neck and nozzle constructed from brass. The atomiser was then grounded for all experiments we wished to produce uncharged droplets.

To test that this set-up produced uncharged droplets, we carried out a small number of experiments where we sprayed the atomiser above the magnet bore in the absence of the PLA ring and ultrasonic transducers, with the atomiser both grounded and ungrounded. In experiments where the atomiser was ungrounded, the mist would coalesce into several well separated droplets, each repelling each other due to the electrostatic charge build up on each of the individual droplets. In experiments when the atomiser was grounded, the mist coalesced into a single larger droplet, providing clear evidence that this method is able to produce uncharged atomised droplets.

With the acoustic transducers switched off, the mist of droplets coalesced as one larger droplet at the stable levitation point, as described above. When a voltage was applied to the transducers and the experiment repeated, the mist coalesced into several well-separated droplets, each levitating in stable equilibrium. Figure 6.1c is a photograph, taken from an angle looking down the axis of the magnet bore, showing the formation of eight separate droplets from the mist. The droplets in this experiment have diameters in the range 0.4–3.0 mm (volume 30 nL–14  $\mu$ L), and are separated by approximately 5 mm. The two centre droplets lie approximately 2 mm from the axis of the bore. This image is representative of all experiments we performed using this method: while the sizes of the individual droplets show some variation between repeat experiments, the position and spacing between the droplets is constant for a given frequency and voltage. The technique usually produced droplets that were larger closer to the axis, since the diamagnetic force funnelled the mist toward the axis as it descended, though in principle droplets with uniform size could be levitated.

### 6.3 Levitation points of droplets

To calculate the levitation position of droplets requires knowing all the forces acting on the droplets. The magnetic and gravitational forces acting on a droplet can be calculated from the gradient of the magnetogravitational potential  $u_{mg}$ , as described in chapter 2. The acoustic radiation force acting on a droplet may be calculated from the gradient of the Gor'kov potential [138],

$$u_{acoust} = \frac{3V}{2} \left[ f_1 \frac{\langle p^2 \rangle}{3\rho_2 c_2^2} - f_2 \frac{\rho_2 \langle u^2 \rangle}{2} \right],$$

$$f_1 = 1 - \frac{\rho_2 c_2^2}{\rho_1 c_1^2},$$

$$f_2 = \frac{2(\rho_1 - \rho_2)}{2\rho_1 + \rho_2}.$$
(6.1)

Here,  $c_1$  is the speed of sound in water and  $c_2$  is the speed of sound in air at room temperature and pressure, and  $\langle p^2 \rangle$  and  $\langle u^2 \rangle$  are the mean square amplitudes of the pressure and velocity of air, respectively. For our case of water in air  $f_1 \approx f_2 \approx 1$ .

The Gor'kov potential is only valid in the limit that the maximum radial extent of the object considered is less than the wavelength of the acoustic field it is placed in. In experiment, the transducers are driven at frequencies from 37–40 kHz, hence produce sound waves with an acoustic wavelength of 8.65–9.35 mm, which is significantly greater than the maximum radius of water droplets studied  $R_{max} \sim 3.0$  mm. Therefore, this approximation is valid for the case being studied.

To find levitation points requires finding locations within the magnet bore at which the net force on a droplet is zero. These points must also satisfy the condition that if the droplet is perturbed away from such a location in any direction, the droplet experiences a restoring force directly opposing this motion. Due to the fact that all forces acting on a droplet may be expressed as the gradient of a potential, we may express the net force on a droplet as the gradient of some total potential

$$u_{total} = u_{mg} + u_{acoust}.$$
(6.2)

At locations of local minima in  $u_{total}$  droplets experience zero net force and all restoring forces act in a direction towards the local minima. Hence, levitation points may be found by finding the locations of local minima of the total potential within the magnet bore.

Due to fact that both  $u_{mg}$  and  $u_{acoust}$  are proportional to the volume of droplets  $V$  (see equation (2.12) and (6.1)), it follows that  $u_{total}$  must also be proportional to  $V$ . We define the total, magnetogravitational and acoustic potential energy densities to be

$$U_{total} = u_{total}/V, \quad U_{mg} = u_{mg}/V, \quad U_{acoust} = u_{acoust}/V.$$
(6.3)

Since all potential energy densities considered here are directly proportional to the volume of droplets, local minima that exist in the potential energy must also exist

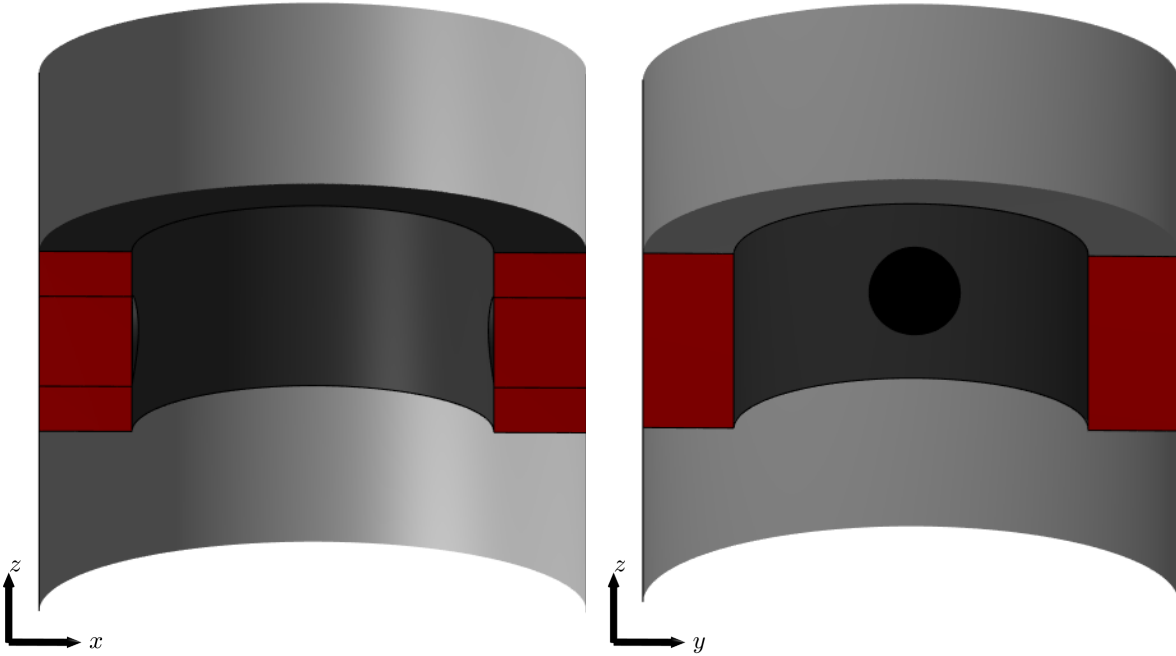


Figure 6.2: Half sections of the experimental domain. The 3D renders have been split down the  $y = 0$  and  $x = 0$  planes respectively. The black regions denote the surface of the transducers, the dark grey regions denote the surfaces of the PLA ring and the light grey regions denote the surface of the superconducting magnet bore. The red surfaces are to denote the internal cross-section of the PLA ring and transducers.

in potential energy density. From now on we shall work with the potential energy densities for ease of calculation.

## 6.4 Modelling ultrasonic transducers

To calculate the Gor'kov potential it is necessary to know the pressure field and velocity field of the external fluid. For ultrasonic transducers a variety of methods to approximate these fields exist, the most relevant of which shall be discussed in the following section. Although to begin with, we shall give a brief overview of the generalised equation and domain which we are using to calculate these fields.

### 6.4.1 Mathematical model

We model the air in the magnet bore using the compressible Euler equations. For small perturbations to the background pressure field, as in our system, the compressible Euler equations may be reduced to the linear acoustic wave equation (see Landau and Lifshitz [139] chapter 8).

To give a better view of the internal geometry of the domain figure 6.2 shows two half sections of the domain, one where the domain has been split along the  $y = 0$  plane and the other where the geometry has been split along the  $x = 0$  plane. Here, the black regions are the transducer faces, the dark grey regions are the surface of the 3D-printed PLA ring and the light grey regions are the bore of the superconducting magnet.

In our experimental setup, we set the transducer faces to oscillate in phase at a given frequency to generate sound waves. The appropriate boundary condition here is that the velocity of the fluid normal to the transducer face is equal to the velocity of the transducer face. Due to the materials which the magnet bore and PLA ring are constructed from it is reasonable to assume that these surfaces reflect sound waves generated by the transducers. Hence, it is appropriate to enforce acoustic boundary conditions on these surfaces [140], [141]. A more in-depth discussion of acoustic boundary conditions shall be given in section 6.4.4.

In addition to these surfaces, the domain extends both vertically up and down. No surfaces or objects block the fluid in either direction and therefore inhibit the flow of the fluid. When modelling these regions we treat them as open boundaries.

## 6.4.2 Rayleigh-Sommerfeld model

Traditionally ultrasonic transducers have been modelled using the piston source model. In this case, the transducer is modelled as a rigid piston embedded in free space, where the face of the transducer oscillates at an angular frequency  $\omega$ , see figure 6.3. The pressure field produced in a fluid by such a system may be calculated by evaluating the Raleigh-Sommerfeld integral [142]

$$p(\mathbf{x}, \omega) = \frac{-i\omega\rho}{2\pi} \int_S v(\mathbf{x}_s) \frac{e^{ikR}}{R} dS(\mathbf{x}_s), \quad (6.4)$$

where  $v$  is the velocity of the surface of the transducer,  $R$  is the distance between the point  $\mathbf{x}$  and the source point  $\mathbf{x}_s$  on the surface of the transducer,  $\rho$  is the density of the fluid and  $k$  is the wavenumber related to  $\omega$  by  $\omega = ck$ , where  $c$  is the speed of sound in the fluid. A further simplification can be made assuming that velocity  $v$  is constant over the surface of the transducer,

$$p(\mathbf{x}, \omega) = \frac{-i\omega\rho v}{2\pi} \int_S \frac{e^{ikR}}{R} dS(\mathbf{x}_s). \quad (6.5)$$

Since most transducers are circular (including ours), the Rayleigh-Sommerfeld integral for a circular piston of radius  $a$  given in terms of cylindrical polar coordinates  $(\varrho, \varphi, z)$  is

$$p(\mathbf{x}, \omega) = \frac{-i\omega\rho v}{2\pi} \int_0^{2\pi} \int_0^a \frac{e^{ikR}}{R} \varrho_s d\varrho_s d\theta_s, \quad (6.6)$$

$$R = \sqrt{\varrho^2 + \varrho_s^2 - 2\varrho\varrho_s \cos\theta_s + z^2},$$

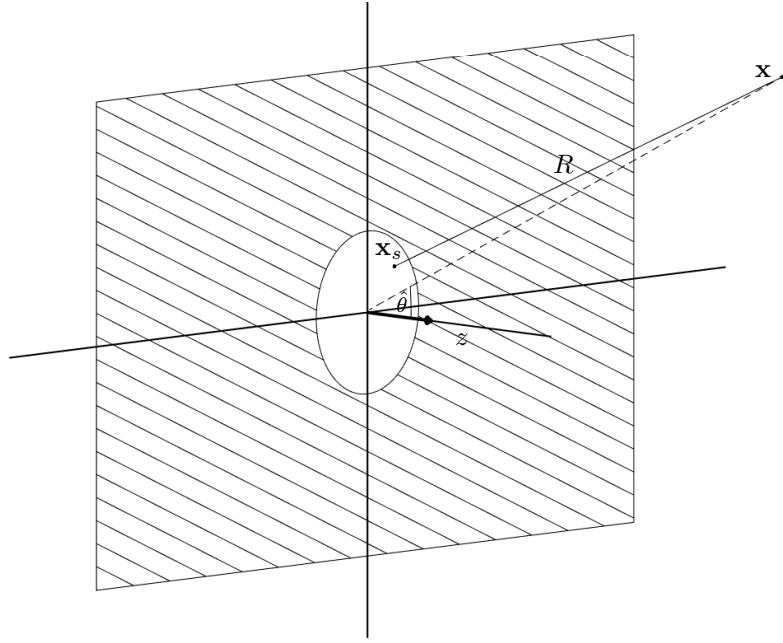


Figure 6.3: Circular planar piston situated in a plane denoted by the hashed region. The fluid is located in the region  $z \geq 0$ , where here  $z$  is the coordinate axis perpendicular to the face of the piston. The velocity of the fluid in contact with the surface of the piston is  $v$  in the direction normal to the piston.

where coordinates with subscript  $s$  denote a point located on the piston's surface. Solutions along the central axis ( $\varrho = 0$  &  $R = \sqrt{\varrho^2 + z^2}$ ) are the most straightforward to find analytically:

$$p(z, \omega) = \rho c v \left( e^{ikz} - e^{ik\sqrt{a^2+z^2}} \right). \quad (6.7)$$

Asymptotic solutions can be obtained in the far field limit in which  $R \gg a$ :

$$p(\mathbf{x}, \omega) = -i\omega\rho v a^2 \frac{e^{ik|\mathbf{x}|}}{|\mathbf{x}|} \frac{J_1(ka \sin \hat{\theta})}{ka \sin \hat{\theta}}, \quad (6.8)$$

where  $\hat{\theta}$  is the angle created between the central axis of the transducer and the line connecting the origin and the point  $\mathbf{x}$  and  $J_1(x)$  is a first-order Bessel function of the first kind.

### 6.4.3 Matrix method for reflections

For most applications where the pressure field of an array of small ultrasonic transducers needs to be determined, equation (6.8) is used [118], [119], [124], [143]. In this case, the pressure field is calculated by summing the contributions of the pressure

field for each transducer. This process is computationally very quick, due to the fact a single analytical equation is being used to define the pressure field produced by each transducer. The downside to this method is it fails to account for reflections created by sound waves reflecting off nearby objects/surfaces.

In many cases reflected sound waves can significantly change the pressure field and ignoring them therefore leads to significant errors. To account for this, a technique called the matrix method was developed that accounts for reflections by calculating the pressure field on a given surface [144], [145]. By discretising the surface into surface elements, each surface element can be treated as a point source with strength proportional to both the pressure at its location and its area. A new pressure field can then be calculated at each point in the domain by summing over the pressure fields created by this set of point sources. By then evaluating this new pressure field at other surfaces that are present in the domain the process described above can be repeated. Repeating this process, reflecting the pressure field off alternating surfaces, creates a series of pressure fields which may be summed together to approximate the effect of reflections within the domain.

This technique is known to be very effective, but only if the objects/surfaces being considered do not form a single continuous loop or are spaced a suitable distance away from each other (see figure 6.4), such that there is an air gap between surfaces [145]. This is due to the fact that surfaces are discretised and then evaluated as point sources. So in the case where there are multiple separated surfaces, the pressure field produced by each surface element is allowed to decay as it propagates back towards the other surfaces in the domain. In the case where there is only a single continuous surface, reflections are evaluated on the same surface for each iteration of the series.

We now consider a surface that has been discretised such that the distance between the centre of each neighbouring element is several orders of magnitude less than the wavelength of the sound being produced,  $\lambda$ . Considering a small subset of adjacent elements on the surface, we can assume the pressure at the centre of each element is roughly equal, due to the fact that the pressure field is continuous and varies on scales comparable to  $\lambda$ . If we now consider evaluating the pressure on one of these surface elements just due to the contributions from its neighbours, we can see that the pressure is approximately proportional to its previous value multiplied by the number of neighbours, due to the fact that pressure sources radiating from each neighbour do not decay over such small length scales. Hence this configuration leads the pressure field to grow on the surface for each iteration, leading to an unbounded solution. This result can also occur if surfaces are placed too close together causing the matrix method to break down.

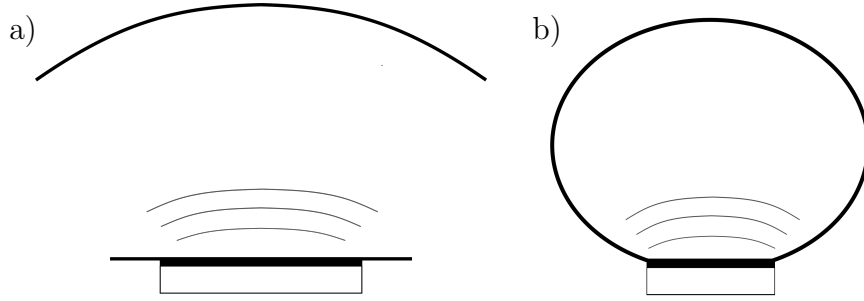


Figure 6.4: Examples of surfaces and domains for which a) the matrix method can model reflections and b) fails to model reflections.

#### 6.4.4 The linear acoustic equation

Another equivalent technique to model ultrasonic transducers is to solve the linear acoustic equation (the wave equation)

$$\nabla^2 p - \frac{1}{c^2} \frac{\partial^2 p}{\partial t^2} = 0, \quad (6.9)$$

where pressure is related to the velocity field  $\mathbf{u}$  by

$$\nabla p = -\rho \frac{\partial \mathbf{u}}{\partial t}. \quad (6.10)$$

As before, transducers are treated as simple rigid pistons oscillating at angular frequency  $\omega$ , therefore the time dependence of solutions can be assumed to be periodic, allowing for the reduction of equation (6.9) to the Helmholtz equation

$$\nabla^2 p + k^2 p = 0. \quad (6.11)$$

The equivalence of both methods presented here can be seen by realising that equation (6.4) is an integral of the Green's function of equation (6.11) over the surface of the transducer.

To solve equation (6.11) boundary conditions must be applied. On the surface of a transducer  $S$ , it is assumed that the surface is oscillating at velocity  $v$ , hence the fluid in the domain must be travelling at the same velocity as the surface of the transducer due to the kinematic condition. Therefore, the Neumann condition given below is enforced:

$$\hat{\mathbf{n}} \cdot \nabla p = -i\omega\rho v. \quad (6.12)$$

To all other boundaries, the acoustic boundary condition is applied, which is given in the form of a Robin boundary condition [140], [141]:

$$\hat{\mathbf{n}} \cdot \nabla p = -\frac{i\omega\rho}{Z_a} p, \quad (6.13)$$

here  $Z_a$  is the acoustic impedance between the fluid in the domain and the boundary. In the case that  $Z_a$  is large we find the zero Neumann boundary condition

$$\hat{\mathbf{n}} \cdot \nabla p = 0. \quad (6.14)$$

This condition is used in the case of hard walls, where it is assumed all incident pressure waves on the surface are reflected. It is also used in the case of symmetry planes. In the case where  $Z_a$  is small, we find the zero Dirichlet boundary condition

$$p = 0. \quad (6.15)$$

For open boundaries, this condition is required to be enforced infinitely far away from the sound source. This is an issue when solving this problem numerically, as most numerical methods (e.g. the finite element method, the finite difference method, the volume of fluid method) require finite spatial domains.

### 6.4.5 Perfectly matched layers

Several techniques have been developed to allow for the modelling of open boundary conditions when using finite spatial domains. These include absorbing boundary conditions [146], [147] and Dirichlet to Neumann maps [148], [149], but here we shall focus on the perfectly matched layer (PML) method [150]–[152]. In this method, additional absorbing layers are added to the outside of the domain of interest. In these layers, a coordinate transform is used to damp the amplitude of outgoing waves so that when they meet the outer boundary of the domain the amplitude of these outgoing waves is approximately zero, and hence a simple zero Dirichlet boundary condition or similar can be used. Properties must be carefully chosen to match the domain of interest to these absorbing layers otherwise a mismatch across this boundary may lead to spurious reflections. Here we shall first demonstrate this technique in 1 dimension, then demonstrate how it can be applied in 3 dimensions, with examples of PMLs of different forms, following closely the examples given in Deakin [152].

The Helmholtz equation in 1D is simply

$$\frac{d^2 u}{dz^2} + k^2 u = 0. \quad (6.16)$$

We shall enforce the boundary conditions  $u(0) = 1$  and  $u'(0) = ik$ , where in this case the prime denotes differentiation with respect to  $x$ . The solution here is

$$u(x) = e^{ikx}. \quad (6.17)$$

We are interested in  $u$  only at real coordinates, but the main principle of the PML method is that  $u$  is evaluated along a path through complex space. Hence, we apply a coordinate transform which maps the real coordinate  $x$  to a complex

coordinate  $\tilde{x}(x)$ . We shall now focus our attention on two distinct regions, the domain of interest,  $z \in [0, X]$  and the domain of the PML,  $x \in [X, X + \delta]$ . Here  $X$  is the width of the domain of interest and  $\delta$  is the width of the PML. We impose  $\tilde{x}(x) = x$  for  $x \in [0, X]$ , so that the solution to the Helmholtz equation in the domain of interest remains unchanged. If the Helmholtz equation is now expressed in terms of the transformed coordinate  $\tilde{x}(x)$ , it is found that

$$\begin{aligned} \frac{d^2 u}{d\tilde{x}^2} + k^2 u = \\ \frac{dx}{d\tilde{x}} \frac{d}{dx} \left( \frac{dx}{d\tilde{x}} \frac{du}{dx} \right) + k^2 u = 0, \end{aligned} \quad (6.18)$$

where the Jacobian of the transformation is

$$\gamma = \frac{d\tilde{x}}{dx}, \quad (6.19)$$

hence

$$\frac{1}{\gamma} \frac{d}{dx} \left( \frac{1}{\gamma} \frac{du}{dx} \right) + k^2 u = 0. \quad (6.20)$$

It is common notation to define transformations in terms of an absorbing function  $\sigma(x)$  [150]–[152], so that

$$\gamma(x) = 1 + \frac{i}{k} \sigma(x). \quad (6.21)$$

Absorbing functions are real, positive valued functions that equal zero in the domain of interest. The solution to equation (6.18) can now be written in terms of the original coordinate  $x$  as

$$u(x) = \begin{cases} e^{ikx} & x \in [0, X], \\ e^{ikx} e^{-\int_X^x \sigma(x') dx'} & x \in [X, X + \delta]. \end{cases} \quad (6.22)$$

Here it can be seen that by analytically continuing  $x$  into the complex plane for  $x > X$  we have managed to retain our solution in the domain of interest but the solution now exponentially decays in the PML. The absorbing function we shall use in our implementation of PMLs was proposed by Bermúdez et. al [150], and is given by

$$\sigma(x) = \begin{cases} 0 & x \in [0, X], \\ \frac{1}{X + \delta - |x|} & x \in [X, X + \delta]. \end{cases} \quad (6.23)$$

Therefore our solution in this case is

$$u(x) = \begin{cases} e^{ikx} & x \in [0, X], \\ e^{ikx} \left(1 - \frac{|x| - X}{\delta}\right) & x \in [X, X + \delta]. \end{cases} \quad (6.24)$$

From the above formulation it can be seen that the Bermúdez absorbing function leads to solutions that decay linearly to zero across the width of the PML. A plot of this solution is given in 6.5.

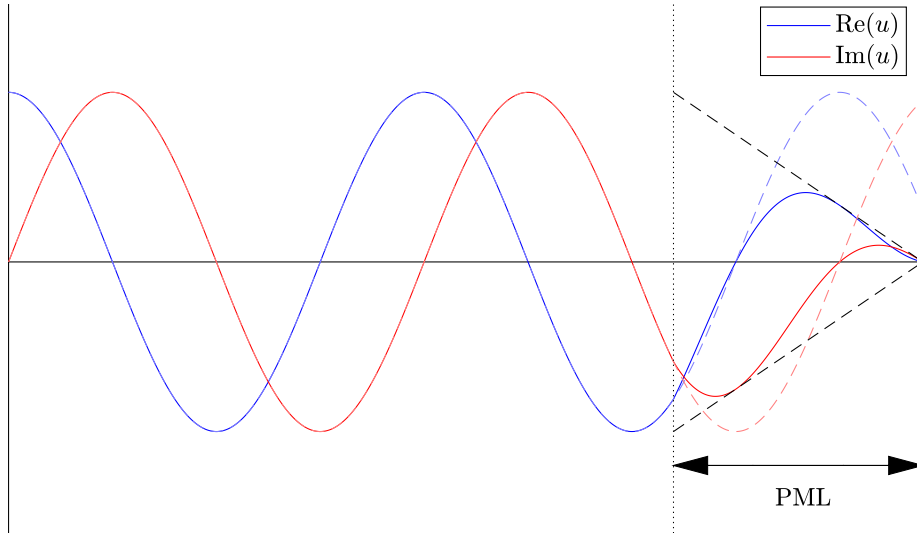


Figure 6.5: Plot of real and imaginary components of equation (6.24). Dashed black lines show the linear decay envelope in the PML region. Dashed red and blue lines indicate the solution in the absence of the PML.

A similar derivation can be made in 3 dimensions. The Helmholtz equation in transformed coordinates is now

$$\tilde{\nabla} \cdot (\tilde{\nabla} u) + k^2 u = 0. \quad (6.25)$$

Just as in the 1D case the transformed coordinates have been mapped to the complex plane inside the PML region, except now  $\tilde{\mathbf{x}}(\mathbf{x})$  is a vector. Writing the Helmholtz equation in terms of  $\mathbf{x}$  gives

$$\left(\underline{\underline{\gamma}}^{-1}\right)^T \nabla \cdot \left(\left(\underline{\underline{\gamma}}^{-1}\right)^T \nabla u\right) + k^2 u = 0, \quad (6.26)$$

where the Jacobian of the transformation  $\underline{\underline{\gamma}}$ , is now the matrix

$$\gamma_{ij} = \frac{\partial \tilde{x}_i}{\partial x_j}. \quad (6.27)$$

The simplest case of PMLs in 3D is given by the axis-aligned case, where PMLs are perpendicular to the  $x$ ,  $y$  and  $z$  axes respectively. Here we shall consider our domain of interest to be a cuboid bounded by  $|x| < X$ ,  $|y| < Y$  and  $|z| < Z$ . In this case, the Jacobian is

$$\underline{\underline{\gamma}} = \begin{pmatrix} \gamma_x & 0 & 0 \\ 0 & \gamma_y & 0 \\ 0 & 0 & \gamma_z \end{pmatrix}, \quad (6.28)$$

where

$$\gamma_{x_i} = 1 + \frac{i}{k}\sigma(x_i). \quad (6.29)$$

In this case, the elements of the Jacobian are identical to the Jacobian in the 1D case along their respective axes.

We will now consider some simple PMLs in both spherical polar and cylindrical polar coordinates, denoted by  $(r, \theta, \phi)$  and  $(\varrho, \varphi, z)$  respectively. In the spherical case, we shall define our PML to be the region  $r \in [R, R + \delta]$ , which is a spherical shell that surrounds the domain of interest. In the cylindrical case we shall define our PML to be a similar region  $\varrho \in [R, R + \delta]$ , which is a cylindrical annulus that surrounds the domain of interest. It can be noticed that in both these cases we only need to transform our coordinates along the radial axis, hence we find the Jacobians to be

$$\underline{\underline{\gamma}}^s = \begin{pmatrix} \gamma_r & 0 & 0 \\ 0 & 1 & 0 \\ 0 & 0 & 1 \end{pmatrix}, \quad \underline{\underline{\gamma}}^c = \begin{pmatrix} \gamma_\varrho & 0 & 0 \\ 0 & 1 & 0 \\ 0 & 0 & 1 \end{pmatrix}, \quad (6.30)$$

where  $\gamma_r$  and  $\gamma_\varrho$  are simply given by equation (6.29), where  $x_i$  in this case is the radial coordinate in each respective coordinate system. When implementing PMLs in numerical models it is often useful to give them in terms of Cartesian coordinates. This may be done by expanding the Jacobian:

$$\gamma_{ij} = \frac{\partial \tilde{x}_i}{\partial x_j} = \frac{\partial \tilde{x}_i}{\partial \tilde{\eta}_k} \frac{\partial \tilde{\eta}_k}{\partial \eta_l} \frac{\partial \eta_l}{\partial x_j}. \quad (6.31)$$

Here  $x_i$  represents the Cartesian coordinate system and  $\eta_i$  represents a polar coordinate system.

### 6.4.6 The finite element method

Due to the complicated geometries of many real-world problems a variety of numerical methods have been developed to solve different partial differential equations (PDEs), such as the Helmholtz equation, when analytical solutions are impossible to attain. Here we shall focus on one of the most widely used methods, the finite element method (FEM).

To begin with, FEM requires equations to be rewritten in their weak formulation. This is done by multiplying by a ‘test function’  $\phi$  and integrating over the whole domain  $\Omega$ . For the Helmholtz equation, this gives

$$\int_{\Omega} (\nabla^2 u + k^2 u) \phi dV = 0 \quad (6.32)$$

where, using Green’s first identity, we may rewrite the equation as

$$\int_{\Omega} \nabla u \cdot \nabla \phi dV - \int_{\partial\Omega} \phi(\nabla u) \cdot \hat{\mathbf{n}} dS - \int_{\Omega} k^2 u \phi dV = 0 \quad (6.33)$$

Here both  $u$  and  $\phi$  are assumed to be elements of Hilbert spaces, and we shall assume that both  $u$  and  $\phi$  belong to the same Hilbert space  $H$ .

The function space to which our functions belong,  $H$ , is infinite dimensional. To be able to find numerical solutions to  $u$  we require our functions to exist in a finite-dimensional space. Therefore, we construct the approximation

$$u \approx u_h = \sum_{i=1}^n u_i \psi_i(\mathbf{x}). \quad (6.34)$$

Here we have split our function into  $n$  subdomains called elements. On each element, we approximate the field with a linear combination of polynomial shape functions  $\psi_i$ , of order  $p$ . Shape functions are only non-zero inside the element they are associated with. Meaning these shape functions form an orthonormal basis for the domain  $\Omega$ , since the L2 norm over the domain  $\langle \psi_i, \psi_j \rangle_{L2}$  is only non-zero if  $i \neq j$ . A simple model example of discretisation using shape functions is shown in figure 6.6. In the Galerkin method, test functions are chosen to be given by the basis function  $\psi_j$ , hence

$$\begin{aligned} \sum_i u_i \int_{\Omega} \nabla \psi_i \cdot \nabla \psi_j dV - \sum_i u_i \int_{\partial\Omega} \psi_j (\nabla \psi_i) \cdot \hat{\mathbf{n}} dS \\ - \sum_i k^2 u_i \int_{\Omega} \psi_i \psi_j dV = 0. \end{aligned} \quad (6.35)$$

If we now chose  $n$  test functions  $\psi_j$ , we form a system of  $n$  equations, with  $n$  unknown coefficients  $u_i$ .

Our system of equations can now be discretised and boundary conditions enforced. This leads to a problem of the form

$$\mathbf{A} \mathbf{u}_h = \mathbf{b}, \quad (6.36)$$

which is a linear system of equations where  $\mathbf{u}_h$  is the vector containing the coefficients  $u_i$ ,  $\mathbf{A}$  is an  $n \times n$  matrix containing the coefficients of  $u_i$  in each equation  $j$  and  $\mathbf{b}$  is an  $n$  dimensional vector. Linear systems of equations, such as equation (6.36), are ubiquitous in maths and physics, hence a multitude of numerical methods have been developed to tackle such problems. These include Gauss-Jordan elimination, lower-upper factorization, eigenvalue decomposition and singular value decomposition [153], [154].

We have shown how to formulate the FEM to solve the Helmholtz equation (6.11), but as mentioned previously FEM can be used to solve a variety of PDEs. We will not demonstrate it here but it can be shown that an almost identical formulation is needed in order to solve equation (6.26) using FEM [150].

## 6.5 Validating our numerical model

Due to the geometry of our physical set-up, it was found that reflected pressure waves contributed significantly to the total acoustic field. Since our transducers

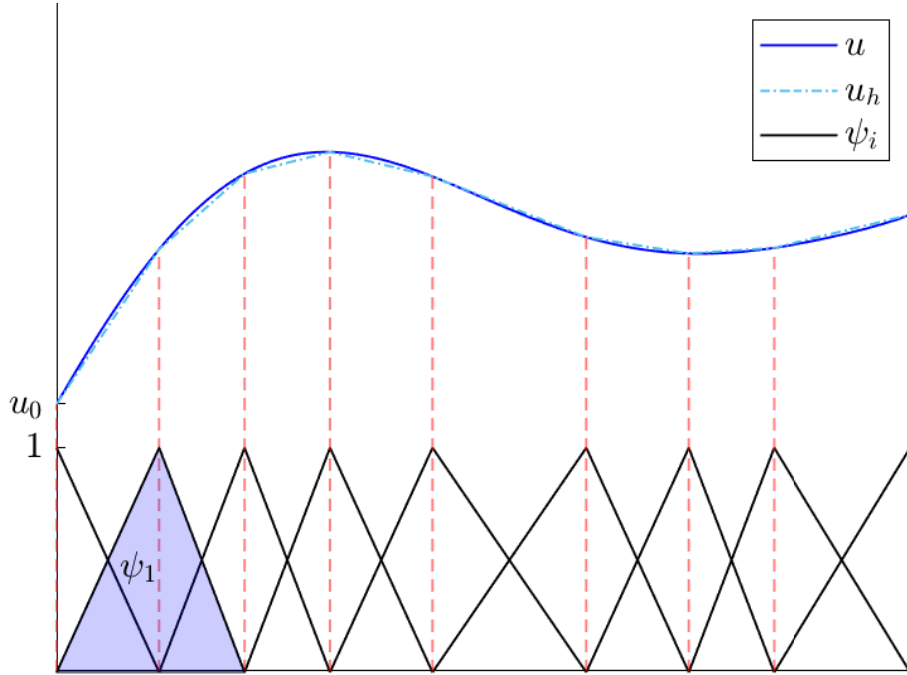


Figure 6.6: 1D example of discretisation of a function using order 1 polynomial shape functions. Here the blue curve  $u$  has been approximated with  $u_h$  (dot-dash blue line), where  $u_h$  is constructed from a linear combination of polynomial shape functions  $\psi_i$  (black lines). The shaded blue region denotes a single shape function, which is equal to unity at node 1 but zero at all other nodes.

were mounted on the inside of a cylindrical surface we were unable to model these reflections using the matrix method described in section 6.4.3. Therefore, we solved the Helmholtz equation inside the domain, as described in section 6.4.4. PMLs were employed on certain edges of the domain as they required open boundary conditions. To do this we used the open source software package FreeFEM to solve equation (6.26) using FEM [155]. An introduction to the FreeFEM code base and language is available at the FreeFEM website [156]. A large number of examples are given on the FreeFEM website, of significant interest to anyone trying to recreate the simulations presented in this thesis is the example *acoustics*. An additional resource that helpfully shows how to implement PMLs in FreeFEM is given in the accompanying example scripts created for use with the book Laude [157].

To validate our implementation of PMLs in FreeFEM we compared calculations of the pressure field for a circular piston source embedded in a planar surface to solutions computed using the Rayleigh-Sommerfeld integral (6.7). Here we take our transducer to be at the origin pointing along the  $z$  axis, hence we only consider the domain  $z > 0$ .

Figure 6.7 shows plots of the gauge pressure (change in pressure relative to the

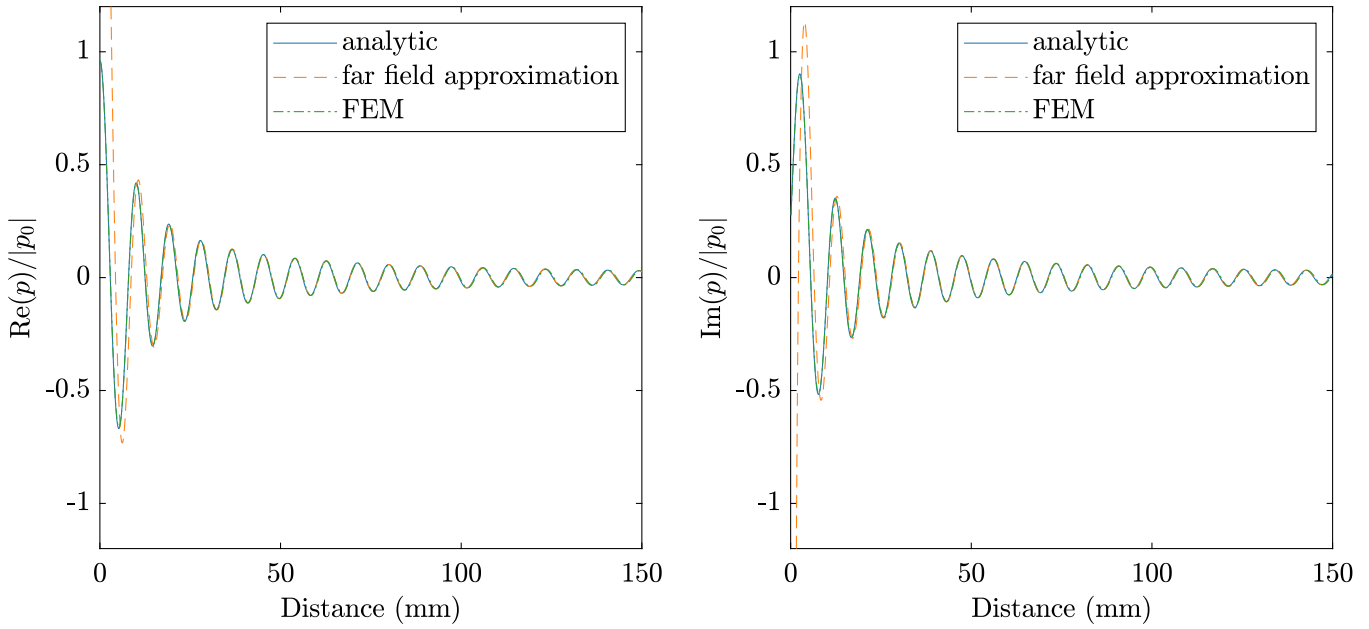


Figure 6.7: Plots of pressure along the central axis of the transducer for both real (left) and imaginary (right) components of pressure.

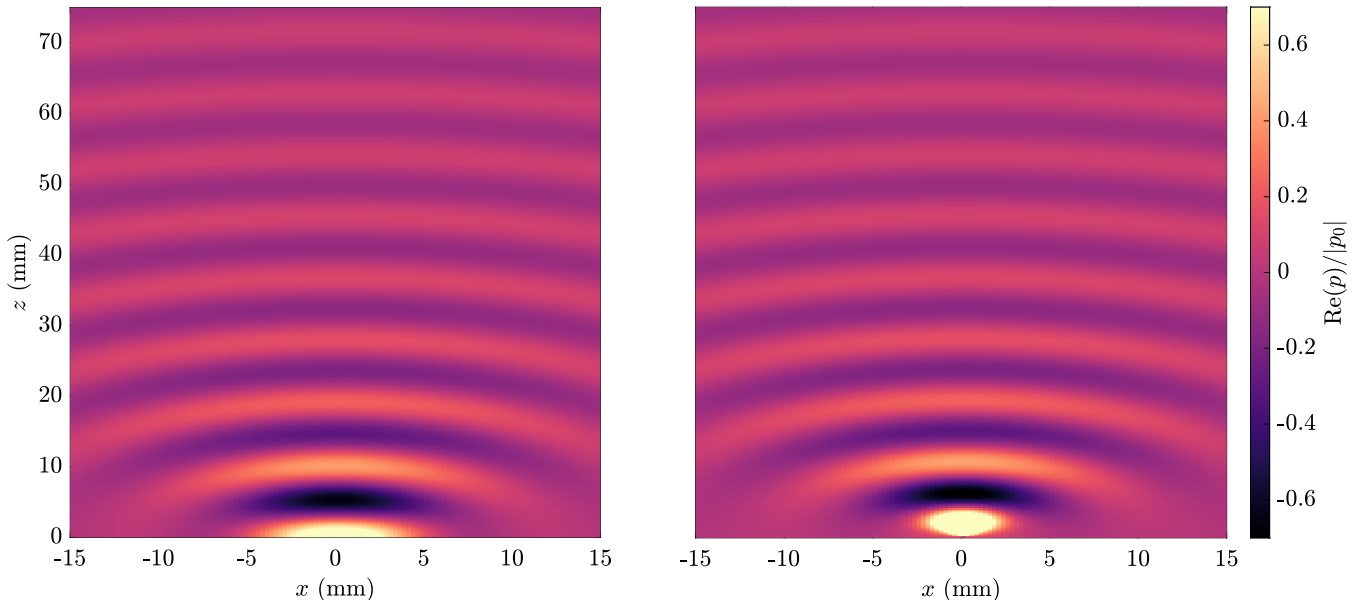


Figure 6.8: Plots of the Real component of the pressure field for the FEM solution (left) and the far field approximation (right).

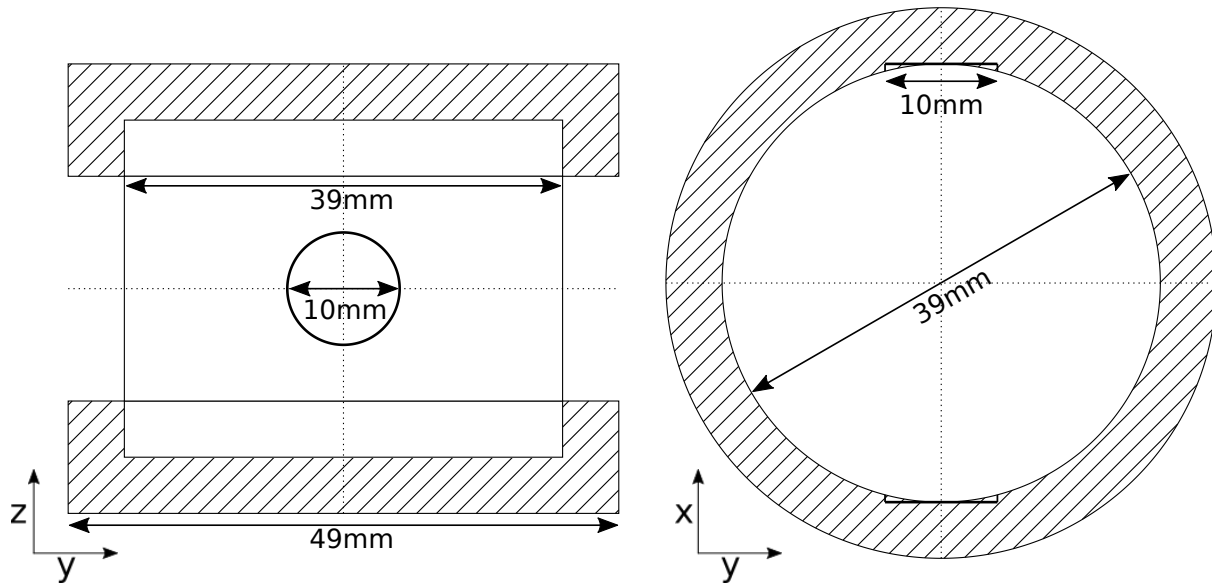


Figure 6.9: Schematics showing the geometry of the numerical domain. Dashed regions denote perfectly matched layers and dotted lines denote symmetry planes.

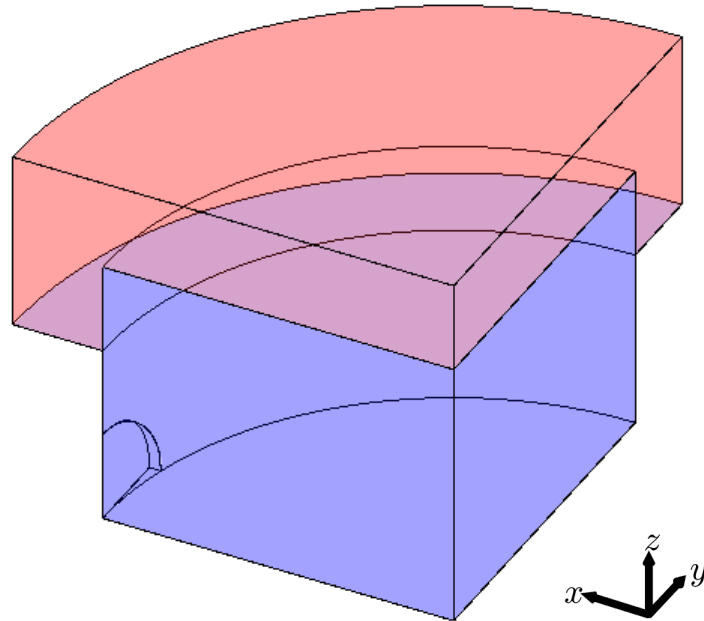


Figure 6.10: 3D rendering of numerical domain used in simulations. The red region denotes Perfectly matched layers.

background atmospheric pressure) along the central axis of a 10 mm diameter transducer. Here we set the frequency of the transducer to be oscillating at 40 kHz, where the speed of sound in air was taken to be  $346 \text{ m s}^{-1}$ . We shall define  $p_0$  to be the pressure at the central point on the surface of the transducer, which is simply equation (6.7) evaluated at  $z = 0$ . For these examples, we have normalised all our pressure fields using  $|p_0|$ . From figure 6.7 it can be seen that there is good agreement between the analytical solution and our FEM solution. The far field approximation is seen to approach both the analytical and FEM solutions after approximately 1–2 wavelengths, as expected. Surface plots of the pressure field for the FEM solution and the far field approximation are shown in figure 6.8. The far field approximation and FEM solution are in excellent agreement, except for the region within 1–2 wavelengths of the surface of the transducer.

## 6.6 Numerical domain

Here we present the numerical domain used to simulate the pressure field in experiment. We modelled the volume of the domain inside the ring by the union of the volume of two cylinders, one of diameter 39 mm with its central axis orientated along the vertical axis  $z$ , and one of diameter 10 mm with its central axis orientated perpendicular to  $z$ , which we shall label  $x$ , where the faces of the second cylinder were tangent to the edge of the first cylinder (see figures 6.9 and 6.10).

Outside the PLA ring open boundary conditions were required. We implemented these using PMLs at the edges of these regions, see figures 6.9 and 6.10. We did not model the inside of the magnet bore and instead enforced open boundary conditions on the edge of the domain instead. This is because the magnet bore was sufficiently far away from the internal domain of the ring that reflections from the wall were minimal. Doing this allowed for a reduction in the overall domain volume, so a reduction in computational costs. The symmetry of the problem allowed us to reduce the domain to the 'wedge-shaped' domain shown in figure 6.10, further reducing the computational cost.

## 6.7 Amplitude of acoustic potential

To calculate the Gor'kov potential our simulations required two input parameters: the wavenumber  $k = \omega/c_2$  and the root mean square velocity of the transducer faces,  $v_{rms}$ . The speed of sound in air may be calculated from the ideal gas law with the equation

$$c_2 = C\sqrt{T_0 + T}, \quad (6.37)$$

where  $C = 20.05 \text{ m s}^{-1} \text{ K}^{-1/2}$ ,  $T_0 = 273.16 \text{ }^\circ\text{C}$  is the conversion factor from degrees Celsius to degrees Kelvin and the temperature in our lab was  $T = 20 \pm 2 \text{ }^\circ\text{C}$ .

It is known that the pressure field produced by a circular piston using the planar piston model is directly proportional to the velocity of the surface of the transducer

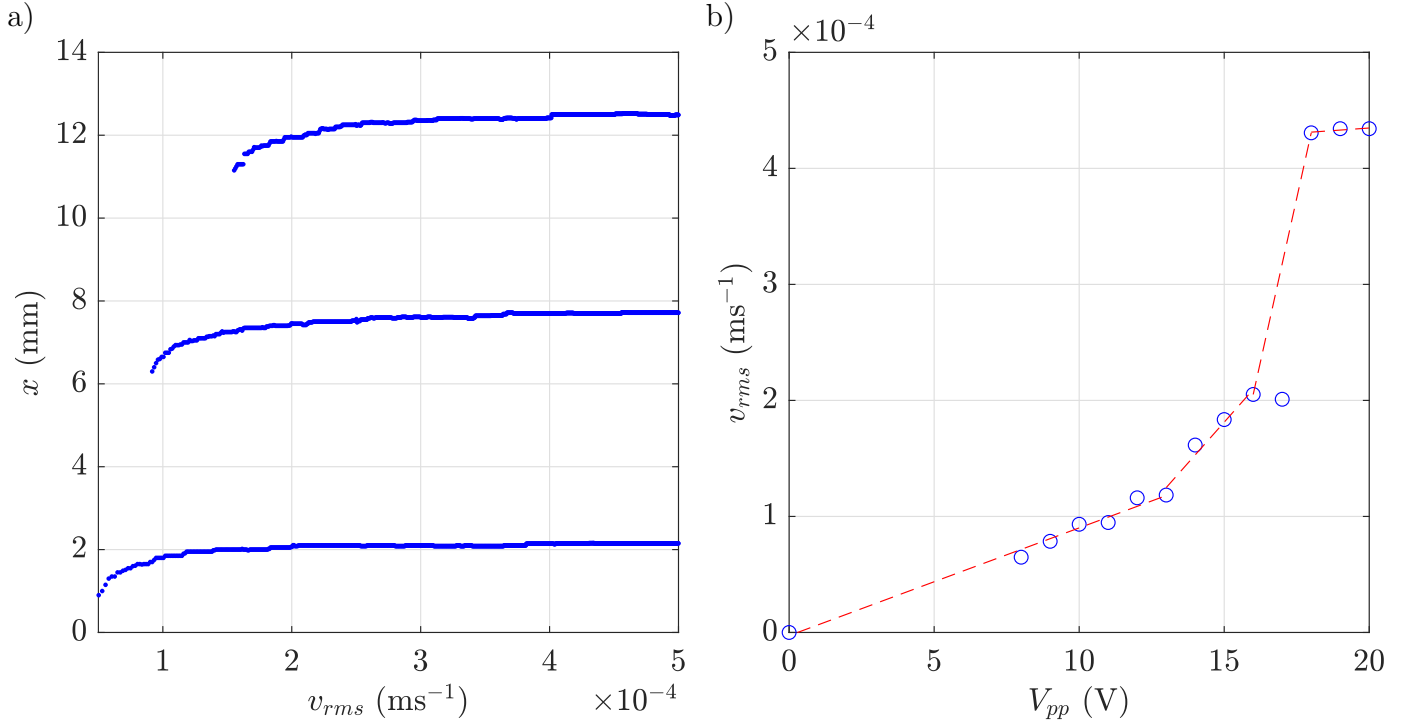


Figure 6.11: a)  $x$  coordinates of minima in  $U_{total}$  as a function of the velocity of the surface of the transducer, for the transducer operating frequency 37.4 kHz.  $U_{total}$  was found from simulation, as described in the text. Multiple stable levitation points exist for a single value of  $v_{rms}$ . b)  $v_{rms}$  as a function of peak-to-peak voltage, for our transducers operating at a frequency 37.4 kHz. Dashed red lines is a piecewise linear function fitted to the data.

$v$ . The velocity  $v$  is a function of the voltage supplied to the transducer and the angular frequency of the transducer, i.e.,  $p(\mathbf{x}, \omega) \propto v(V_{pp}, \omega)$ , where  $p$  is the pressure at a location  $\mathbf{x}$  in the domain and  $V_{pp}$  is the peak-to-peak voltage used to drive the transducers.

We determined the relationship between  $v_{rms}$  and  $V_{pp}$  experimentally. To find this relationship we obtained the  $|x|$  coordinate of stable levitation points as a function of  $v_{rms}$  from simulation (see figure 6.11a). Due to the symmetry across the  $y = 0$  plane if a stable levitation point exists at  $x$  one must also exist at  $-x$ . It should be noted that multiple stable levitation points may occur for a single value of  $v_{rms}$  (see figure 6.11a). We shall denote the location of the innermost stable levitation point as  $x_1(v_{rms})$  and the adjacent levitation point as  $x_2(v_{rms})$ .

We then compared these results to experimental results of stable levitation points as a function of  $V_{pp}$ . We stably levitated four droplets in the four most central traps of our Sonomaglev setup at  $V_{pp} = 20$  V and recorded their  $x$  positions. We then incrementally decreased  $V_{pp}$  by 1 V until the droplets became unstable and eventually coalesced until a single droplet residing at  $x = 0$  mm, recording the  $x$  position of the stably levitating droplets at each voltage. Multiple droplets stably levitated in

our setup for  $V_{pp} = 8\text{--}20\text{V}$ . We calculated the mean  $|x|$  location for the inner two and outer two droplets respectively, to obtain an average value for the experimental  $x$  location of stable levitation points. We shall denote the average  $x$  location of the innermost stable levitation point as  $X_1(V_{pp})$  and the outermost stable levitation point as  $X_2(V_{pp})$ .

To calculate the relationship between  $V_{pp}$  and  $v_{rms}$ , we found the value of  $v_{rms}$  which minimised

$$\sqrt{\left(x_1(v_{rms}) - X_1(V_{pp})\right)^2 + \left(x_2(v_{rms}) - X_2(V_{pp})\right)^2}$$

for each value of  $V_{pp}$ . In the case  $X_2(V_{pp})$  didn't exist we found the value of  $v_{rms}$  which minimised

$$x_1(v_{rms}) - X_1(V_{pp}).$$

The maximum value from either of these procedures was found to be 0.017 mm. For the transducers operating at a frequency of 37.4 kHz we found  $v_{rms} \propto V_{pp}$  for  $V_{pp} \leq 13$  V. For  $V_{pp} > 13$  V  $v_{rms}$  varies non-linearly with  $V_{pp}$ , and plateaus at  $v_{rms} \approx 4.3 \times 10^{-4} \text{ m s}^{-1}$  for  $V_{pp} \gtrsim 18$  V. A continuous piecewise linear fit was fitted to the data, as can be seen in figure 6.11b.

## 6.8 Results

### 6.8.1 Levitation of multiple droplets

Figure 6.12a shows a contour plot of the magnetogravitational potential energy density  $U_{mg}$  for water in air. The blue circle in the figure marks the location of a local minimum in  $U_{mg}$ , i.e. the location of the stable levitation point. We take this point to be the origin of a coordinate system in which the  $x - y$  plane is perpendicular to the axis,  $z$ , of the solenoid, and in which the  $x$  axis intersects the centres of the faces of both transducers. The magnetic field strength at this point is  $B \approx 11$  T.

Figure 6.12b and c show plots of the total potential energy density. The simulations show that the addition of the acoustic field modulates the potential energy density,  $U_{total}$ , giving rise to multiple potential minima, ‘wells’, along the  $x$ -axis (fig. 6.12b, c). Unlike  $U_{mg}$ ,  $U_{total}$  is not cylindrically symmetric about the  $z$  (solenoid) axis. Figure 6.12b shows  $U_{total}$  in the  $y = 0$  plane. Blue circles indicate the positions of each well. The two central wells lie on the  $x$ -axis, i.e. on the line passing through the centres of the two acoustic transducers. The vertical,  $z$ , location of each well increases as a function of  $|x|$ , increasing to  $z = 3$  mm for the wells farthest from the axis, at  $|x| = 17$  mm. This variation in height results from the shape of  $U_{mg}$ , in particular an octupole contribution to  $U_{mg}$ . Figure 6.12c shows  $U_{total}$  in the  $z = 0$  plane, and includes a photograph of levitating droplets taken from an angle looking down the bore (i.e. down the  $z$  axis), superposed on the contours.

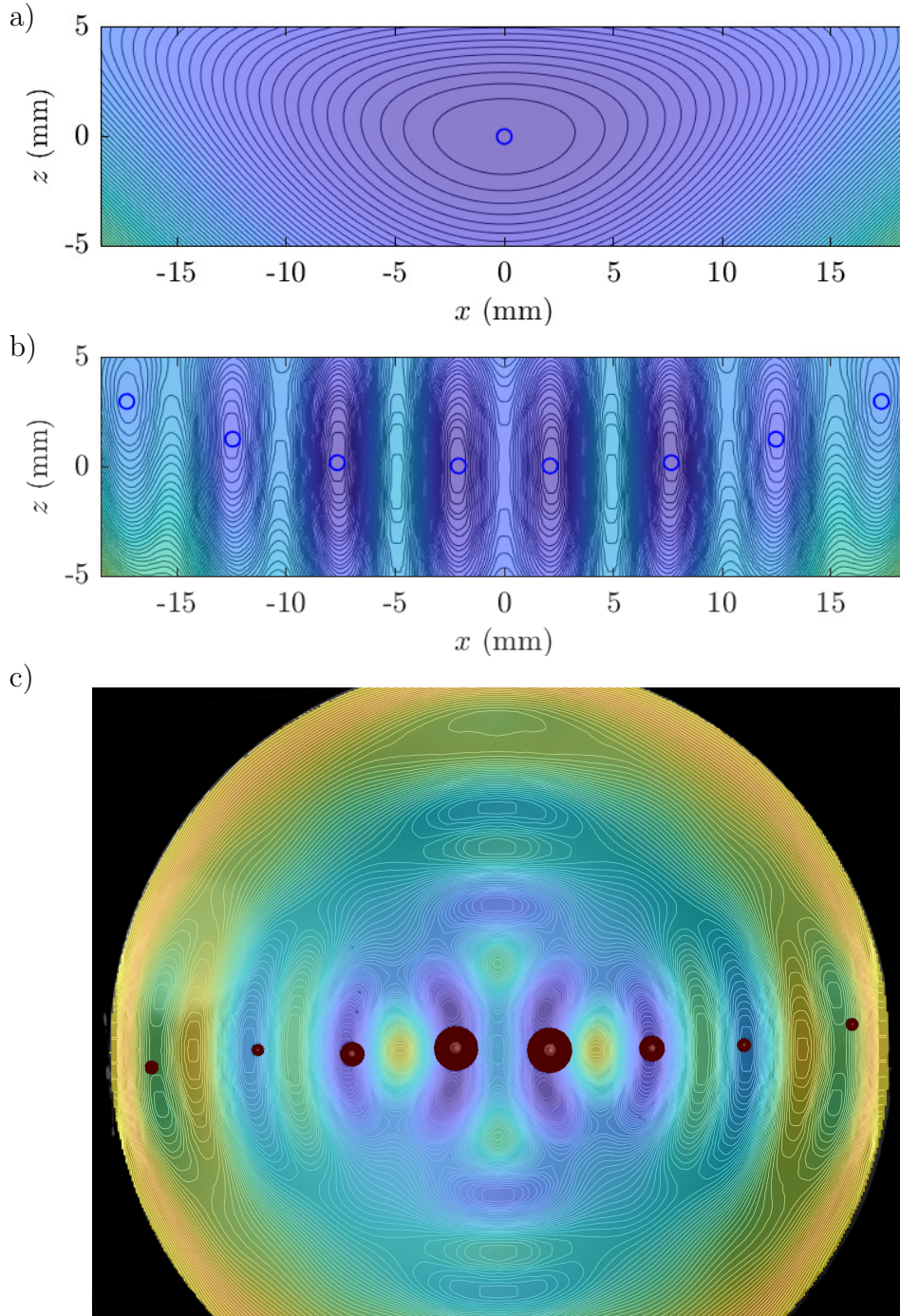


Figure 6.12: a) Slice through the calculated magnetogravitational potential,  $U_{mg}(x, y, z)$ , in the  $y = 0$  plane. The coordinates  $x, y, z$  are as defined in figure 6.1; the location of the local minimum in  $U_{mg}$  (blue circle) defines their origin. b) Slice through the calculated total potential  $U_{total}(x, y, z)$ , which is the sum of  $U_{mg}$  and the acoustic potential  $U_{acoust}$ , in the  $y = 0$  plane. Blue circles indicate the local minima. N.b.: whereas  $U_{mg}$  is cylindrically symmetric about the  $z$  axis,  $U_{total}$  is not. c) Slice through  $U_{total}(x, y, z)$  in the  $z = 0$  plane. The locations of the minima closest to the bore axis lie on this plane; the others lie at slightly higher  $z$  as shown in the centre panel. The superposed photograph shows water droplets levitating at local minima in  $U_{total}$ .

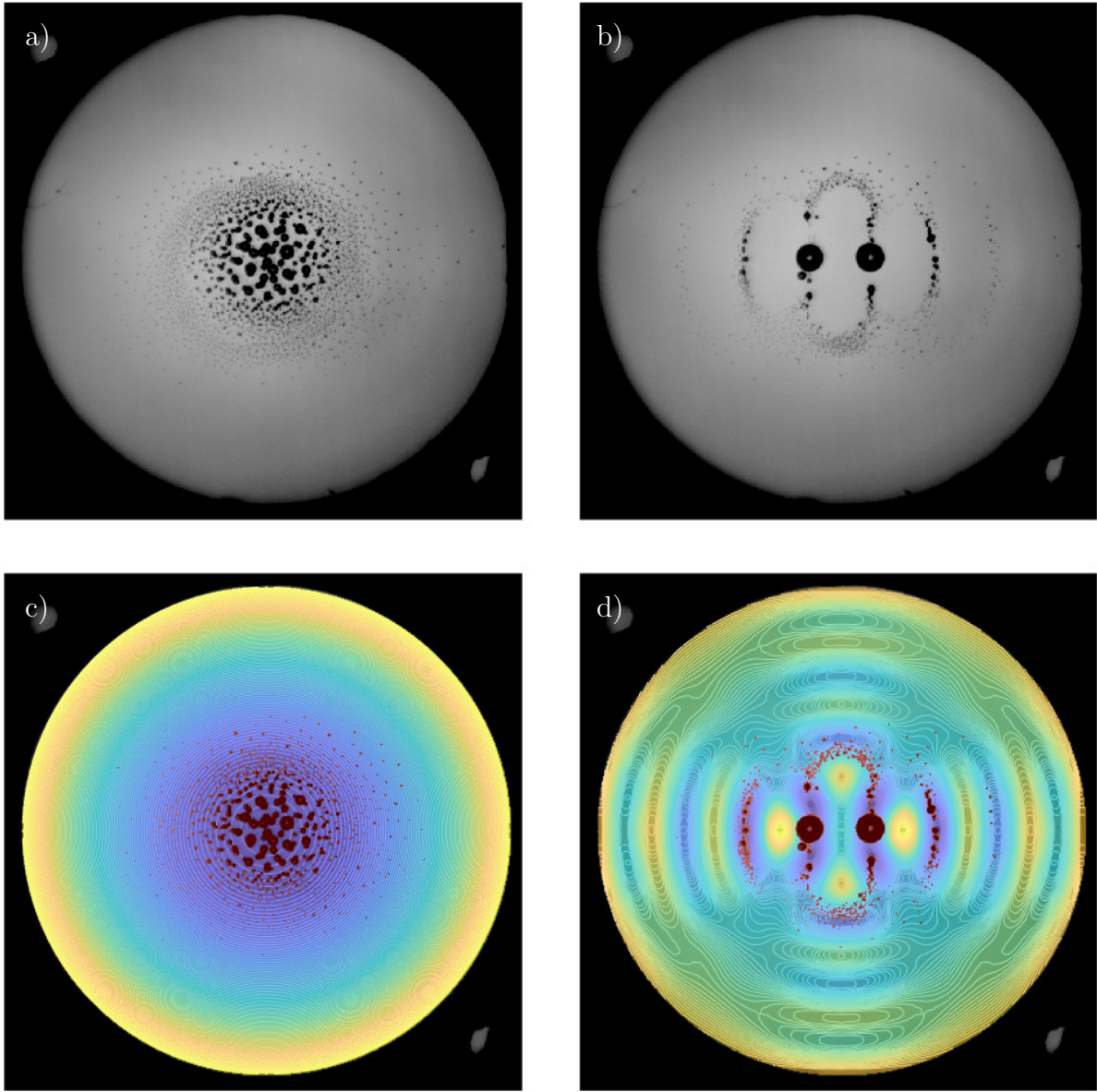


Figure 6.13: Images of a cloud of charged droplets before a) and c), and after b) and d), the addition of the acoustic field. Figures a) and b) display images taken from experiment. Figures c) and d) display the same images overlaid with a slice through  $U_{total}$  in the  $z = 0$  plane. Droplets are coloured red to differentiate them from the background.

### 6.8.2 Visualising ultrasound fields using charged droplet clouds

Figure 6.13a,c shows a cloud of charged droplets levitating in the bore of the Cryogenic magnet in the absence of an acoustic field. Due to electrostatic forces between

the droplets they collectively form the shape of the magnetogravitational potential trap, so as to minimise the total energy of the system. The shape of the trap in the  $x - z$  plane is given in figure 6.12a. Due to the limitation of our imaging set-up, we were only able to capture a top-down view of the droplet cloud, as inserting an object such as a mirror into the PLA ring would affect the acoustic field. From this view the droplet cloud is observed to attain a circular shape, as expected due to the rotational symmetry of the magnetogravitational potential trap.

Figures 6.13b,d shows the same charged droplet cloud as in 6.13a,c with the ultrasonic transducers powered with  $V_{pp} = 20$  V. The addition of the acoustic field applies additional acoustic radiation forces to the droplets resulting in rearrangement of the droplets as they find the minimum energy of the new system. The number and size of the droplets in figure 6.13 can be seen to differ before and after the addition of the acoustic field. This is due to droplets undergoing coalescence, as the addition of acoustic radiation forces overcame the electrostatic forces separating certain droplets, leading to the growth of several larger droplets observed near the axis of the magnet bore (figure 6.13b,d). The creation of additional smaller droplets was also observed, due to the ejection of satellite droplets during droplet coalescence [158].

Droplets rearranging themselves to minimise the total energy of the system leads to them residing in the potential wells of  $U_{total}$ . Figure 6.13a,b display the charged droplet cloud before and after the addition of the acoustic field, whereas figure 6.13c,d displays the same experimental images but overlaid on contours of  $U_{total}$  at  $z = 0$ . Although only a 2D slice of  $U_{total}$  in the  $x - y$  plane is displayed in these plots, by comparing them to figure 6.12a,b it can be seen that potential wells to a good approximation occupy the same horizontal extent independent of vertical location close to their minima, but the minima of the wells occur at different horizontal locations, hence the cross section at  $z = 0$  gives a good representation of the shape of potential wells.

From figure 6.13 it is clear that the ensemble of charged droplets are able to denote the location of potential wells in  $U_{total}$ , hence allowing for the visualisation of the wells by imaging the droplets. Good agreement is found between the experimental location of the charged droplets and the simulated shapes of potential wells, see figure 6.13c,d.

### 6.8.3 Positioning of levitated droplets

We were able to adjust the horizontal ( $x$ ) positions of the levitating droplets by varying the peak-to-peak voltage  $V_{pp}$  applied to the transducers. Figure 6.14 shows a montage of photographs displaying the horizontal position of two levitated water droplets close to the solenoid axis as a function of  $V_{pp}$ . In this particular experiment, the larger of the two droplets, which was closest to the solenoid axis had a diameter of  $1.93 \pm 0.05$  mm and the smaller of the droplets, which was situated at positions further away from the axis, had a diameter of  $1.19 \pm 0.05$  mm. The uncertainty in the measurement of the diameters of the droplets is attained from the resolution

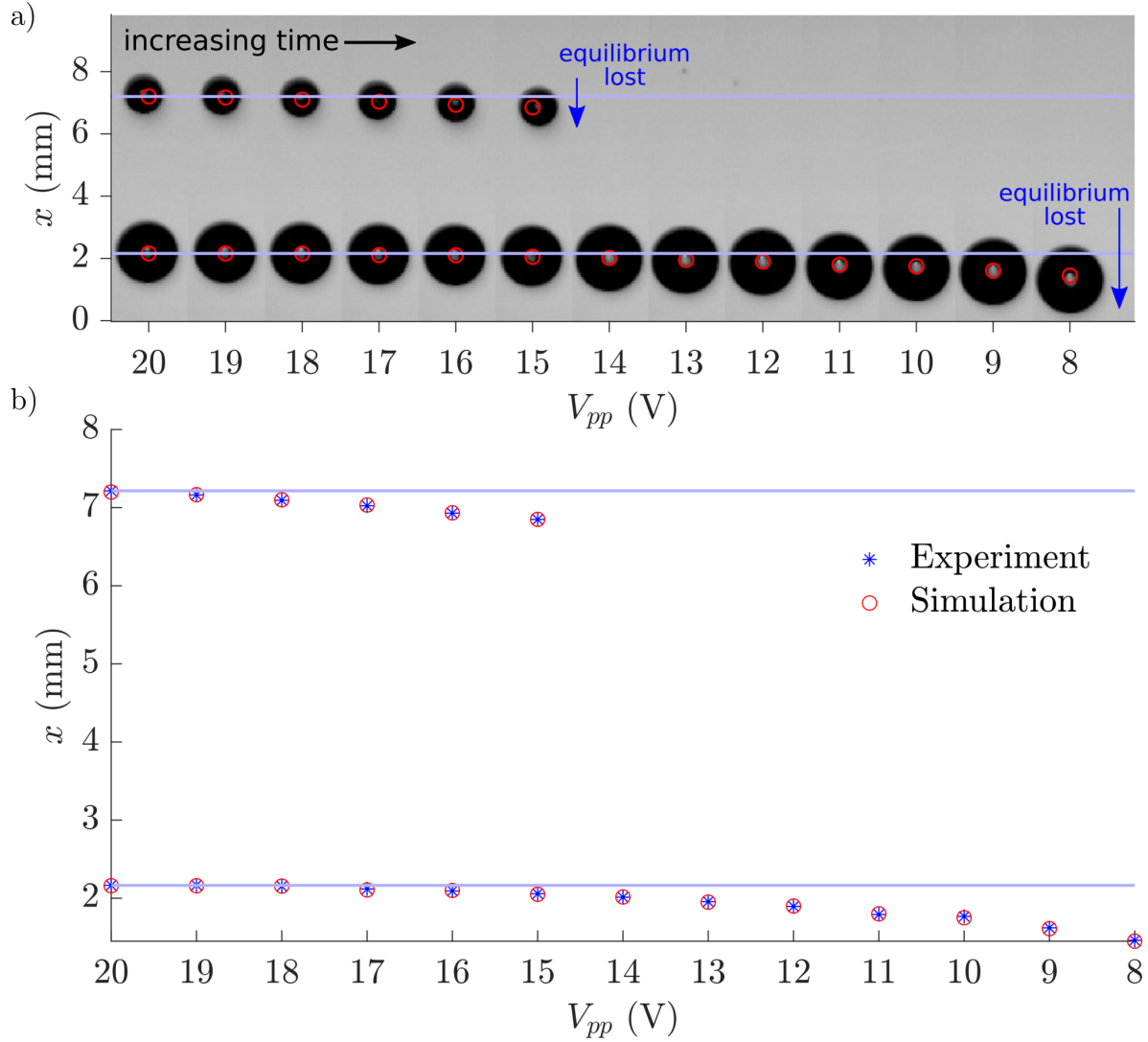


Figure 6.14: a) Montage of images of two levitating droplets showing the variation in their horizontal position,  $x$ , as  $V_{pp}$  was reduced from 20 V to 8 V. Down-pointing arrows indicate the voltage below which droplets lost equilibrium. b) Measured  $x$ -coordinates of the centres of the droplets. In both plots, red circles show the calculated  $x$ -coordinates of local minima in  $U_{total}$ . The blue unbroken lines indicate the  $x$ -coordinates of the two minima at  $V_{pp} = 20$  V.

of the optical set-up. Note that, since the total potential energy density,  $U_{total}$ , is independent of volume, the positions of the stable equilibrium points are independent of the volume of the droplets. When the transducers were driven with a peak-to-peak voltage of  $V_{pp} = 20.0$  V, the larger droplet levitated with its centre at  $x = 2.16 \pm 0.03$  mm and the smaller levitated with its centre at  $x = 7.21 \pm 0.03$  mm, were the levitation of both was stable. When the voltage was decreased from  $V_{pp}$  from 20 V to 15 V, the position of the smaller droplet decreased from  $x = 7.21$  mm

to  $6.85 \pm 0.03$  mm, while the position of the larger droplet decreased slightly from  $x = 2.16$  mm to  $2.06 \pm 0.03$  mm. On decreasing the voltage further to  $V_{pp}$  15 V, the smaller of the two droplets lost equilibrium, as the depth of the local potential well was reduced to zero, and the smaller droplet ‘fell’ towards the larger droplet, resulting in coalescence between the two droplets. Further decreasing  $V_{pp}$  from 14 V to 8 V, we found that the equilibrium position of the centre of the remaining large droplet decreased from  $x = 2.06$  mm to  $1.50 \pm 0.03$  mm. Below  $V_{pp} = 8$  V, this droplet also lost equilibrium and ‘fell’ radially towards the solenoid axis, finding a new equilibrium position at the origin. The equilibrium positions obtained from both simulation and experiment are shown together in figure 6.14, for comparison.

#### 6.8.4 Whispering gallery modes

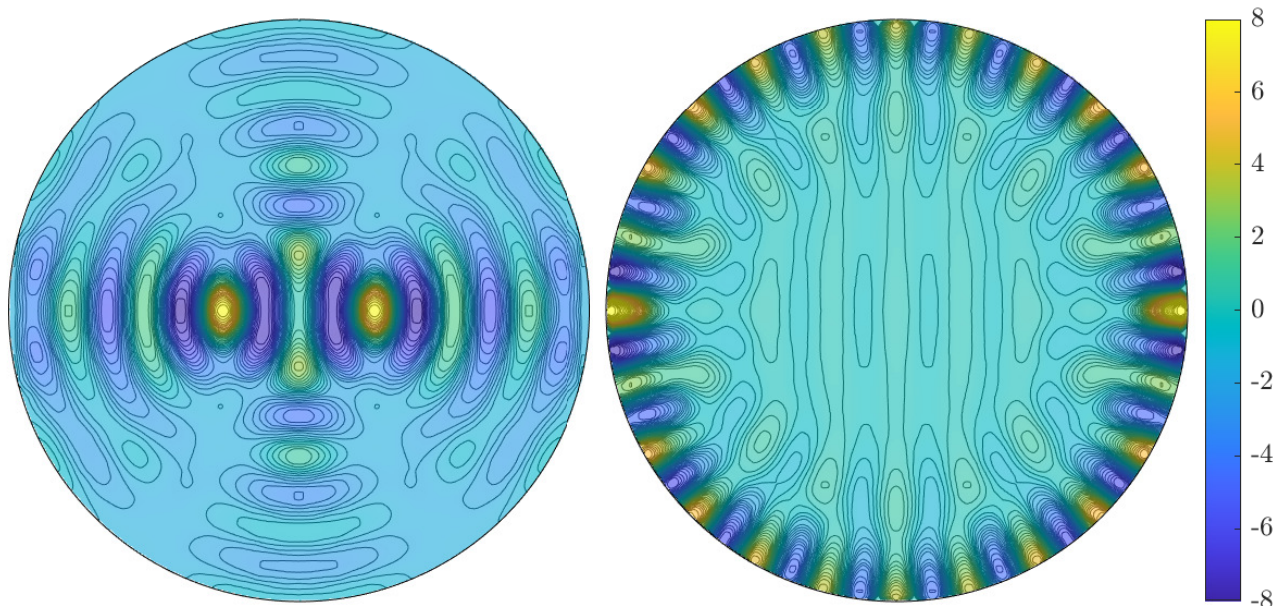


Figure 6.15: Contour plots of a horizontal cross-section of  $U_{acoust}$  along the  $z = 0$  plane. Transducer operating frequency is 37.4 kHz (left) and 40 kHz (right). Here  $U_{acoust}$  has been normalised by  $v_{rms}^2$  allowing for direct comparison between frequencies.

In experiments, the transducer operating frequency was varied between 37–40 kHz. The nominal resonant frequency of the transducers used in our experiments was 40 kHz. It was found that due to the geometry of the domain, ‘whispering gallery modes’ were excited when the operating frequency approached 40 kHz (see figure 6.15) [159]. This is due to the fact the wavelength of the acoustic fields produced by the transducers operating at 40 kHz is  $\lambda = 8.575$  mm, where the diameter of the

PLA ring is approximately  $4.5\lambda$ . In this configuration, the depth of each potential well was much reduced compared to the configuration at lower operating frequencies, which made it experimentally more difficult to trap droplets.

## 6.9 Summary

In this chapter, we have demonstrated that by combining techniques from both acoustic and diamagnetic levitation, we can stably trap quiescent liquid droplets in a series of potential wells arrayed along a horizontal line, and that the location of these traps, and thus the droplets, may be varied precisely. By using diamagnetic levitation to balance the vertical gravitational force on the droplets, the sound pressure levels generated to make use of techniques from acoustic levitation were much reduced compared to those of an acoustic levitator:  $\sim 110$  dB compared to 150–165 dB [132], a greater than 100-fold reduction in the amplitude of the pressure. Due to this reduced sound level, we did not observe phenomena such as vibration of the droplets, deformation of their equilibrium shape, or instabilities in their position, which are characteristic of acoustic levitators [1], [126], [130]. Several disciplines may find this technique useful for a number of applications, such as in areas where particularly delicate handling of material is required, where evaporation and cooling by the oscillating air flow are problematic or where control over the internal droplet flow is important. Many common techniques used in biochemical analysis are compatible with a strong magnetic field, such as fluorescence microscopy [160], Raman spectroscopy [161], and light scattering [162]. Hence these techniques could be used in conjunction with future sonomaglev systems allowing for the analysis of levitated samples.

The combination of magnetic and acoustic forces creates additional possibilities to manipulate the droplets: here, we demonstrated controlled contactless coalescence of two droplets by varying the ratchet-like potential  $U_{total}$ , using a relatively simple acoustic set-up consisting of two low-power transducers, a feat that otherwise requires large transducer arrays [163], [164]. Droplets can also be moved vertically by adjusting the electric current in the solenoid. With the addition of more acoustic transducers, we anticipate that this flexibility will allow the creation of a system that can provide spatial positioning in three directions within the bore of the magnet.

We also demonstrated a new technique to visualise the acoustic fields utilised in experiments throughout this chapter. A number of techniques have previously been developed to visualise acoustic fields such as: schlieren [165], [166], shadowgraphy [165], [166], synthetic schlieren [166], [167] and optical feedback interferometry [168]. All these techniques rely upon the use of light, to image the acoustic field. This is due to the fact small variations in the density of fluids leads to a localised variation in the refractive index, which distorts the light rays passing through the medium and therefore can be visualised with the appropriate optical set-up. In contrast, the technique presented in this chapter uses physical objects (charged droplets) to visualise

the acoustic field. This could be seen as analogous to Kundt's tube experiment [169], [170], where a fine dust of small particles is placed throughout a tube, an acoustic field is then generated at one end of the tube forcing the dust to settle at the nodes of the acoustic wave. Kundt's experiment was initially used to measure the speed of sound in air, but is also a good visualisation of the behaviour of the acoustic wave present in the tube.

There are several limitations of our new visualisation technique as presented here: It can only be used to visualise the acoustic field occupying a small volume of space; it requires the use of diamagnetic levitation and therefore the ability to create large magnetic fields in the region that is to be visualised; the acoustic field can only be viewed from a single orientation; and the technique only gives a qualitative indication of the shape of acoustic wells, hence produces no quantitative data. Even considering all of these limitations, the technique presents a novel way of visualising acoustic fields.

It has been demonstrated that a wide variety of materials may be diamagnetically levitated at much lower magnetic field strengths if surrounded by a paramagnetic fluid [92], [171], [172]. Hence, a diamagnetic levitator constructed of several cheap readily available permanent magnets where the extent of the diamagnetic trap is filled with a paramagnetic fluid, such as an aqueous manganese chloride solution, could easily be able to levitate a powdered diamagnetic substance, e.g. bismuth or graphite. If an external acoustic field is then applied to the fluid, we hypothesise that the levitated powder would move to reside in the wells of the acoustic field and hence allow for visualisation of the acoustic field. If successful, such a system would overcome many of the pitfalls of the aforementioned visualisation set-up, while building upon its fundamental idea. Such a set-up would offer a much cheaper and easier method for visualising acoustic fields than any present method, as no expensive optical set-up or post-processing of images would be required.

# Chapter 7

## Conclusions

In this thesis, we have explored the use of diamagnetic levitation to study bubbles and droplets in zero gravity. We performed a number of experimental investigations using a novel technique to levitate bubbles in a weightless environment, allowing for the study of surface oscillations of bubbles as well as the contactless manipulation of multiple bubbles. We presented a new experimental technique, enabling the levitation and manipulation of multiple spherical droplets inside the bore of a superconducting magnet. We have also carried out numerical simulations to support our experimental results and find good agreement between experiment and simulation in all cases.

### 7.1 Chapter review

In **chapter 1** we gave a brief introduction to the topics studied in this thesis and gave an overview of several levitation techniques and the advantages they provide over alternative methods of studying systems in weightless environments.

In **chapter 2**, we provided a detailed explanation of the theory behind diamagnetic levitation. We introduced Earnshaw's theory and discussed why it does not apply to diamagnetic materials placed within a magnetic field. We then investigated the conditions necessary for the stable levitation of diamagnetic materials and showed these conditions are satisfied in the bore of a solenoid magnet.

In this chapter, we also introduced the superconducting magnet utilised in the experiments presented throughout this thesis. We investigated the shape of magnetogravitational traps produced by the magnet as a function of current through the solenoid coil and presented a simple method to optimise the sphericity of magnetogravitational potential traps, which was utilised in chapter 4.

In **chapter 3** we introduced a novel method to levitate air bubbles surrounded by a fluid using diamagnetic levitation. We reported on previous experiments that had used similar techniques, but show that using our new methodology bubbles may be levitated at room temperature whereas previous experiments required fluids to be kept at cryogenic temperatures. Previous experiments also showed significant defor-

mation to the shape of bubbles due to demagnetisation forces present in experiments. In our experiments, we achieved spherical bubbles in all cases due to the dominance of surface tension over all other forces acting on the surfaces of bubbles.

In **chapter 4** we report on the nonlinear surface oscillations of bubbles. We used the coalescence of a pair of diamagnetically levitated bubbles to introduce a large initial axisymmetric perturbation into the bubble system and then observed the decay of the surface oscillations of the bubble. We studied two cases; a symmetric case where the radii of the bubbles before coalescence were equal (within experimental error) and an asymmetric case where the ratio of the radii of the bubbles was approximately 1.5.

In this chapter, we also approximate the effect of the magnetogravitational potential trap on the surface oscillations of bubbles. Asymptotic expansions are used to derive a formula for the effect of the magnetogravitational potential trap on the oscillation frequency of vanishingly small perturbations on the surface of a bubble in the case of a spherical magnetogravitational potential trap. We use this theory to show that we expect a negligible effect due to the magnetogravitational potential trap on linear surface oscillations of a bubble and hence conclude the magnetogravitational potential trap should have a negligible effect on nonlinear surface oscillations too.

We also carried out numerical simulations to compare with our experimental results. A volume of fluid method was used to carry out direct numerical simulations of the Navier-Stokes equations implemented in the open-source software Basilisk. We present examples of the axisymmetric meshes used in simulation and show how the mesh is adaptively refined near to the liquid-gas interface to reduce computational cost and allow for an accurate representation of the curvature of the interface necessary for the simulation of capillary-driven flows.

For both experiments and simulations, we decompose the interface of the bubbles into spherical harmonics to compare with the theory of Tsamopoulos and Brown [5]. Comparison of the time series for each harmonic showed good agreement between experiment and simulation except for the  $n = 0$  mode. This is due to the incompressibility condition being enforced in the gas phase in simulation. As this was the only discernible difference between experiment and simulation it shows that the small volume oscillations present in the experiment had a negligible effect on all other modes.

We then proceeded to analyse the Fourier transforms of these time series. We found evidence of additional peaks in certain spherical harmonics due to second-order shape corrections, as predicted by Tsampoulos and Brown. In the symmetric case the order of magnitude of these peaks was consistent with the prediction of Tsamopoulos and Brown but in the asymmetric case, the magnitude was at least an order magnitude greater than predicted by theory. Other peaks were also observed in the spectrum of the time series and we showed that some of these peaks are consistent with the shape corrections at third-order, as predicted by M. M. Scase (personal communication, 30 June, 2022).

We then calculated short-time Fourier transforms of the time series. In the case of the dominant modes,  $n = 2$  in the symmetric case, and  $n = 2$  and  $n = 3$  in the asymmetric case, we tracked the amplitude and frequency of the dominant peak. This allowed us to compare the change in frequency as a function of amplitude. For the symmetric case, we observed the relationship between frequency and amplitude to be quadratic as predicted by Tsamopoulos and Brown. In the asymmetric case, we don't observe a quadratic relationship for either the  $n = 2$  or  $n = 3$  modes, although the  $n = 2$  mode approached the value of frequency shift predicted by Tsamopoulos and Brown in the limit of vanishingly small amplitude. We argued that this discrepancy between theory and our results is due to mode coupling, as the theory of Tsamopoulos and Brown only accounts for a single mode undergoing oscillations which is well approximated by the symmetric case.

We also analysed the viscous damping of the dominant modes. We found that damping rates varied slightly between the experiment and simulation due to numerical damping in simulation, although the qualitative behaviour was the same. Interestingly, the damping rate of the  $n = 2$  mode was found to have qualitatively different behaviour in the symmetric case than in the asymmetric case. This was assumed to be because of mode coupling.

Additionally, we comment on the observed translational motion of the bubble in the asymmetric case. We found differing behaviour between experiment and simulation due to the effect of the magnetogravitational trap in experiment not accounted for in simulation.

In **chapter 5** we introduced a new method to generate clusters of diamagnetically levitated bubbles. We showed we could manipulate the configuration of these clusters by adjusting the current in the superconducting magnet used to levitate the bubbles. We showed examples of two bubble clusters, one constructed from seven approximately equal-sized bubbles and one constructed from nineteen approximately equal-sized bubbles. We presented several configurations of these clusters, including a close-packed arrangement and a planar arrangement. We then proceeded to discuss future use cases and applications for bubble clusters.

In **chapter 6** we discussed a new experimental technique we have developed named 'Sonomaglev', which combined acoustic and diamagnetic levitation. We presented our experimental set-up and demonstrated we were able to levitate and manipulate multiple spherical droplets in the bore of our superconducting magnet. We also showed we were able to predict the position of levitated droplets using numerical simulations. In addition to this, we present a novel technique to image the potential field produced inside the bore of the magnet using clouds of charged droplets.

## 7.2 Future work

In chapter 4 we show the first experimental confirmation of the simultaneous ejection of multiple satellite bubbles. It is known from previous studies that the number and

size of ejected satellite bubbles are dependent on only two parameters: the Ohnesorge number and the radii of the ratio of the bubbles before coalescence [64], [66]. A total description of this phase space has never been mapped. We propose experiments and numerical simulations similar to those carried out in chapter 4 could be used to systematically study this problem.

An associated problem similar to that studied in chapter 4 is the nonlinear surface oscillation of droplets. In theory, droplet coalescence could be used to study this problem, but experimentally this proves to be exceedingly difficult. Our experiments on bubble coalescence allow us to simply inject two spherical bubbles next to each other and wait for them to coalesce, in which time the inertia from the motion of the bubble is dissipated and therefore coalescence events start from rest. Applying a similar technique for droplet coalescence has up until recently been impossible, as droplets coalesce almost instantaneously when moved into contact with each other, hence coalescence would start with at least one droplet in motion and in a non-spherical shape. In chapter 6 we introduce a new experimental technique that allows for the controlled manipulation of spherical droplets. In a small number of preliminary experiments carried out using our Sonomaglev set-up, we have been able to levitate two mm–cm droplets with a distance between the surface of the two droplets of order 0.1 mm. By turning the transducers off we were able to bring the droplets together and hence observed droplet coalescence. Due to the small distance separating the droplets and the weak magnetogravitational force accelerating the droplets together, no deviation of the surface of the droplets from spherical was observed. As well as this, the velocity of the droplets before coalescence is several orders of magnitude less than the velocity scale of surface oscillations of the droplets, therefore it is reasonable to treat the droplets as coalescing from rest.

In addition to the study of nonlinear surface oscillations of droplets, this technique could also be used to study the satellite ejection of droplets due to droplet coalescence, as previously reported on by Zhang *et al.* [158]. The experiments of Zhang *et al.* [158] were carried out in settings with terrestrial gravity as well as requiring the pinning of one of the droplets to the end of a capillary tube, leading to the deformation of droplets from spherical and impinging on the free surface oscillations of the droplets. The method proposed here has none of these setbacks and hence could lead to an increased understanding of the underlying fluid flow.

In chapter 6 we introduce a new experimental technique, Sonomaglev. The Sonomaglev system presented in this chapter is very simple consisting of two transducers wired in parallel and controlled by a signal generator. Even still, the system was able to levitate and manipulate multiple droplets. By adding more transducers, the operating voltage and phase of each being controlled independently, we could create systems that have much more control and flexibility in the positioning of the droplets. Such systems could pave the way for new results in chemistry and biochemistry, as experimental set-ups could be constructed that allow for the manipulation, mixing and analysis of small volumes of liquid without the problems associated with the presence of container walls, such as adsorption and contamination of the analyte, or

measurement interference.

At the end of chapter 5 we hypothesise several use cases for the bubble clusters. The first of which is as a tool to create new acoustic metamaterials, and the second is as a new experimental way to study the nonlinear interactions of bubbles in an oscillating acoustic field. In addition to this, bubble clusters make the ideal tool to study the properties of monodisperse wet foams in zero gravity.

### 7.3 Closing statement

Throughout this thesis, I have explored the use of diamagnetic levitation to study bubbles and droplets in a weightless environment. I have used this technique to test previously untested theories and experimentally validate previous numerical results, as well as to create a new experimental technique. I am hoping this body of work shows how useful a tool diamagnetic levitation can be. But still, to many researchers, diamagnetic levitation remains unknown.

Manned missions to Mars currently seem like an inevitability, but before this can happen more research is needed on understanding certain biological and physical processes in reduced or zero gravity conditions. To most academics, they assume this is only possible either onboard the ISS or on parabolic flights. In a number of cases, experiments carried out onboard the ISS or parabolic flights could have been conducted using diamagnetic levitation, which could have saved the researchers time, money and energy. Although diamagnetic levitation requires the use of strong magnetic fields, usually created using superconducting magnets which require cooling down to approximately 4 K, the energy required to do this for several days is significantly less than to fly a plane for 2–3 hours or to send a rocket into space. In the current climate crisis, the reduction in energy usage in experimental studies should be of paramount importance where possible.

# Bibliography

- [1] A. Yarin, M. Pfaffenlehner, and C. Tropea, “On the acoustic levitation of droplets,” *Journal of Fluid Mechanics*, vol. 356, pp. 65–91, 1998.
- [2] M. A. Andrade, N. Pérez, and J. C. Adamowski, “Review of progress in acoustic levitation,” *Brazilian Journal of Physics*, vol. 48, pp. 190–213, 2018.
- [3] W.-K. Rhim, S. K. Chung, D. Barber, *et al.*, “An electrostatic levitator for high-temperature containerless materials processing in 1-g,” *Review of Scientific Instruments*, vol. 64, no. 10, pp. 2961–2970, 1993.
- [4] M. V. Berry and A. K. Geim, “Of flying frogs and levitrons,” *European Journal of Physics*, vol. 18, no. 4, p. 307, 1997.
- [5] J. A. Tsamopoulos and R. A. Brown, “Nonlinear oscillations of inviscid drops and bubbles,” *Journal of Fluid Mechanics*, vol. 127, pp. 519–537, 1983.
- [6] E. Brandt, “Levitation in physics,” *Science*, vol. 243, no. 4889, pp. 349–355, 1989.
- [7] R. Herranz, O. J. Larkin, C. E. Dijkstra, *et al.*, “Microgravity simulation by diamagnetic levitation: Effects of a strong gradient magnetic field on the transcriptional profile of drosophila melanogaster,” *BMC genomics*, vol. 13, no. 1, pp. 1–14, 2012.
- [8] J. M. Valles Jr, K. Lin, J. M. Denegre, and K. L. Mowry, “Stable magnetic field gradient levitation of xenopus laevis: Toward low-gravity simulation,” *Biophysical Journal*, vol. 73, no. 2, pp. 1130–1133, 1997.
- [9] R. Hill, O. Larkin, P. Anthony, *et al.*, “Effects of diamagnetic levitation on bacterial growth in liquid,” *Nature Precedings*, pp. 1–1, 2010.
- [10] K. Guevorkian and J. M. Valles Jr, “Swimming paramecium in magnetically simulated enhanced, reduced, and inverted gravity environments,” *Proceedings of the National Academy of Sciences*, vol. 103, no. 35, pp. 13 051–13 056, 2006.
- [11] M. Heijna, P. Poodt, K. Tsukamoto, *et al.*, “Magnetically controlled gravity for protein crystal growth,” *Applied physics letters*, vol. 90, no. 26, p. 264 105, 2007.

- [12] P. Lopez-Alcaraz, A. Catherall, R. Hill, M. Leaper, M. R. Swift, and P. King, “Magneto-vibratory separation of glass and bronze granular mixtures immersed in a paramagnetic liquid,” *The European Physical Journal E*, vol. 24, pp. 145–156, 2007.
- [13] R. Hill and L. Eaves, “Vibrations of a diamagnetically levitated water droplet,” *Physical review E*, vol. 81, no. 5, p. 056 312, 2010.
- [14] R. Hill and L. Eaves, “Shape oscillations of an electrically charged diamagnetically levitated droplet,” *Applied Physics Letters*, vol. 100, no. 11, p. 114 106, 2012.
- [15] R. H. Temperton, R. J. Hill, and J. S. Sharp, “Mechanical vibrations of magnetically levitated viscoelastic droplets,” *Soft Matter*, vol. 10, no. 29, pp. 5375–5379, 2014.
- [16] R. Hill and L. Eaves, “Nonaxisymmetric shapes of a magnetically levitated and spinning water droplet,” *Physical review letters*, vol. 101, no. 23, p. 234 501, 2008.
- [17] L. Liao and R. J. Hill, “Shapes and fissility of highly charged and rapidly rotating levitated liquid drops,” *Physical Review Letters*, vol. 119, no. 11, p. 114 501, 2017.
- [18] K. A. Baldwin, M. M. Scase, and R. J. Hill, “The inhibition of the rayleigh-taylor instability by rotation,” *Scientific reports*, vol. 5, no. 1, pp. 1–12, 2015.
- [19] M. Scase, K. Baldwin, and R. Hill, “Magnetically induced rayleigh-taylor instability under rotation: Comparison of experimental and theoretical results,” *Physical Review E*, vol. 102, no. 4, p. 043 101, 2020.
- [20] K. A. Baldwin, S. L. Butler, and R. J. Hill, “Artificial tektites: An experimental technique for capturing the shapes of spinning drops,” *Scientific reports*, vol. 5, no. 1, pp. 1–5, 2015.
- [21] W. Thomson, *Reprint of papers on electrostatics and magnetism*. Macmillan & Company, 1872.
- [22] S. Earnshaw, “On the nature of the molecular forces which regulate the constitution of the luminiferous ether,” *Transactions of the Cambridge Philosophical Society*, vol. 7, p. 97, 1848.
- [23] W. Braunbek, “Freischwebende körper im elektrischen und magnetischen feld,” *Zeitschrift für Physik*, vol. 112, no. 11-12, pp. 753–763, 1939.
- [24] W. Braunbek, “Freies schweben diamagnetischer körper im magnetfeld,” *Zeitschrift für Physik*, vol. 112, no. 11-12, pp. 764–769, 1939.
- [25] A. Boerdijk, “Levitation by static magnetic fields,” *Philips technical review*, vol. 18, no. 125-127, p. 5, 1956.
- [26] R. D. Waldron, “Diamagnetic levitation using pyrolytic graphite,” *Review of Scientific Instruments*, vol. 37, no. 1, pp. 29–35, 1966.

- [27] B. Kendall, M. Voller, and L. Hinkle, "Passive levitation of small particles in vacuum: Possible applications to vacuum gauging," *Journal of Vacuum Science & Technology A: Vacuum, Surfaces, and Films*, vol. 5, no. 4, pp. 2458–2462, 1987.
- [28] E. Beaugnon and R. Tournier, "Levitation of organic materials," *Nature*, vol. 349, no. 6309, pp. 470–470, 1991.
- [29] C. Paine and G. Seidel, "Magnetic levitation of condensed hydrogen," *Review of scientific instruments*, vol. 62, no. 12, pp. 3022–3024, 1991.
- [30] M. Weilert, D. L. Whitaker, H. Maris, and G. Seidel, "Magnetic levitation of liquid helium," *Journal of low temperature physics*, vol. 106, pp. 101–131, 1997.
- [31] A. Catherall, P. Lopez-Alcaraz, K. Benedict, P. King, and L. Eaves, "Cryogenically enhanced magneto-archimedes levitation," *New Journal of Physics*, vol. 7, no. 1, p. 118, 2005.
- [32] V. Garbin, D. Cojoc, E. Ferrari, *et al.*, "Changes in microbubble dynamics near a boundary revealed by combined optical micromanipulation and high-speed imaging," *Applied physics letters*, vol. 90, no. 11, p. 114103, 2007.
- [33] E. Trinh, D. Thiessen, and R. Holt, "Driven and freely decaying nonlinear shape oscillations of drops and bubbles immersed in a liquid: Experimental results," *Journal of Fluid Mechanics*, vol. 364, pp. 253–272, 1998.
- [34] F. R. Young, *Sonoluminescence*. CRC Press, 2005.
- [35] F. J. Montes, M. A. Galán, and R. L. Cerro, "Mass transfer from oscillating bubbles in bioreactors," *Chem. Eng. Sci.*, vol. 54, p. 3127, 1999.
- [36] M. Martín, F. J. Montes, and M. A. Galán, "Mass transfer from oscillating bubbles in bubble column reactors," *Chem. Eng. J.*, vol. 151, p. 79, 2009.
- [37] G. Pichavant, B. Cariteau, D. Chatain, V. Nikolayev, and D. Beysens, "Magnetic compensation of gravity: Experiments with oxygen," *Microgravity Science and Technology*, vol. 21, pp. 129–133, 2009.
- [38] J. Duplat and A. Mailfert, "On the bubble shape in a magnetically compensated gravity environment," *Journal of Fluid Mechanics*, vol. 716, R11, 2013.
- [39] W. Fritz, "Berechnung des maximalvolumens von dampfblasen," *Physik. Zeitschr*, vol. 36, pp. 379–384, 1935.
- [40] R. Kumar and N. Kuloor, "The formation of bubbles and drops," in *Advances in chemical engineering*, vol. 8, Elsevier, 1970, pp. 255–368.
- [41] H. N. Oguz and A. Prosperetti, "Dynamics of bubble growth and detachment from a needle," *Journal of Fluid Mechanics*, vol. 257, pp. 111–145, 1993.
- [42] P. Novotny and O. Sohnel, "Densities of binary aqueous solutions of 306 inorganic substances," *Journal of Chemical and Engineering Data*, vol. 33, no. 1, pp. 49–55, 1988.

- [43] M. L. Huber, R. A. Perkins, A. Laesecke, *et al.*, “New international formulation for the viscosity of h<sub>2</sub>o,” *Journal of Physical and Chemical Reference Data*, vol. 38, no. 2, pp. 101–125, 2009.
- [44] J. Illingworth and J. Kittler, “A survey of the hough transform,” *Computer vision, graphics, and image processing*, vol. 44, no. 1, pp. 87–116, 1988.
- [45] I. Sobel, “Camera Models and Machine Perception,” 1970.
- [46] G. Hunter-Brown, N. Sampara, M. M. Scase, and R. J. A. Hill, “Nonlinear oscillations of a magnetically levitated air bubble in water,” 2023, (*Manuscript under review*).
- [47] H. Lamb, *Hydrodynamics*. The University Press, 1932, ISBN: 9780521055154.
- [48] L. Rayleigh, “On the capillary phenomena of jets,” *Proc. R. Soc. London*, vol. 29, no. 196-199, pp. 71–97, 1879.
- [49] C. Miller and L. Scriven, “The oscillations of a fluid droplet immersed in another fluid,” *Journal of fluid mechanics*, vol. 32, no. 3, pp. 417–435, 1968.
- [50] A. Prosperetti, “Free oscillations of drops and bubbles: The initial-value problem,” *Journal of Fluid Mechanics*, vol. 100, no. 2, pp. 333–347, 1980.
- [51] A. H. Nayfeh and D. T. Mook, *Nonlinear oscillations*. John Wiley & Sons, 1979.
- [52] J. A. Tsamopoulos, “Nonlinear dynamics of simple and compound drops,” Ph.D. dissertation, Massachusetts Institute of Technology, 1985.
- [53] J. A. Tsamopoulos, “Nonlinear dynamics and break-up of charged drops,” in *AIP Conference Proceedings*, vol. 197, 1990, pp. 169–187.
- [54] T. Wang, A. Anilkumar, and C. Lee, “Oscillations of liquid drops: Results from usml-1 experiments in space,” *Journal of Fluid Mechanics*, vol. 308, pp. 1–14, 1996.
- [55] E. Becker, W. Hiller, and T. Kowalewski, “Experimental and theoretical investigation of large-amplitude oscillations of liquid droplets,” *Journal of Fluid Mechanics*, vol. 231, pp. 189–210, 1991.
- [56] U. Kornek, F. Müller, K. Harth, *et al.*, “Oscillations of soap bubbles,” *New Journal of Physics*, vol. 12, no. 7, p. 073031, 2010.
- [57] C. Vicente, W. Yao, H. Maris, and G. Seidel, “Surface tension of liquid 4 he as measured using the vibration modes of a levitated drop,” *Physical Review B*, vol. 66, no. 21, p. 214504, 2002.
- [58] S. Popinet and Collaborators, *Basilisk c*, Mar. 8, 2023. [Online]. Available: <http://basilisk.fr>.
- [59] S. Popinet, “An accurate adaptive solver for surface-tension-driven interfacial flows,” *Journal of Computational Physics*, vol. 228, no. 16, pp. 5838–5866, 2009.

- [60] S. Popinet, “A quadtree-adaptive multigrid solver for the serre–green–naghdi equations,” *Journal of Computational Physics*, vol. 302, pp. 336–358, 2015.
- [61] G. Tryggvason, R. Scardovelli, and S. Zaleski, *Direct numerical simulations of gas–liquid multiphase flows*. Cambridge university press, 2011.
- [62] C. W. Hirt and B. D. Nichols, “Volume of fluid (vof) method for the dynamics of free boundaries,” *Journal of computational physics*, vol. 39, no. 1, pp. 201–225, 1981.
- [63] J. U. Brackbill, D. B. Kothe, and C. Zemach, “A continuum method for modeling surface tension,” *Journal of computational physics*, vol. 100, no. 2, pp. 335–354, 1992.
- [64] F. Zhang and S. Thoroddsen, “Satellite generation during bubble coalescence,” *Physics of Fluids*, vol. 20, no. 2, p. 022 104, 2008.
- [65] Á. M. Soto, T. Maddalena, A. Fraters, D. Van Der Meer, and D. Lohse, “Coalescence of diffusively growing gas bubbles,” *Journal of fluid mechanics*, vol. 846, pp. 143–165, 2018.
- [66] M. Ohnishi, H. Azuma, and J. Straub, “Study on secondary bubble creation induced by bubble coalescence,” *Advances in Space Research*, vol. 24, no. 10, pp. 1331–1336, 1999.
- [67] E. Ghabache and T. Séon, “Size of the top jet drop produced by bubble bursting,” *Physical Review Fluids*, vol. 1, no. 5, p. 051 901, 2016.
- [68] J. Gordillo and J. Rodriguez-Rodriguez, “Capillary waves control the ejection of bubble bursting jets,” *Journal of Fluid Mechanics*, vol. 867, pp. 556–571, 2019.
- [69] A. Tufaile and J. Sartorelli, “Bubble and spherical air shell formation dynamics,” *Physical Review E*, vol. 66, no. 5, p. 056 204, 2002.
- [70] T. J. Asaki, P. L. Marston, and E. H. Trinh, “Shape oscillations of bubbles in water driven by modulated ultrasonic radiation pressure: Observations and detection with scattered laser light,” *The Journal of the Acoustical Society of America*, vol. 93, no. 2, pp. 706–713, 1993.
- [71] F. J. Harris, “On the use of windows for harmonic analysis with the discrete fourier transform,” *Proceedings of the IEEE*, vol. 66, no. 1, pp. 51–83, 1978.
- [72] T. B. Benjamin and A. T. Ellis, “Self-propulsion of asymmetrically vibrating bubbles,” *Journal of Fluid Mechanics*, vol. 212, pp. 65–80, 1990.
- [73] A. A. Doinikov, “Translational motion of a bubble undergoing shape oscillations,” *Journal of Fluid Mechanics*, vol. 501, pp. 1–24, 2004.
- [74] S. J. Shaw, “Translation and oscillation of a bubble under axisymmetric deformation,” *Physics of fluids*, vol. 18, no. 7, p. 072 104, 2006.

- [75] D. Plümacher, M. Oberlack, Y. Wang, and M. Smuda, “On a non-linear droplet oscillation theory via the unified method,” *Physics of Fluids*, vol. 32, no. 6, p. 067104, 2020.
- [76] I. Cantat, S. Cohen-Addad, F. Elias, *et al.*, *Foams: structure and dynamics*. OUP Oxford, 2013.
- [77] C. Hill and J. Eastoe, “Foams: From nature to industry,” *Advances in colloid and interface science*, vol. 247, pp. 496–513, 2017.
- [78] J. Whittaker, “Cercopid spittle as a microhabitat,” *Oikos*, pp. 59–64, 1970.
- [79] D. Andrade and A. S. Abe, “Foam nest production in the armoured catfish,” *Journal of Fish Biology*, vol. 50, no. 3, pp. 665–667, 1997.
- [80] L. Dalgetty and M. W. Kennedy, “Building a home from foam—túngara frog foam nest architecture and three-phase construction process,” *Biology letters*, vol. 6, no. 3, pp. 293–296, 2010.
- [81] A. Ratzler, “History and development of foam as a fire extinguishing medium,” *Industrial & Engineering Chemistry*, vol. 48, no. 11, pp. 2013–2016, 1956.
- [82] J. Seow, *Fire fighting foams with perfluorochemicals-environmental review*. Hemming Information Services London, UK, 2013.
- [83] A. Nguyen and H. J. Schulze, *Colloidal science of flotation*. CRC Press, 2003.
- [84] E. A. Deliyanni, G. Z. Kyzas, and K. A. Matis, “Various flotation techniques for metal ions removal,” *Journal of Molecular Liquids*, vol. 225, pp. 260–264, 2017.
- [85] P. Stevenson, *Foam engineering: fundamentals and applications*. John Wiley & Sons, 2012.
- [86] A. J. Wilson, *Foams: physics, chemistry and structure*. Springer Science & Business Media, 2013.
- [87] D. L. Weaire and S. Hutzler, *The physics of foams*. Oxford University Press, 2001.
- [88] N. Vandewalle, H. Caps, G. Delon, *et al.*, “Foam stability in microgravity,” in *Journal of Physics: Conference Series*, IOP Publishing, vol. 327, 2011, p. 012024.
- [89] H. Caps, N. Vandewalle, A. Saint-Jalmes, *et al.*, “How foams unstable on earth behave in microgravity?” *Colloids and Surfaces A: Physicochemical and Engineering Aspects*, vol. 457, pp. 392–396, 2014.
- [90] D. Langevin, “Aqueous foams and foam films stabilised by surfactants. gravity-free studies,” *Comptes Rendus Mécanique*, vol. 345, no. 1, pp. 47–55, 2017.
- [91] N. Isert, G. Maret, and C. M. Aegerter, “Coarsening dynamics of three-dimensional levitated foams: From wet to dry,” *The European Physical Journal E*, vol. 36, pp. 1–6, 2013.

- [92] F. Ilievski, K. A. Mirica, A. K. Ellerbee, and G. M. Whitesides, “Templated self-assembly in three dimensions using magnetic levitation,” *Soft Matter*, vol. 7, no. 19, pp. 9113–9118, 2011.
- [93] G. Ma and P. Sheng, “Acoustic metamaterials: From local resonances to broad horizons,” *Science advances*, vol. 2, no. 2, e1501595, 2016.
- [94] Z. Liu, X. Zhang, Y. Mao, *et al.*, “Locally resonant sonic materials,” *science*, vol. 289, no. 5485, pp. 1734–1736, 2000.
- [95] H. Chen and C. T. Chan, “Acoustic cloaking in three dimensions using acoustic metamaterials,” *Applied physics letters*, vol. 91, no. 18, p. 183518, 2007.
- [96] T. X. Misaridis, K. Gammelmark, C. H. Jørgensen, *et al.*, “Potential of coded excitation in medical ultrasound imaging,” *Ultrasonics*, vol. 38, no. 1-8, pp. 183–189, 2000.
- [97] D. Cosgrove, “Ultrasound contrast agents: An overview,” *European journal of radiology*, vol. 60, no. 3, pp. 324–330, 2006.
- [98] S. Qin, C. F. Caskey, and K. W. Ferrara, “Ultrasound contrast microbubbles in imaging and therapy: Physical principles and engineering,” *Physics in medicine & biology*, vol. 54, no. 6, R27, 2009.
- [99] U. Parlitz, R. Mettin, S. Luther, I. Akhatov, M. Voss, and W. Lauterborn, “Spatio-temporal dynamics of acoustic cavitation bubble clouds,” *Philosophical Transactions of the Royal Society of London. Series A: Mathematical, Physical and Engineering Sciences*, vol. 357, no. 1751, pp. 313–334, 1999.
- [100] J. T. Tervo, R. Mettin, and W. Lauterborn, “Bubble cluster dynamics in acoustic cavitation,” *Acta acustica united with acustica*, vol. 92, no. 1, pp. 178–180, 2006.
- [101] Z. Zeravcic, D. Lohse, and W. Van Saarloos, “Collective oscillations in bubble clouds,” *Journal of fluid mechanics*, vol. 680, pp. 114–149, 2011.
- [102] S. Behnia, H. Zahir, M. Yahyavi, A. Barzegar, and F. Mobadersani, “Observations on the dynamics of bubble cluster in an ultrasonic field,” *Nonlinear Dynamics*, vol. 72, pp. 561–574, 2013.
- [103] D. A. Beysens and J. J. Van Loon, *Generation and applications of extra-terrestrial environments on earth*. Taylor & Francis, 2015.
- [104] T. Hoshi, M. Takahashi, T. Iwamoto, and H. Shinoda, “Noncontact tactile display based on radiation pressure of airborne ultrasound,” *IEEE Transactions on Haptics*, vol. 3, no. 3, pp. 155–165, 2010.
- [105] A. Marzo, S. A. Seah, B. W. Drinkwater, D. R. Sahoo, B. Long, and S. Subramanian, “Holographic acoustic elements for manipulation of levitated objects,” *Nature communications*, vol. 6, no. 1, p. 8661, 2015.

- [106] R. H. Morris, E. R. Dye, P. Docker, and M. I. Newton, “Beyond the langevin horn: Transducer arrays for the acoustic levitation of liquid drops,” *Physics of Fluids*, vol. 31, no. 10, p. 101301, 2019.
- [107] N. Leopold, M. Haberkorn, T. Laurell, *et al.*, “On-line monitoring of airborne chemistry in levitated nanodroplets: In situ synthesis and application of sers-active ag-sols for trace analysis by ft-raman spectroscopy,” *Analytical chemistry*, vol. 75, no. 9, pp. 2166–2171, 2003.
- [108] J. Leiterer, W. Leitenberger, F. Emmerling, A. F. Thünemann, and U. Panne, “The use of an acoustic levitator to follow crystallization in small droplets by energy-dispersive x-ray diffraction,” *Journal of applied crystallography*, vol. 39, no. 5, pp. 771–773, 2006.
- [109] M. S. Westphall, K. Jorabchi, and L. M. Smith, “Mass spectrometry of acoustically levitated droplets,” *Analytical chemistry*, vol. 80, no. 15, pp. 5847–5853, 2008.
- [110] C. Warschat, A. Stindt, U. Panne, and J. Riedel, “Mass spectrometry of levitated droplets by thermally unconfined infrared-laser desorption,” *Analytical chemistry*, vol. 87, no. 16, pp. 8323–8327, 2015.
- [111] S. Tsujino and T. Tomizaki, “Ultrasonic acoustic levitation for fast frame rate x-ray protein crystallography at room temperature,” *Scientific reports*, vol. 6, no. 1, pp. 1–9, 2016.
- [112] S. J. Brotton and R. I. Kaiser, “Controlled chemistry via contactless manipulation and merging of droplets in an acoustic levitator,” *Analytical Chemistry*, vol. 92, no. 12, pp. 8371–8377, 2020.
- [113] J. Gao, C. Cao, and B. Wei, “Containerless processing of materials by acoustic levitation,” *Advances in Space Research*, vol. 24, no. 10, pp. 1293–1297, 1999.
- [114] C. Benmore and J. Weber, “Amorphization of molecular liquids of pharmaceutical drugs by acoustic levitation,” *Physical Review X*, vol. 1, no. 1, p. 011004, 2011.
- [115] C. J. Benmore, J. Weber, A. N. Taylor, *et al.*, “Structural characterization and aging of glassy pharmaceuticals made using acoustic levitation,” *Journal of pharmaceutical sciences*, vol. 102, no. 4, pp. 1290–1300, 2013.
- [116] V. Vandaele, P. Lambert, and A. Delchambre, “Non-contact handling in microassembly: Acoustical levitation,” *Precision engineering*, vol. 29, no. 4, pp. 491–505, 2005.
- [117] S. Deng, K. Jia, E. Wu, X. Hu, Z. Fan, and K. Yang, “Controllable micro-particle rotation and transportation using sound field synthesis technique,” *Applied Sciences*, vol. 8, no. 1, p. 73, 2018.

- [118] M. A. Andrade, T. S. Camargo, and A. Marzo, “Automatic contactless injection, transportation, merging, and ejection of droplets with a multifocal point acoustic levitator,” *Review of Scientific Instruments*, vol. 89, no. 12, p. 125 105, 2018.
- [119] I. Ezcurdia, R. Morales, M. A. Andrade, and A. Marzo, “Leviprint: Contactless fabrication using full acoustic trapping of elongated parts.,” in *ACM SIGGRAPH 2022 Conference Proceedings*, 2022, pp. 1–9.
- [120] G. Hunter-Brown, N. Sampara, M. M. Scase, and R. J. A. Hill, “Sonomaglev: Combining acoustic and diamagnetic levitation,” *Appl. Phys. Lett.*, vol. 122, no. 1, p. 014 103, 2023.
- [121] K. Bücks and H. Müller, “Über einige beobachtungen an schwingenden piezo-quarzen und ihrem schallfeld,” *Zeitschrift für Physik*, vol. 84, pp. 75–86, 1933.
- [122] T. Hoshi, Y. Ochiai, and J. Rekimoto, “Three-dimensional noncontact manipulation by opposite ultrasonic phased arrays,” *Japanese Journal of Applied Physics*, vol. 53, no. 7S, 07KE07, 2014.
- [123] F.-S. Lin, P.-W. Yang, C.-C. Hsieh, *et al.*, “Investigation of a novel acoustic levitation technique using the transition period between acoustic pulse trains and electrical driving signals,” *IEEE Transactions on Ultrasonics, Ferroelectrics, and Frequency Control*, vol. 69, no. 2, pp. 769–778, 2021.
- [124] M. Röthlisberger, G. Schmidli, M. Schuck, and J. W. Kolar, “Multi-frequency acoustic levitation and trapping of particles in all degrees of freedom,” *IEEE Transactions on Ultrasonics, Ferroelectrics, and Frequency Control*, vol. 69, no. 4, pp. 1572–1575, 2022.
- [125] Z. Long, H. Zhao, H. Peng, M. Yao, Y. Pan, and Z. Li, “Acoustic levitation for large particle based on concave spherical transducer arrays,” *IEEE Sensors Journal*, vol. 22, no. 18, pp. 18 104–18 113, 2022.
- [126] J. Rudnick and M. Barmatz, “Oscillational instabilities in single-mode acoustic levitators,” *The Journal of the Acoustical Society of America*, vol. 87, no. 1, pp. 81–92, 1990.
- [127] M. A. Andrade, N. Pérez, and J. C. Adamowski, “Experimental study of the oscillation of spheres in an acoustic levitator,” *The Journal of the Acoustical Society of America*, vol. 136, no. 4, pp. 1518–1529, 2014.
- [128] E. Trinh and J. Robey, “Experimental study of streaming flows associated with ultrasonic levitators,” *Physics of Fluids*, vol. 6, no. 11, pp. 3567–3579, 1994.
- [129] K. Hasegawa, Y. Abe, A. Kaneko, Y. Yamamoto, and K. Aoki, “Visualization measurement of streaming flows associated with a single-acoustic levitator,” *Microgravity Science and Technology*, vol. 21, pp. 9–14, 2009.

- [130] L. Cox, A. Croxford, B. Drinkwater, and A. Marzo, “Acoustic lock: Position and orientation trapping of non-spherical sub-wavelength particles in mid-air using a single-axis acoustic levitator,” *Applied Physics Letters*, vol. 113, no. 5, p. 054 101, 2018.
- [131] P. Helander, T. Puranen, A. Meriläinen, *et al.*, “Omnidirectional microscopy by ultrasonic sample control,” *Applied Physics Letters*, vol. 116, no. 19, p. 194 101, 2020.
- [132] N. Kawahara, A. Yarin, G. Brenn, O. Kastner, and F. Durst, “Effect of acoustic streaming on the mass transfer from a sublimating sphere,” *Physics of Fluids*, vol. 12, no. 4, pp. 912–923, 2000.
- [133] A. L. Yarin, G. Brenn, O. Kastner, D. Rensink, and C. Tropea, “Evaporation of acoustically levitated droplets,” *Journal of Fluid Mechanics*, vol. 399, pp. 151–204, 1999.
- [134] C. Shen, W. Xie, and B. Wei, “Parametrically excited sectorial oscillation of liquid drops floating in ultrasound,” *Physical Review E*, vol. 81, no. 4, p. 046 305, 2010.
- [135] A. Picard, R. Davis, M. Gläser, and K. Fujii, “Revised formula for the density of moist air (cipm-2007),” *Metrologia*, vol. 45, no. 2, p. 149, 2008.
- [136] J. F. Schenck, “The role of magnetic susceptibility in magnetic resonance imaging: Mri magnetic compatibility of the first and second kinds,” *Medical physics*, vol. 23, no. 6, pp. 815–850, 1996.
- [137] R. Davis, “Equation for the volume magnetic susceptibility of moist air,” *Metrologia*, vol. 35, no. 1, p. 49, 1998.
- [138] L. P. Gor’kov, “On the Forces Acting on a Small Particle in an Acoustical Field in an Ideal Fluid,” *Soviet Physics Doklady*, vol. 6, p. 773, Mar. 1962.
- [139] L. D. Landau and E. M. Lifshitz, *Fluid Mechanics: Landau and Lifshitz: Course of Theoretical Physics, Volume 6*. Elsevier, 2013, vol. 6.
- [140] J. Lighthill, *Waves in fluids*. Cambridge university press, 2001.
- [141] D. Noreland, “Impedance boundary conditions for acoustic waves in a duct with a step discontinuity,” *Comput. Methods Appl. Mech. Eng.*, vol. 71, no. 2, pp. 197–224, 2003.
- [142] A. E. Farjat and J. I. Etcheverry, “Mathematical modeling of the radiated acoustic field of ultrasonic transducers,” *J. Nondestruct. Test. Ultrason.*, vol. 2007, no. 11, pp. 1–12, 2007.
- [143] A. Marzo, A. Barnes, and B. W. Drinkwater, “Tinylev: A multi-emitter single-axis acoustic levitator,” *Review of Scientific Instruments*, vol. 88, no. 8, p. 085 105, 2017.

- [144] T. Kozuka, K. Yasui, T. Tuziuti, A. Towata, and Y. Iida, “Acoustic standing-wave field for manipulation in air,” *Japanese Journal of Applied Physics*, vol. 47, no. 5S, p. 4336, 2008.
- [145] M. A. Andrade, N. Perez, F. Buiocchi, and J. C. Adamowski, “Matrix method for acoustic levitation simulation,” *IEEE transactions on ultrasonics, ferro-electrics, and frequency control*, vol. 58, no. 8, pp. 1674–1683, 2011.
- [146] B. Engquist and A. Majda, “Absorbing boundary conditions for numerical simulation of waves,” *Proceedings of the National Academy of Sciences*, vol. 74, no. 5, pp. 1765–1766, 1977.
- [147] F. Collino *et al.*, “High order absorbing boundary conditions for wave propagation models: Straight line boundary and corner cases,” in *Second International Conference on Mathematical and Numerical Aspects of Wave Propagation (Newark, DE, 1993)*, 1993, pp. 161–171.
- [148] C. I. Goldstein, “A finite element method for solving helmholtz type equations in waveguides and other unbounded domains,” *Mathematics of Computation*, vol. 39, no. 160, pp. 309–324, 1982.
- [149] J. B. Keller and D. Givoli, “Exact non-reflecting boundary conditions,” *Journal of computational physics*, vol. 82, no. 1, pp. 172–192, 1989.
- [150] A. Bermúdez, L. Hervella-Nieto, A. Prieto, R. Rodri, *et al.*, “An optimal perfectly matched layer with unbounded absorbing function for time-harmonic acoustic scattering problems,” *Journal of computational Physics*, vol. 223, no. 2, pp. 469–488, 2007.
- [151] R. Cimpéanu, A. Martinsson, and M. Heil, “A parameter-free perfectly matched layer formulation for the finite-element-based solution of the helmholtz equation,” *Journal of Computational Physics*, vol. 296, pp. 329–347, 2015.
- [152] J. Deakin, *Optimal PML transformations for the Helmholtz equation*. The University of Manchester (United Kingdom), 2020.
- [153] C. F. Van Loan and G. Golub, “Matrix computations (johns hopkins studies in mathematical sciences),” *Matrix Computations*, vol. 53, 1996.
- [154] W. Layton and M. Sussman, “Numerical linear algebra,” *University of Pittsburgh, Pittsburgh*, pp. 28–39, 2014.
- [155] F. Hecht, “New development in freefem++,” *Journal of numerical mathematics*, vol. 20, no. 3-4, pp. 251–266, 2012.
- [156] F. Hecht, *A high level multiphysics finite element software*. [Online]. Available: <https://freefem.org/>.
- [157] V. Laude, *Phononic crystals: artificial crystals for sonic, acoustic, and elastic waves*. Walter de Gruyter GmbH & Co KG, 2020.

- [158] F. Zhang, E. Li, and S. T. Thoroddsen, “Satellite formation during coalescence of unequal size drops,” *Physical review letters*, vol. 102, no. 10, p. 104502, 2009.
- [159] O. Wright, “Gallery of whispers,” *Physics World*, vol. 25, no. 02, p. 31, 2012.
- [160] Y. Kitahama, Y. Kimura, and K. Takazawa, “Study of internal structure of meso-tetrakis (4-sulfonatophenyl) porphine j-aggregates in solution by fluorescence microscope imaging in a magnetic field,” *Langmuir*, vol. 22, no. 18, pp. 7600–7604, 2006.
- [161] J. Perenboom, S. Wiegers, P. Christianen, U. Zeitler, and J. Maan, “Research in high magnetic fields: The installation at the university of nijmegen,” *Journal of low temperature physics*, vol. 133, pp. 181–201, 2003.
- [162] P. Van Rhee, R. Rikken, L. Abdelmohsen, *et al.*, “Polymersome magnetovalves for reversible capture and release of nanoparticles,” *Nature communications*, vol. 5, no. 1, p. 5010, 2014.
- [163] D. Foresti, M. Nabavi, M. Klingauf, A. Ferrari, and D. Poulikakos, “Acoustophoretic contactless transport and handling of matter in air,” *Proceedings of the National Academy of Sciences*, vol. 110, no. 31, pp. 12549–12554, 2013.
- [164] A. Watanabe, K. Hasegawa, and Y. Abe, “Contactless fluid manipulation in air: Droplet coalescence and active mixing by acoustic levitation,” *Scientific reports*, vol. 8, no. 1, p. 10221, 2018.
- [165] W. Merzkirch, *Flow visualization*. Elsevier, 2012.
- [166] G. S. Settles and M. J. Hargather, “A review of recent developments in schlieren and shadowgraph techniques,” *Measurement Science and Technology*, vol. 28, no. 4, p. 042001, 2017.
- [167] B. R. Sutherland, S. B. Dalziel, G. O. Hughes, and P. Linden, “Visualization and measurement of internal waves by ‘synthetic schlieren’. part 1. vertically oscillating cylinder,” *Journal of fluid mechanics*, vol. 390, pp. 93–126, 1999.
- [168] K. Bertling, J. Perchoux, T. Taimre, *et al.*, “Imaging of acoustic fields using optical feedback interferometry,” *Optics express*, vol. 22, no. 24, pp. 30346–30356, 2014.
- [169] A. Kundt, “Ueber eine neue art akustischer staubfiguren und über die anwendung derselben zur bestimmung der schallgeschwindigkeit in festen körpern und gasen,” *Annalen der Physik*, vol. 203, no. 4, pp. 497–523, 1866.
- [170] A. Kundt, “Iii. acoustic experiments,” *The London, Edinburgh, and Dublin Philosophical Magazine and Journal of Science*, vol. 35, no. 234, pp. 41–48, 1868.

- [171] A. Winkleman, R. Perez-Castillejos, K. L. Gudiksen, S. T. Phillips, M. Prentiss, and G. M. Whitesides, “Density-based diamagnetic separation: Devices for detecting binding events and for collecting unlabeled diamagnetic particles in paramagnetic solutions,” *Analytical chemistry*, vol. 79, no. 17, pp. 6542–6550, 2007.
- [172] A. B. Subramaniam, D. Yang, H.-D. Yu, *et al.*, “Noncontact orientation of objects in three-dimensional space using magnetic levitation,” *Proceedings of the National Academy of Sciences*, vol. 111, no. 36, pp. 12 980–12 985, 2014.